INFORMATION TO USERS

This manuscript has been reproduced from the microfilm master. UMI films the text directly from the original or copy submitted. Thus, some thesis and dissertation copies are in typewriter face, while others may be from any type of computer printer.

The quality of this reproduction is dependent upon the quality of the copy submitted. Broken or indistinct print, colored or poor quality illustrations and photographs, print bleedthrough, substandard margins, and improper alignment can adversely affect reproduction.

In the unlikely event that the author did not send UMI a complete manuscript and there are missing pages, these will be noted. Also, if unauthorized copyright material had to be removed, a note will indicate the deletion.

Oversize materials (e.g., maps, drawings, charts) are reproduced by sectioning the original, beginning at the upper left-hand corner and continuing from left to right in equal sections with small overlaps.

ProQuest Information and Learning
300 North Zeeb Road, Ann Arbor, MI 48106-1346 USA
800-521-0600

MATHEMATICAL SIMULATION OF PROPAGATED ELECTRICAL EXCITATION IN THE HUMAN VENTRICULAR MYOCARDIUM

By

Clyde Jeffory Clements

SUBMITTED IN PARTIAL FULFILLMENT OF THE
REQUIREMENTS FOR THE DEGREE OF
DOCTOR OF PHILOSOPHY
AT
DALHOUSIE UNIVERSITY
HALIFAX, NOVA SCOTIA
SEPTEMBER 2005

0-494-08409-X

Library and Archives Canada

Published Heritage Branch

395 Wellington Street
Ottawa ON K1A 0N4
Canada

Bibliothèque et Archives Canada

Direction du Patrimoine de l'édition

395, rue Wellington
Ottawa ON K1A 0N4
Canada

Your file *Votre référence*
ISBN:
Our file *Notre reference*
ISBN:

DALHOUSIE UNIVERSITY

To comply with the Canadian Privacy Act the National Library of Canada has requested that the following pages be removed from this copy of the thesis:

Preliminary Pages

Examiners Signature Page (pii)

Dalhousie Library Copyright Agreement (piii)

Appendices

Copyright Releases (if applicable)

In memory of

Clyde Vincent

Lost at sea

February 18, 1966

Age 32 years

Table of Contents

List of Tables

List of Figures

Abstract

Mathematical models for simulating the electrical propagation phenomena in the heart can provide valuable insight into the normal and pathological process of cardiac depolarization and repolarization. Using a model based on anisotropic bidomain theory and a physiologically accurate transmembrane ionic current term, we investigated action-potential propagation in one-, two-, and three-dimensional domains representing the ventricular myocardium. The model of the current flow in cardiac tissue consisted of two coupled partial differential equations for the bidomain case, or a single partial differential equation for the reduced monodomain case. Additionally coupled to this was a system of nonlinear ordinary differential equations that determine the time-varying ionic current at each point in the domain. The total ionic current was described by a realistic membrane model that employs Hodgkin-Huxley formalism to reconstruct the cardiac action potential. A novel approach for the numerical solution of these equations was developed based on the method of lines: the partial differential equations were discretized in space and the resultant differential-algebraic equations were then solved using the robust numerical software package DASPK.

In a three-dimensional bidomain block of human ventricular myocardium, we investigated the propagation of excitation under assumption of equal and unequal anisotropy ratio—to answer the question of whether the former adequately describes physiological characteristics of ventricular myocardium. The simulations demonstrated the sensitivity of the spread of activation and potential time courses and distributions to the underlying electrical properties of cardiac tissue.

We explored the basis for electrocardiographic waveforms using a bidomain model incorporating transmural electrical heterogeneity. The simulations demonstrated that a T wave with the same polarity as the QRS complex can be generated by a model of cardiac tissue that includes the three cell types: endocardial, M cell, and epicardial. Of key importance in generating a "correct" T wave was the presence of a transmural dispersion of *repolarization*. Furthermore, it was observed that a J wave is produced by the heterogeneous distribution of the transient outward current, I_{to}, across the ventricular wall.

The model has been shown to be a useful representation of human ventricular myocardium for experimental data of activation under normal conditions. A uniqueness of this model is its ability to simulate—by virtue of having physiologically accurate description of transmembrane ionic currents—the effect of therapeutic drugs.

Symbols and Abbreviations

Symbols

a	the scalar a
$\boldsymbol{a}$	the vector $\boldsymbol{a}$
A	the matrix A
A^T	transpose of the matrix A
A^{-1}	inverse of the matrix A
a	radius of fiber (cm)
b	radius of volume conductor (cm)
l	length of fiber/volume conductor (cm)
r_e	interstitial resistance per unit length (kΩ/cm)
r_i	intracellular resistance per unit length (kΩ/cm)
ρ	intrinsic resistivity of fiber (k$\Omega \cdot$ cm)
A_e	interstitial cross-sectional area (cm^2)
A_i	intracellular cross-sectional area (cm^2)
A_{tot}	total cross-sectional area (cm^2)
Φ_e	interstitial potential (mV)
Φ_i	intracellular potential (mV)
I_e	interstitial axial current (μA)
I_i	intracellular axial current (μA)
i_m	transmembrane current per unit length (μA/cm)
I_m	transmembrane current per unit area (μA/cm^2)
i_{eapp}	interstitially applied current per unit length (μA/cm)
i_{iapp}	intracellularly applied current per unit length (μA/cm)
I_{app}	applied current per unit of membrane area (μA/cm^2)
I_{eapp}	interstitially applied current per unit of membrane area (μA/cm^2)

I_{iapp} intracellularly applied current per unit of membrane area ($\mu A/cm^2$)

V_m transmembrane potential (mV)

C_m specific membrane capacitance ($\mu F/cm^2$)

I_{ion} total ionic current ($\mu A/cm^2$)

σ_e interstitial conductivity (mS/cm)

σ_i intracellular conductivity (mS/cm)

g_e interstitial bidomain conductivity (mS/cm)

g_i intracellular bidomain conductivity (mS/cm)

χ surface-to-volume ratio (cm^{-1})

Generic Action-Potential Parameters

I_s transmembrane current per unit area generated by an ionic species s as it passes through its respective channel ($\mu A/cm^2$)

G_s conductance of channel (mS/cm^2)

$\bar{G}_s$ maximum channel conductance (mS/cm^2)

E_s reversal potential for an ionic species s (mV)

u gating variable (1)

u_∞ steady-state value (1)

τ_u time constant (ms)

α_u voltage-dependent rate parameter (ms^{-1})

β_u voltage-dependent rate parameter (ms^{-1})

R gas constant

F Faraday's constant

T temperature (K); usually 310 K (37 °C)

Luo-Rudy Phase-1 Model

I_{Na} fast sodium current ($\mu A/cm^2$)

I_{si}	slow inward current carried primarily by calcium ions ($\mu A/cm^2$)
I_K	time-dependent potassium current ($\mu A/cm^2$)
I_{K1}	time-independent potassium current ($\mu A/cm^2$)
I_{Kp}	time-independent plateau potassium current ($\mu A/cm^2$)
I_b	time-independent background potassium current ($\mu A/cm^2$)
m	act/inact gate (1)
h	act/inact gate (1)
j	act/inact gate (1)
d	act/inact gate (1)
f	act/inact gate (1)
X	act/inact gate (1)
$[Ca^{2+}]_i$	intracellular calcium concentration (mmol)

Abbreviations

AP	action potential
APD	action potential duration
CPU	central processing unit
DAE	differential-algebraic equation
GMRES	generalized minimal residual
LR1	Luo-Rudy phase-1 membrane model
LR2	Luo-Rudy phase-2 membrane model
ODE	ordinary differential equation
PDE	partial differential equation

Acknowledgements

It is my pleasure to acknowledge all staff, faculty and fellow graduate students in the Department of Physiology & Biophysics at Dalhousie University, who have contributed to making my graduate work in the Department a positive experience. Most of all, I would like to thank my supervisors, Drs. B. Milan Horáček and John C. Clements, for their guidance and unflagging support throughout the tenure of my graduate studies.

During my tenure as a graduate student, I have been supported by the Faculty of Graduate Studies of Dalhousie University, and by research grants awarded to Drs. Horáček and Clements by the Canadian Institutes of Health Research (CIHR), the Nova Scotia Heart & Stroke Foundation, and the Natural Sciences and Engineering Research Council of Canada (NSERC). The full extent of the work would not have been possible without the support of these granting agencies.

Last but not least, I thank my wife Doreen who has been so patient, supportive, encouraging and understanding through this long process.

Chapter 1

Introduction

Models of electrical propagation in the heart can yield valuable insight into normal and pathological processes of cardiac depolarization and repolarization.[1] Mathematical models that have been developed for simulating action-potential propagation in cardiac tissue can be divided into two broad classes. One utilizes a cellular automaton; the other, a reaction-diffusion system. A cellular automaton simulates the cardiac electrical activity descriptively as a series of discrete states, with each cell beginning in some initial state, and then, according to a transition rule, being assigned a new one based on its current state and that of its neighbours. The primary advantage of this method is its speed and computational simplicity; one of its serious limitations is that it cannot easily incorporate or describe the complex physiological phenomena associated with the action potential of cardiac tissue. For a survey of this modelling approach the reader is referred to Plonsey and Barr [57].

A reaction-diffusion system results from the theoretical consideration of the structural properties of cardiac tissue and of the flow of electric current in excitable cells. This method can therefore simulate the electrical activity with a high degree of accuracy and realism, accounting for those physiological properties that a cellular-automata system cannot. However, the modelling by means of this approach is typically governed by nonlinear partial differential equations (PDEs). This makes the problem computationally complex, and until recently, simulations were restricted to one- and two-dimensional 'slabs' of ventricular muscle and ran through only one activation sequence. For examples of application of reaction-diffusion systems in three-dimensional media, see Colli Franzone and Guerri [17] or Vigmond and Leon [85].

[1] Hereafter, we will use the term excitation to refer summarily to the entire depolarization-repolarization cycle.

Other approaches to the mathematical modelling of propagation in excitable media are also worth mentioning. Colli Franzone and Guerri [17] have applied singular-perturbation techniques to a reaction-diffusion system, which yielded eikonal equations that track the propagating wave front. Similarly, Keener [39] has developed a hybrid model based on an eikonal-curvature equation that describes the wave-front motion. As well, Horáček et al [37] have developed a hybrid model in which a cell's transmembrane potential is governed by a single nonlinear PDE until it reaches a threshold value; after this, the cell's behaviour is modelled by a cellular automaton. These methods have the advantage of describing complex phenomena while reducing the computational complexity of the problem and so allow one to simulate activation sequences in a large block of cardiac tissue. Advantages of the various simplified methods notwithstanding, a full implementation of the reaction-diffusion system is still highly desirable as a 'yardstick' against which the other, simplified models can be tested.

1.1 Objectives

The primary goal of this thesis is to gain an improved understanding of action-potential propagation in the ventricular myocardium. This is undertaken through application of mathematical modelling which then allows us to simulate the process on a computer. To meet our goal, the mathematical model and resultant simulations must be as realistic as possible, and should therefore include such important features as

(A) a three-dimensional geometry of ventricular muscle;

(B) physiologically accurate formulation of the transmembrane action potential in terms of the ionic currents; and

(C) anatomically accurate properties of cardiac tissue such as fiber rotation and anisotropy.

Ideally, (A) should be the actual geometry of the ventricles. However, in this study we consider a simplified slab model of the ventricular myocardium. For (B) we

use the Luo-Rudy phase-1 [43] and Bernus [7] models of ventricular cardiac action potentials, which are based on Hodgkin-Huxley type formalism for describing the gating of ionic currents [35]. Application of bidomain theory allows to us incorporate (C).

The specific objectives of the thesis are:

(i) to review the current literature regarding action-potential (AP) models for cell membrane dynamics in cardiac tissue;

(ii) to review the derivation of isolated monodomain and anisotropic bidomain models for the propagation of excitation in cardiac tissue, as well as to derive a new isolated bidomain model which incorporates capillary capacitance in the extracellular cardiac domain. All of these models will include one of the AP models reviewed in (i) to define the cardiac cell membrane dynamics.

(iii) to use an alternating-direction implicit (ADI) numerical scheme to solve the isolated monodomain model for a rectangular slab of cardiac tissue. This will provide a benchmark and test-bed for the more complex numerical methods to be developed in the thesis. While extremely easy to implement and computationally efficient, ADI methods are restricted in practice to rectangular geometries and simple boundary conditions.

(iv) to develop parallelized computational software for simulating propagation of excitation in the anisotropic bidomain models using a method-of-lines approach and employing the computational software package DASPK. The significant advantages of an implementation using DASPK versus the ADI method are that it can incorporate general boundary conditions and can be applied to irregular domains such as those required for simulations involving a realistic heart geometry. Parallelization of the computer source code is necessary to ensure reasonable computation times.

(v) to explore the reduction of the isolated bidomain models to more simple formulations and to compare simulation results for the reduced (decoupled) models with the original bidomain models.

(vi) to examine transmural electrical heterogeneity as the basis for electrocardiographic waveforms using the computer programs developed in (iv).

1.2 Overview

In Chapter 2, we review the AP models for ventricular cells and present the derivation of a mathematical model of propagated excitation in cardiac tissue. Application of the anisotropic bidomain theory to describe propagation, coupled with Hodgkin-Huxley type gating equations to represent the AP, leads to the following reaction-diffusion system:

$$C_m \frac{\partial V_m}{\partial t} = \frac{1}{\chi}\nabla \cdot \boldsymbol{D}_i \nabla V_m + \frac{1}{\chi}\nabla \cdot \boldsymbol{D}_i \nabla \Phi_e - I_{ion} + I_{app} \quad x \in H \tag{1.1a}$$

$$\nabla \cdot (\boldsymbol{D}_i + \boldsymbol{D}_e)\nabla \Phi_e + \nabla \cdot \boldsymbol{D}_i \nabla V_m = 0 \quad x \in H \tag{1.1b}$$

$$\frac{\partial u}{\partial t} = w(V_m, u) \tag{1.1c}$$

$$\boldsymbol{n} \cdot \boldsymbol{D}_i(\nabla V_m + \nabla \Phi_e) = 0 \quad x \in \partial H \tag{1.1d}$$

$$\boldsymbol{n} \cdot \boldsymbol{D}_e \nabla \Phi_e = 0 \quad x \in \partial H \tag{1.1e}$$

$$V_m(x, 0) = V_{m0}(x) \tag{1.1f}$$

$$\Phi_e(x, 0) = \Phi_{e0}(x) \tag{1.1g}$$

$$u(x, 0) = u_0(x) \tag{1.1h}$$

where

- $V_m \equiv V_m(x, t)$ and $\Phi_e \equiv \Phi_e(x, t)$ are the membrane and interstitial potentials, respectively;
- u represents the variables of the AP model (for example, gating variables and ionic concentrations);
- $\boldsymbol{D}$ represents a conductivity tensor—a matrix function of the spatial variables that incorporates the anisotropy and realistic fiber rotation; subscripts i and e refer to the intracellular and interstitial media, respectively;
- $I_{ion} \equiv I_{ion}(V_m, u)$ is the total ionic current as calculated by Hodgkin-Huxley type gating equations;

- $I_{app} \equiv I_{app}(x,t)$ is an applied current stimulus used to initiate excitation;
- H represents the ventricular heart volume, and ∂H is the boundary of this region;
- n is the outward unit normal to the surface ∂H.

With the assumption of an equal anisotropy ratio, the coupled parabolic and elliptic PDEs reduce to a single parabolic PDE. In Chapter 3, we develop the numerical methods to solve this reduced *monodomain* model using an ADI scheme. In Chapter 4, we develop the numerical methods to solve the *bidomain* model in its fully coupled form using the method of lines. We present in Chapter 5, a formulation of the monodomain model that does not depend on the assumption of an equal anisotropy ratio, and compare the results from this new model with that of the bidomain model. In Chapter 6, we investigate the basis of the electrocardiographic (ECG) waveforms using the bidomain model. Finally, in Chapter 7 we give some conclusions and directions for future work.

Chapter 2

Theory

In this chapter, we present the theory that allows us to derive a mathematical model of the electrical activity of the heart. Simultaneously computing the electric potentials both within the heart and outside of it (e.g., on the torso) is computationally challenging. This problem is therefore split into two subproblems. The first subproblem deals solely with the propagation of action potentials within the myocardium. The second subproblem then deals with computation of the extracardiac potential, given that the propagated behaviour is now known.

We begin in Section 2.1 with an overview of the theory of action-potential modelling, and then move on to propagated behaviour. Before diving into the complex 3-D case, where inclusion of anisotropy and fiber architecture (such as curvature and rotation) complicates the picture, we consider in Section 2.2 the simple 1-D case of a single cylindrical fiber. Application of cable theory yields a mathematical model which describes impulse conduction along the fiber. This model is then re-interpreted in terms of bidomain theory. With this groundwork laid, derivation of the 3-D model from bidomain theory is presented in Section 2.3, and can be seen as an extension of the classical cable theory. Section 2.4 deals with the boundary and initial conditions associated with the propagation models, and lastly, we cover the problem of determining the extracardiac potentials in Section 2.5.

2.1 Action-Potential Models

Figure 2.1 shows the electrical circuit for a cell membrane. It is clear from the figure that the total membrane current, I_m ($\mu A/cm^2$), is the sum of a capacitive current

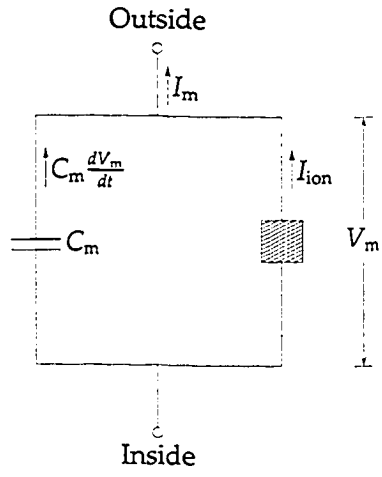

Figure 2.1: Simple electrical circuit model of a cell membrane.

and an ionic current, namely,

$$I_m = C_m \frac{dV_m}{dt} + I_{ion} \tag{2.1}$$

where V_m is the membrane potential (mV), t is time (ms), C_m is the specific membrane capacitance ($\mu F/cm^2$), and I_{ion} represents the total ionic current crossing the membrane per unit area ($\mu A/cm^2$). Note that here we are concerned with a non-propagated, or space-clamped action potential (AP). Therefore, at each instant in time, the membrane potential is uniform over the entire fiber, and there is no net membrane current, except during a stimulus. We thus have

$$C_m \frac{dV_m}{dt} + I_{ion} = I_{app} \tag{2.2}$$

where $I_{app} \equiv I_{app}(t)$ is zero for all t except during the time of a stimulus when it is equal to the externally applied current per unit area ($\mu A/cm^2$). The membrane capacitance is typically regarded as a "biological constant" with $C_m \approx 1\ \mu F/cm^2$ for all biological membranes [15]. The total ionic current is shown as a "black box" in Figure 2.1 because it will vary depending on what exactly is being modelled. In the simplest case, I_{ion} is solely a function of membrane potential, as when considering excitation only (that is, no recovery process is involved). Equation (2.2), with suitably chosen initial conditions, then represents the full model to be solved.

Inclusion of a recovery process, however, means I_{ion} additionally depends on auxiliary variables u; i.e., $I_{\text{ion}} \equiv I_{\text{ion}}(V_{\text{m}}, u)$. Furthermore, the auxiliary variables are governed by a system of ordinary differential equations (ODEs)

$$\frac{du}{dt} = w(V_{\text{m}}, u) \tag{2.3}$$

for some specified function w. Typically, u represents dimensionless gating variables with Hodgkin-Huxley kinetics [35].

2.1.1 The Luo-Rudy Phase-1 Model

The Luo-Rudy phase-1 (LR1) model [43] is a mathematical reconstruction of the ventricular cardiac action potential. It defines I_{ion} as the sum of six ionic currents: I_{Na}, a fast sodium current; I_{si}, a slow inward current carried primarily by calcium ions; I_{K}, a time-dependent potassium current; I_{K1}, a time-independent potassium current; I_{Kp}, a time-independent plateau potassium current; and I_{b}, a time-independent background potassium current. (See Table 1, p. 1503 in [43] for the complete formulation.) In general, the transmembrane current per unit area I_s generated by an ionic species s as it passes through its respective channel is the product of the conductance G_s (mS/cm^2) of the channel, and the difference between the transmembrane potential V_{m} and the reversal potential E_s (mV) for the ion species s. That is,

$$I_s = G_s \cdot (V_{\text{m}} - E_s).$$

The conductance of the channel varies with time and transmembrane potential, and is typically formulated as

$$G_s = \bar{G}_s \cdot g(u_1, u_2, \ldots)$$

where $\bar{G}_s$ is the maximum channel conductance and $u_1, u_2, \ldots$ represent gating parameters. The rate of change of each gating parameter u depends upon its steady-state value u_∞ and its time constant τ_u (ms) as follows

$$\frac{du}{dt} = \frac{u_\infty - u}{\tau_u} \tag{2.4}$$

In turn, the steady-state value and time constant are defined as

$$u_\infty = \frac{\alpha_u}{\alpha_u + \beta_u} \tag{2.5}$$

$$\tau_u = \frac{1}{\alpha_u + \beta_u} \tag{2.6}$$

where α_u (ms^{-1}) and β_u (ms^{-1}) are voltage-dependent rate parameters. In total there are six gating parameters (specifically m, h, j, d, f, and X) which govern the opening and closing of the time-dependent currents of the LR1 model, and each of these is governed by an ODE of the form of equation (2.4). As well, there is an uptake mechanism for the intracellular calcium concentration $[Ca^{2+}]_i$ (mmol); this contributes another ODE to the model. In sum, the LR1 model is described by a system of eight ODEs.

2.1.2 The Luo-Rudy Phase-2 and Subsequent Models

In 1994, Luo and Rudy [44] published an updated AP model, hereafter referred to as the Luo-Rudy phase-2 (LR2) model. This model represents a significant update of the LR1 model; we shall only highlight some of the more important changes. The LR2 model defines eleven sarcolemmal ionic currents and an additional four ionic currents pertaining to the sarcoplasmic reticulim (SR). As before, it includes ionic currents through voltage-gated channels, but also provides currents due to pumps and exchangers (for example, the Na^+-Ca^{2+} exchanger and the Na^+-K^+ pump).

The LR2 model incorporates dynamic changes of ionic concentrations. In general, the rate of concentration change of ion s is given by

$$\frac{d[s]}{dt} = -\frac{I_s \cdot A_{cap}}{V_c \cdot z_s \cdot F} \tag{2.7}$$

where $[s]$ is the concentration of ion s, I_s is the sum of ionic currents carrying ion s, A_{cap} is the capacitive membrane area, V_c is the volume of the compartment where $[s]$ is updated, z_s is the valence of ion s, and F is the Faraday constant.

Lastly, the LR2 model contains an overhaul of the calcium-handling mechanisms. It models Ca^{2+} release from the SR via the Ca^{2+}-induced Ca^{2+}-release (CICR) process and under Ca^{2+}-overload conditions. In addition, it describes buffering of

Ca^{2+} via the major cytosolic (troponin and calmodulin) and SR (calsequestrin) buffers.

As with the previous model, the LR2 model is described by a system of ODEs. In this model, however, there is some choice in the total number of such equations. As mentioned previously, the LR2 model incorporates dynamic ionic concentration changes. If one allows for all ionic species to vary, then the toal number of ODEs is 17. This number can be reduced, though, by holding certain ionic species constant when appropriate. (For example, the extracellular $[Na^+]$ usually does not change significantly throughout the course of an AP.)

Rudy and associates have continued to improve upon the AP model. The present model is now referred to as the Luo-Rudy dynamic (LRd) model. Recent modifications include incoporation of the T-type Ca^{2+} current and two components of the delayed rectifier K^+ current [94], improvement of CICR that yields graded Ca^{2+} release [86], and formulation of a Na^+-activated K^+ current to model Na^+ overload conditions [25]. While the recent additions to the model vastly improve upon the simulated physiology, it comes at a price: a greatly increased computational load. Simulation of a nonpropagated AP poses little problem for todays computing resources, even when considering the most detailed AP model. However, simulation of propagated activity with a comprehensive AP model, particularly 3-D simulations, can be computationally challenging.

2.1.3 FitzHugh-Nagumo Models

Rather than display accurate *quantitative* properties of nerve impulses, FitzHugh [26] developed a simpler model that exhibits *qualitative* physiological behaviour such as excitability and oscillations. FitzHugh started with the van der Pol oscillator as a prototype, then adapted it to nerve impulses to arrive at the following equations

$$\frac{dx}{dt} = c\left[y + x - \frac{x^3}{3} + z(t)\right] \tag{2.8}$$

$$\frac{dy}{dt} = -\frac{x - a + by}{c} \tag{2.9}$$

where x is the excitability of the system, y is the recovery variable, $z(t)$ is an applied stimulus, and a, b, and c are suitably-chosen constants. The variable x can be

identified with membrane potential, while y represents the combined forces that draw membrane to rest.

Similar work was done independently by Nagumo et al [47] and thus today models derived from this work are referred to as a FitzHugh-Nagumo (FN) model. In general terms, we define an FN model as a system of two ODEs

$$\frac{dv}{dt} = I_{\text{app}} - i(v,u) \tag{2.10}$$

$$\frac{du}{dt} = w(v,u) \tag{2.11}$$

where v is the excitability variable, u is the recovery variable, $i(v,u)$ is a function that is normally cubic in v, and $w(v,u)$ is some specified recovery function.

Though only a caricature of the neural excitation process, the FN model has been adapted and used extensively. Its simplicity allows it to be programmed quickly and used successfully in 3-D simulations of propagated activity where the CPU time for other detailed AP models would be prohibitive. In the remainder of this section, we present some variants of the FN model that have been adapted to cardiac cells.

Colli Franzone and Guerri [17] used the following formulation:

$$i(v_{\text{m}}) = Gv_{\text{m}}\left(1 - \frac{v_{\text{m}}}{v_{\text{th}}}\right)\left(1 - \frac{v_{\text{m}}}{v_{\text{p}}}\right) \tag{2.12}$$

where v_{m} is the deviation of the membrane potential from rest, G is the maximum membrane conductance per unit area of the surface membrane, v_{th} is the threshold potential value, and v_{p} is the plateau potential value. This model totally disregards the recovery process—there is no recovery variable u or recovery function w. As such this model only describes the depolarization phase, but it is still appropriate for simulations where the effects of repolarization can be neglected or are not of interest.

Pertsov et al [51] used the following FN variant

$$i(v,u) = -F(v) + u \tag{2.13}$$

$$w(v,u) = \frac{v-u}{\tau(v)} \tag{2.14}$$

where the functions $F(v)$ and $\tau(v)$ are defined as

$$F(v) = \begin{cases} -c_1 v & \text{if } v < e_1 \\ c_2(v-a) & \text{if } e_1 \le v \le e_2 \\ -c_3(v-1) & \text{if } v > e_2 \end{cases} \tag{2.15}$$

$$\tau(v) = \begin{cases} \tau_1 & \text{if } v < b_1 \\ \tau_2 & \text{if } b_1 \le v \le b_2 \\ \tau_3 & \text{if } v > b_2 \end{cases} \tag{2.16}$$

Rogers and McCulloch [63] proposed the following model

$$i(v,u) = c_1 v(v-a)(v-1) + c_2 vu \tag{2.17}$$

$$w(v,u) = b(v-du) \tag{2.18}$$

Note that equation (2.17) differs from the 'standard' FN system in that the last term has been multiplied by v. A transient hyperpolarization during the recovery phase is characteristic of the standard FN system; the above modification prevents this and thereby produces a more physiological action-potential waveform [62].

Henriquez and colleagues [34, 46] have developed the following FN model

$$i(v_m,u) = 0.5v_m\left(1-\frac{v_m}{5.0}\right)\left(1-\frac{v_m}{100.0}\right) + 0.02v_m u \tag{2.19}$$

$$w(v_m,u) = 0.015\,(v_m - 0.005u) \tag{2.20}$$

where v_m is the deviation of the membrane potential from rest.

2.1.4 Bernus Model

In 2002, Bernus et al [7] published a model of a human ventricular AP that emphasized computational efficiency and stability. It came about as a reduction of the Priebe-Beuckelmann (PB) model [59], which itself is based on the LRd models. In short, the Bernus model incorporates nine ionic currents, including the Na^+-Ca^{2+} exchanger and Na^+-K^+ pump currents, but lacks any ionic concentration handling. It is comprised of a system of just seven ODEs; the complete equations for this model are given in Appendix B.

Though much less complex than the LRd-based models, the Bernus model still retains important properties such as AP shape, restitution, and AP heterogeneity. With regards to the last property, the model has configurations for three cell types: endocardial, midmyocardial (M cell), and epicardial. Another important feature of the Bernus model is its stablity. Comprehensive models like the PB model are intrinsically unstable, exhibiting problems such as drift of ionic concentrations in long-running simulations. The Bernus model does not suffer from these defects.

2.2 One-Dimensional Propagation Models: Cable Theory

Consider a uniform cylindrical fiber of radius a and length l lying within a restricted cylindrical volume conductor of radius b as shown in Figure 2.2(a). We assume axial symmetry; moreover, the flow of current is assumed to be confined to the axial direction only. The corresponding electrical circuit for this fiber is shown in Figure 2.2(b). This is the linear core-conductor model [15, 36, 38, 58, 61].

A homogeneous conducting material (such as the intracellular or interstitial media) may be characterized by a bulk property called the intrinsic resistivity, denoted ρ (k$\Omega \cdot$ cm). The resistance per unit length, r (kΩ/cm), is then defined as

$$r_{\mathrm{i}} = \frac{\rho_{\mathrm{i}}}{A_{\mathrm{i}}} \tag{2.21}$$

$$r_{\mathrm{e}} = \frac{\rho_{\mathrm{e}}}{A_{\mathrm{e}}} \tag{2.22}$$

where A is the cross-sectional area (cm^2). For the present case of a cylindrical fiber, $A_{\mathrm{i}} = \pi a^2$ and $A_{\mathrm{e}} = \pi(b^2 - a^2)$. The subscripts i and e denote the intracellular and interstitial regions, respectively. According to Ohm's law, the decrease in intracellular potential, Φ_{i} (mV), is

$$\frac{\partial \Phi_{\mathrm{i}}}{\partial x} = -r_{\mathrm{i}} I_{\mathrm{i}} \tag{2.23}$$

and similarly for the interstitial potential, Φ_{e} (mV),

$$\frac{\partial \Phi_{\mathrm{e}}}{\partial x} = -r_{\mathrm{e}} I_{\mathrm{e}} \tag{2.24}$$

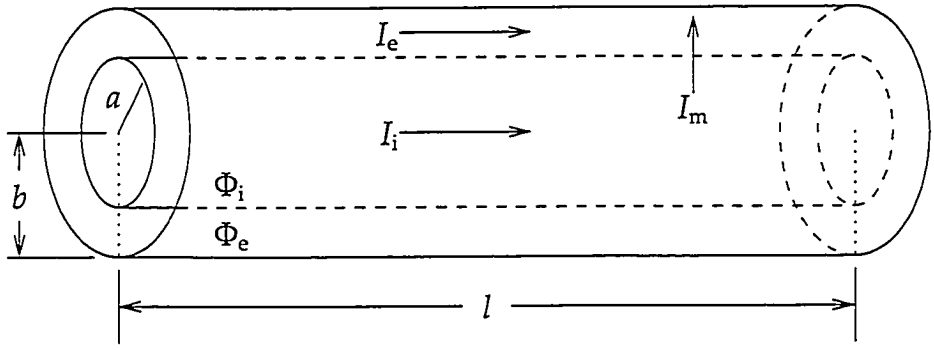

(a)

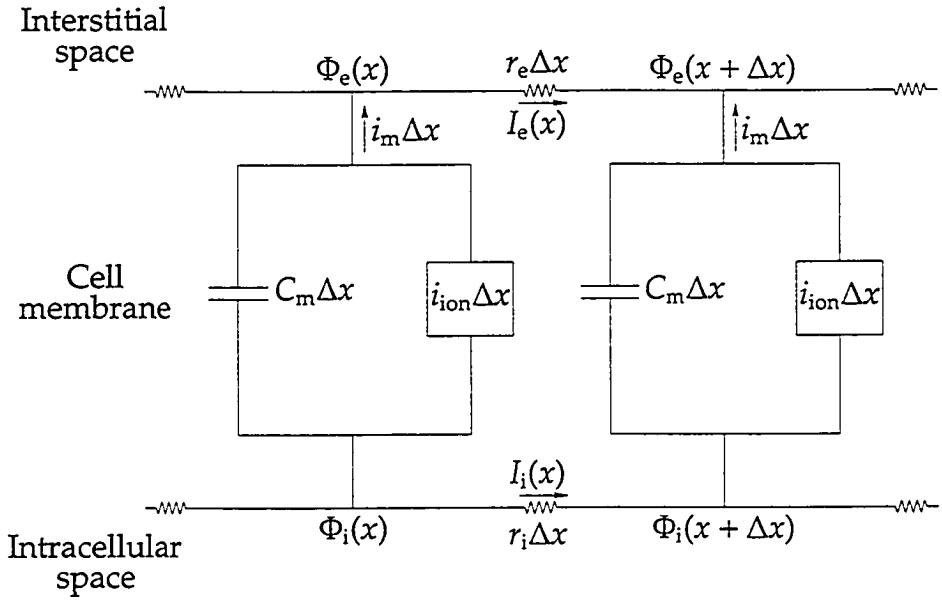

(b)

Figure 2.2: (a) Geometry of a single cylindrical fiber of radius a and length l immersed in a volume conductor of radius b. (b) Equivalent electrical ciruit of a patch of the fiber. Φ represents the potential, I the current, and r the resistance per unit length. Subscripts e, i, and m denote interstitial, intracellular, and membrane regions, respectively.

where I_i and I_e are axial currents (μA) of the intracellular and interstitial regions, respectively. Loss of intracellular current can only occur through current crossing the membrane. Mathematically, this can be stated as

$$\frac{\partial I_i}{\partial x} = -i_m \tag{2.25}$$

where i_m is the transmembrane current per unit length (μA/cm). The transmembrane current is lost to the interstitial space, resulting in a gain there, and thus we have

$$\frac{\partial I_e}{\partial x} = i_m \tag{2.26}$$

To be complete, current can be introduced to the intracellular region through, for example, an electrode. In this case, equation (2.25) becomes

$$\frac{\partial I_i}{\partial x} = -i_m + i_{iapp} \tag{2.27}$$

where i_{iapp} is the external current per unit length (μA/cm) applied to the intracellular space and taken as positive outward. An analogous modification can be made to equation (2.26), if a stimulus is applied to the interstitial medium. We will, however, use equations (2.25) and (2.26), and instead introduce a stimulus via an alternate means to be discussed shortly.

Differentiating equation (2.23) it follows that

$$\begin{aligned}\frac{\partial I_i}{\partial x} &= \frac{\partial}{\partial x}\left(-\frac{1}{r_i}\frac{\partial \Phi_i}{\partial x}\right) \\ &= -\frac{1}{r_i}\frac{\partial^2 \Phi_i}{\partial x^2}\end{aligned}$$

where we have assumed that r_i is constant. Combining this result with equation (2.25) gives

$$-\frac{1}{r_i}\frac{\partial^2 \Phi_i}{\partial x^2} = -i_m \tag{2.28}$$

In a similar fashion, we can derive

$$-\frac{1}{r_e}\frac{\partial^2 \Phi_e}{\partial x^2} = i_m \tag{2.29}$$

The membrane potential, V_m (mV), is defined as

$$V_m = \Phi_i - \Phi_e \tag{2.30}$$

from which it clearly follows that

$$\frac{\partial V_m}{\partial x} = \frac{\partial \Phi_i}{\partial x} - \frac{\partial \Phi_e}{\partial x} \tag{2.31}$$

$$\frac{\partial^2 V_m}{\partial x^2} = \frac{\partial^2 \Phi_i}{\partial x^2} - \frac{\partial^2 \Phi_e}{\partial x^2} \tag{2.32}$$

Using equations (2.28) and (2.32) we obtain

$$-\frac{1}{r_i}\frac{\partial^2 V_m}{\partial x^2} - \frac{1}{r_i}\frac{\partial^2 \Phi_e}{\partial x^2} = -i_m \tag{2.33}$$

and adding this to equation (2.29) gives (after rearranging terms)

$$\left(\frac{1}{r_i} + \frac{1}{r_e}\right)\frac{\partial^2 \Phi_e}{\partial x^2} = -\frac{1}{r_i}\frac{\partial^2 V_m}{\partial x^2} \tag{2.34}$$

The transmembrane current per unit *area*, I_m ($\mu A/cm^2$), is related to i_m as follows

$$i_m = P_m I_m \tag{2.35}$$

where P_m is the perimeter of a cross-section of fiber. (In the case of a cylindrical fiber, $P_m = 2\pi a$.) Recall from Section 2.1 that I_m is the sum of a capacitive current and the total current due to the flow of ions across the membrane:

$$I_m = C_m \frac{\partial V_m}{\partial t} + I_{ion}$$

In this equation, we now introduce a stimulus term so that it becomes

$$I_m = C_m \frac{\partial V_m}{\partial t} + I_{ion} - I_{app} \tag{2.36}$$

where I_{app} is the transmembrane injected current ($\mu A/cm^2$). Combining equations (2.33), (2.35) and (2.36), we obtain

$$P_m\left(C_m \frac{\partial V_m}{\partial t} + I_{ion} - I_{app}\right) = \frac{1}{r_i}\frac{\partial^2 V_m}{\partial x^2} + \frac{1}{r_i}\frac{\partial^2 \Phi_e}{\partial x^2} \tag{2.37}$$

Equations (2.34) and (2.37), together with a formulation for I_{ion} and appropriate auxiliary conditions, describe the propagation of electrical activity along a cylindrical fiber and are known as cable equations [32, 38, 58]. However, we will not use this form of the equations; instead, we will convert them to a more "familiar" form.

2.2.1 Alternative Formulation: A Bidomain Approach

Bidomain theory is typically used to describe propagation of electrical activity in two or three dimensions (see Section 2.3). However, we can still rewrite the equations for one-dimensional propagation in terms of bidomain parameters. This will allow for better comparison of equations in one dimension to those in two and three dimensions.

First we define the intracellular and interstitial conductivities, σ (mS/cm), to be

$$\sigma_i = \frac{1}{\rho_i} \tag{2.38}$$

$$\sigma_e = \frac{1}{\rho_e} \tag{2.39}$$

Recall that $r = \rho/A$ and so we have

$$r_i = \frac{1}{A_i \sigma_i} \tag{2.40}$$

$$r_e = \frac{1}{A_e \sigma_e} \tag{2.41}$$

Substituting this into equations (2.34) and (2.37), and dividing through by the total cross-sectional area, A_{tot} (cm^2), gives

$$\frac{P_m}{A_{tot}} \left(C_m \frac{\partial V_m}{\partial t} + I_{ion} - I_{app} \right) = \frac{A_i \sigma_i}{A_{tot}} \frac{\partial^2 V_m}{\partial x^2} + \frac{A_i \sigma_i}{A_{tot}} \frac{\partial^2 \Phi_e}{\partial x^2} \tag{2.42}$$

$$\left(\frac{A_i \sigma_i}{A_{tot}} + \frac{A_e \sigma_e}{A_{tot}} \right) \frac{\partial^2 \Phi_e}{\partial x^2} = -\frac{A_i \sigma_i}{A_{tot}} \frac{\partial^2 V_m}{\partial x^2} \tag{2.43}$$

The intracellular bidomain conductivity, g_i (mS/cm), is defined as the intracellular conductivity multiplied by the ratio of the volume of the intracellular region to the total tissue volume. Mathematically, this translates into

$$\begin{aligned} g_i &= \frac{A_i l}{A_{tot} l} \sigma_i \\ &= \frac{A_i}{A_{tot}} \sigma_i \end{aligned} \tag{2.44}$$

The interstitial bidomain conductivity, g_e (mS/cm), is defined in a similar manner, and so we have

$$g_e = \frac{A_e}{A_{tot}} \sigma_e \tag{2.45}$$

The surface-to-volume ratio, χ (cm^{-1}), is the ratio of the total membrane area to the total tissue volume; that is,

$$\begin{aligned}\chi &= \frac{P_m l}{A_{tot} l} \\ &= \frac{P_m}{A_{tot}}\end{aligned} \tag{2.46}$$

Finally, substituting the relations in (2.44) to (2.46) into equations (2.42) and (2.43) yields

$$\chi\left(C_m\frac{\partial V_m}{\partial t} + I_{ion} - I_{app}\right) = g_i\frac{\partial^2 V_m}{\partial x^2} + g_i\frac{\partial^2 \Phi_e}{\partial x^2} \tag{2.47}$$

$$(g_i + g_e)\frac{\partial^2 \Phi_e}{\partial x^2} = -g_i\frac{\partial^2 V_m}{\partial x^2} \tag{2.48}$$

To complete the model we need to stipulate boundary and initial conditions; this topic is taken up in Section 2.4.

2.2.2 Simplification to a Monodomain Formulation

Equations (2.47) and (2.48) can be reduced to just one equation in terms of V_m (or Φ_e, if you desire). Simply rewriting equation (2.48) gives

$$\frac{\partial^2 \Phi_e}{\partial x^2} = -\frac{g_i}{g_i + g_e}\frac{\partial^2 V_m}{\partial x^2} \tag{2.49}$$

Substituting this into (2.47) and simplifying, we get[1]

$$\chi\left(C_m\frac{\partial V_m}{\partial t} + I_{ion} - I_{app}\right) = \frac{g_i g_e}{g_i + g_e}\frac{\partial^2 V_m}{\partial x^2} \tag{2.50}$$

[1]Equation (2.50) could have been obtained much quicker. Multiplying equation (2.28) by $\frac{r_i}{r_i+r_e}$ and equation (2.29) by $\frac{r_e}{r_i+r_e}$, and then adding the two gives

$$\frac{1}{r_i + r_e}\left(\frac{\partial^2 \Phi_i}{\partial x^2} - \frac{\partial^2 \Phi_e}{\partial x^2}\right) = i_m$$

Using relations (2.32), (2.35) and (2.36), the above equation can be rewritten as

$$P_m\left(C_m\frac{\partial V_m}{\partial t} + I_{ion} - I_{app}\right) = \frac{1}{r_i + r_e}\frac{\partial^2 V_m}{\partial x^2} \tag{$*$}$$

One can verify that equations ($*$) and (2.50) are equivalent.

2.2.3 Bidomain Formulation Incorporating Capillary Capacitance

We now derive a formulation of the bidomain equations involving a new capacitive term. Let $[x_1, x_2]$ be an arbitrary segment of a uniform cylindrical fiber of radius a (the intracellular region, i) lying within a cylindrical volume conductor of radius b (the interstitial region, e). Let c_e be the interstitial capacitance per unit length (μF/cm), which we identify with the capillary capacitance. Conservation of charge requires that the loss in current flow between x_1 and x_2 must equal the current lost due to the transmembrane current *plus* the current required to charge the section of line between x_1 and x_2. That is,

$$I_e(x_1,t) - I_e(x_2,t) \equiv -\int_{x_1}^{x_2} \frac{\partial I_e}{\partial x}\,dx = \int_{x_1}^{x_2} -i_m\,dx + \int_{x_1}^{x_2} c_e \frac{\partial \Phi_e}{\partial t}\,dx$$

$$I_i(x_1,t) - I_i(x_2,t) \equiv -\int_{x_1}^{x_2} \frac{\partial I_i}{\partial x}\,dx = \int_{x_1}^{x_2} i_m\,dx$$

or equivalently,

$$\int_{x_1}^{x_2} i_m\,dx = \int_{x_1}^{x_2} \left(\frac{\partial I_e}{\partial x} + c_e \frac{\partial \Phi_e}{\partial t}\right) dx \tag{2.51}$$

$$\int_{x_1}^{x_2} -i_m\,dx = \int_{x_1}^{x_2} \frac{\partial I_i}{\partial x}\,dx \tag{2.52}$$

Since $[x_1, x_2]$ was arbitrary, it follows that

$$i_m = \frac{\partial I_e}{\partial x} + c_e \frac{\partial \Phi_e}{\partial t} \tag{2.53}$$

$$-i_m = \frac{\partial I_i}{\partial x} \tag{2.54}$$

Note that when the interstitial capacitance is zero, as was assumed in the previous sections, equation (2.53) reduces to (2.26). Equation (2.54) is idential to (2.25) as no capacitive term has been introduced into the intracellular region.

Following the procedure of Section 2.2, we can derive new equations governing V_m and Φ_e:

$$P_m\left(C_m \frac{\partial V_m}{\partial t} + I_{ion} - I_{app}\right) = \frac{1}{r_i}\left(\frac{\partial^2 V_m}{\partial x^2} + \frac{\partial^2 \Phi_e}{\partial x^2}\right) \tag{2.55}$$

$$\left(\frac{1}{r_i} + \frac{1}{r_e}\right)\frac{\partial^2 \Phi_e}{\partial x^2} - c_e \frac{\partial \Phi_e}{\partial t} = -\frac{1}{r_i}\frac{\partial^2 V_m}{\partial x^2} \tag{2.56}$$

Now let us define

$$C_e = \frac{c_e}{P_m} \tag{2.57}$$

where C_e is a capacitance per unit area ($\mu F/cm^2$). Analogous to Section 2.2.1, the equations can be rewritten in terms of bidomain parameters as follows

$$\chi\left(C_m\frac{\partial V_m}{\partial t} + I_{ion} - I_{app}\right) = g_i\left(\frac{\partial^2 V_m}{\partial x^2} + \frac{\partial^2 \Phi_e}{\partial x^2}\right) \tag{2.58}$$

$$(g_i + g_e)\frac{\partial^2 \Phi_e}{\partial x^2} - \chi C_e\frac{\partial \Phi_e}{\partial t} = -g_i\frac{\partial^2 V_m}{\partial x^2} \tag{2.59}$$

The above equations form the basis for the one-dimensional bidomain model with capillary capacitance.

2.3 Three-Dimensional Propagation Models: Bidomain Theory

To derive a simplified, yet realistic model of electrical wave propagation in 3-D cardiac tissue, we apply the *anisotropic bidomain theory* [29, 81]. Let H represent the ventricular heart volume consisting of cylindrical myocardial fibers. We assume that this volume H is an anisotropic bidomain region. That is, H is composed of two inter-penetrating media, the *intracellular* and *extracellular* (or interstitial) media, connected by a continuous cardiac cell membrane—a concept first proposed by Schmitt [69]. Electric potentials and current densities are defined as continuous macroscopic quantities which can be viewed as the average of the corresponding quantity taken over many cells. Furthermore, electrical conductivities are assumed to be anisotropic: the electrical conductivity is the same in any direction perpendicular to the fiber axis (hereafter called the *transverse* fiber direction), but differs from that measured along any direction parallel with the fiber axis (referred to as the *longitudinal* fiber direction).

Let $j_i = [j_{i,1}, j_{i,2}, j_{i,3}]^T$ represent the intracellular current density ($\mu A/cm^2$) and D_i, the intracellular conductivity tensor (each element of which has units of mS/cm), In the most general case, D_i is a full 3×3 matrix and is a function of the position $x = [x_1, x_2, x_3]^T$. From Ohm's law we have

$$j_i = -D_i \nabla \Phi_i \tag{2.60}$$

where Φ_i is the intracellular potential (mV). For the interstitial domain, a corresponding relationship holds

$$j_e = -D_e \nabla \Phi_e \tag{2.61}$$

Loss of intracellular current can only occur through current crossing the membrane, and so we have

$$\nabla \cdot j_i = -I_{m,v} \tag{2.62}$$

where $I_{m,v}$ is the transmembrane current per unit volume ($\mu A/cm^3$). The transmembrane current is lost to the interstitial space, resulting in a gain there:

$$\nabla \cdot j_e = I_{m,v} \tag{2.63}$$

Taking the divergence of both sides of equation (2.60) yields

$$\nabla \cdot j_i = -\nabla \cdot D_i \nabla \Phi_i \tag{2.64}$$

and substituting this into equation (2.62) gives

$$-\nabla \cdot D_i \nabla \Phi_i = -I_{m,v} \tag{2.65}$$

In a similar manner we can obtain

$$-\nabla \cdot D_e \nabla \Phi_e = I_{m,v} \tag{2.66}$$

Recall from Section 2.2 that the membrane potential is defined as $V_m = \Phi_i - \Phi_e$ where now $V_m \equiv V_m(x,t)$, $\Phi_i \equiv \Phi_i(x,t)$, and $\Phi_e \equiv \Phi_e(x,t)$. Analogous to equation (2.31), it follows that

$$\nabla V_m = \nabla \Phi_i - \nabla \Phi_e \tag{2.67}$$

From this and equation (2.65) we obtain

$$-\nabla \cdot D_i(\nabla V_m + \nabla \Phi_e) = -I_{m,v} \tag{2.68}$$

and adding this to equation (2.66) gives

$$-\nabla \cdot D_i(\nabla V_m + \nabla \Phi_e) - \nabla \cdot D_e \nabla \Phi_e = 0$$

or equivalently,

$$\nabla \cdot (D_i + D_e) \nabla \Phi_e = -\nabla \cdot D_i \nabla V_m \tag{2.69}$$

The transmembrane current per unit area, I_m $\mu A/cm^2$, is related to $I_{m,v}$ as follows

$$I_{m,v} = \chi I_m \tag{2.70}$$

where χ is the surface-to-volume ratio. Recall equation (2.36) from Section 2.2

$$I_m = C_m \frac{\partial V_m}{\partial t} + I_{ion} - I_{app}$$

Substituting this and relation (2.70) into equation (2.68) gives (after some rearranging)

$$\chi\left(C_m \frac{\partial V_m}{\partial t} + I_{ion} - I_{app}\right) = \nabla \cdot \boldsymbol{D}_i \nabla V_m + \nabla \cdot \boldsymbol{D}_i \nabla \Phi_e \tag{2.71}$$

This and equation (2.69), together with appropriate initial/boundary conditions and a suitable description for I_{ion}, describe the propagation of electrical activity in the heart. Observe that (2.69) and equations (2.71) are merely extensions of the corresponding 1-D counterparts: equations (2.47) and (2.48).

2.3.1 Assumption of an Equal Anisotropy Ratio

For reasons of computational complexity, it is convenient to assume that the ratio of interstitial to intracellular conductivity is the same in all directions; that is,

$$\frac{g_{e,x_1}}{g_{i,x_1}} = \frac{g_{e,x_2}}{g_{i,x_2}} = \frac{g_{e,x_3}}{g_{i,x_3}} \equiv r \tag{2.72}$$

This assumption implies that

$$\boldsymbol{D}_e = r\boldsymbol{D}_i \tag{2.73}$$

From this and equation (2.69) we get

$$\nabla \cdot \boldsymbol{D}_i \nabla \Phi_e = -\frac{1}{1+r} \nabla \cdot \boldsymbol{D}_i \nabla V_m \tag{2.74}$$

Substituting this into equation (2.71) gives

$$\chi\left(C_m \frac{\partial V_m}{\partial t} + I_{ion} - I_{app}\right) = \frac{r}{1+r} \nabla \cdot \boldsymbol{D}_i \nabla V_m \tag{2.75}$$

Thus, the assumption of an equal anisotropy ratio allows us to reduce the system of two coupled PDEs in V_m and Φ_e to just one PDE in V_m.

2.3.2 Bidomain Formulation Incorporating Capillary Capacitance

For the 3-D bidomain model, the formulation incorporating capillary capacitance [76] will result in numerically stable well-posed problems for the Neumann boundary conditions and is given by

$$\chi\left(C_m\frac{\partial V_m}{\partial t}+I_{ion}-I_{app}\right)=\nabla\cdot\boldsymbol{D}_i\nabla V_m+\nabla\cdot\boldsymbol{D}_i\nabla\Phi_e \tag{2.76}$$

$$\nabla\cdot(\boldsymbol{D}_i+\boldsymbol{D}_e)\nabla\Phi_e-\chi C_e\frac{\partial\Phi_e}{\partial t}=-\nabla\cdot\boldsymbol{D}_i\nabla V_m \tag{2.77}$$

The directional dependence of the "bulk" membrane capacitance due to the cell membrane, gap junctions and other microstructures [75] could also be incorporated into the model by replacing C_m in (2.76) by C_{blk} with

$$\begin{aligned}C_{blk}&=C_{blk}(C^t_{blk},C^l_{blk},\nabla V_m,\boldsymbol{a}_l)\\&=\begin{cases}\sqrt{((C^l_{blk})^2-(C^t_{blk})^2)\left(\frac{\nabla V_m\cdot\boldsymbol{a}_l}{\|\nabla V_m\|}\right)^2+(C^t_{blk})^2} & \text{for } \nabla V_m\cdot\boldsymbol{a}_l\neq 0\\ C^t_{blk} & \text{for } \nabla V_m\cdot\boldsymbol{a}_l=0\end{cases}\end{aligned} \tag{2.78}$$

where C^t_{blk} and C^l_{blk} are the "bulk" membrane capacitances in the transverse and longitudinal directions, respectively, and $\boldsymbol{a}_l$ is the local (longitudinal) fiber direction. The study of this extended model will be the focus of future work.

2.4 Boundary and Initial Conditions

We give the initial conditions in a general form as

$$V_m(x,0)=V_{m0}(x) \tag{2.79}$$

$$\Phi_e(x,0)=\Phi_{e0}(x) \tag{2.80}$$

$$u(x,0)=u_0(x) \tag{2.81}$$

where V_{m0}, Φ_{e0}, and u_0 are, as yet, unspecified functions of x. In reality these functions are often just simply constants. For example, we usually assume that all cells are initially at rest, which implies that $V_{m0}\equiv V_{rest}$. (The parameter V_{rest} is a constant that depends on the particular AP model used: it is −84 mV in the LR1 model [43], while in the Bernus model [7] it is −90.2 mV.)

We now our attention to the boundary conditions. The bidomain myocardial region H is surrounded by a volume conductor B. This extracardiac region represents the saline bath of an experimental setup, or the torso and intracardiac blood masses, if modelling the human body. We assume that B is homogeneous and isotropic with a constant conductivity of σ_o. Furthermore, we assume that the interstitial space in the myocardium is contiguous with the extracardiac region. Denoting the potential in B as Φ_o, we thus have

$$\Phi_e = \Phi_o \tag{2.82}$$

on ∂H, the boundary of H. This condition specifies continuity of potential across the interface. Likewise, we must have continuity of the current density:

$$\boldsymbol{n} \cdot (\boldsymbol{j}_i + \boldsymbol{j}_e) = \boldsymbol{n} \cdot \boldsymbol{j}_o \tag{2.83}$$

In the above expression, $\boldsymbol{j}_o$ denotes the current density in B and $\boldsymbol{n}$ is an outward unit normal to the surface ∂H. Analogous to the relations for the intracellular and interstitial current densities (see equations (2.60) and (2.61)), we have

$$\boldsymbol{j}_o = -\sigma_o \nabla \Phi_o \tag{2.84}$$

Equation (2.83) can therefore be rewritten in terms of potential as

$$\boldsymbol{n} \cdot (\boldsymbol{D}_i \nabla \Phi_i + \boldsymbol{D}_e \nabla \Phi_e) = \boldsymbol{n} \cdot \sigma_o \nabla \Phi_o \tag{2.85}$$

A third and final boundary condition is needed; however, this condition has been the subject of controversy and at least three alternatives have been used. Tung [81] proposed that the intracellular current does not cross into the extracardiac domain, namely,

$$\boldsymbol{n} \cdot \boldsymbol{D}_i \nabla \Phi_i = 0 \tag{2.86}$$

With this relation, the boundary condition in (2.85) simplifies to

$$\boldsymbol{n} \cdot \boldsymbol{D}_e \nabla \Phi_e = \boldsymbol{n} \cdot \sigma_o \nabla \Phi_o \tag{2.87}$$

On the other hand, Peskoff [53] and Plonsey [56] suggested that at the myocardial surface the intracellular current density matches the transmembrane current density

$$\boldsymbol{n} \cdot (-\boldsymbol{D}_i \nabla \Phi_i) = I_m \tag{2.88}$$

Adding this to equation (2.85) and using the definition of I_m, we arrive at

$$\boldsymbol{n} \cdot \boldsymbol{D}_e \nabla \Phi_e = \boldsymbol{n} \cdot \sigma_o \nabla \Phi_o + C_m \frac{\partial V_m}{\partial t} + I_{ion} \tag{2.89}$$

In contrast, Colli Franzone and colleagues [16, 18] introduced the notion of a bulk conductivity tensor, $\boldsymbol{D} \equiv \boldsymbol{D}_i + \boldsymbol{D}_e$, to describe the composite intracellular and interstitial medium. They postulated that the current flowing in the bulk tissue is given by $-\boldsymbol{D}\nabla\Phi_e$, and that the current flux across the interface ∂H must match the flux entering the extracardiac region B. Mathematically, this yields the boundary condition

$$\boldsymbol{n} \cdot \boldsymbol{D} \nabla \Phi_e = \boldsymbol{n} \cdot \sigma_o \nabla \Phi_o \tag{2.90}$$

Combining this with equation (2.85), we have a compatibility condition for V_m:

$$\boldsymbol{n} \cdot \boldsymbol{D}_i \nabla V_m = 0 \tag{2.91}$$

The appropriateness of the above boundary conditions has been investigated by others [41, 64, 65]. In particular, Krassowska and Neu [41] started with a microscopic model and then applied a homogenization process and boundary layer analysis to arrive at effective boundary conditions for the macroscopic volume-averaged potentials of the bidomain model. Their rigorous analysis proved, on a theoretical basis, that the intracellular current density is zero on the interface between a syncytial tissue and a surrounding volume conductor. In other words, the boundary condition (2.86) proposed by Tung [81] is the correct one to use. Krassowska and Neu further state the physiological implications of equation (2.91). In order for this condition to hold, cells on the boundary must be *cut* and still maintain normal physiological function. In lieu of this finding, equation (2.91) or the even simpler analogue

$$\boldsymbol{n} \cdot \nabla V_m = 0 \tag{2.92}$$

is still frequently used as a boundary condition, owing to its ease of implementation.

In the present study, we consider only an *isolated* bidomain region H; that is, we exclude the extracardiac volume conductor B. In so doing we assume that $\boldsymbol{n} \cdot \sigma_o \nabla \Phi_o = 0$ on ∂H, which is consistent with the experimental findings of Green

et al [31]. The aforementioned boundary conditions can then be replaced with two equations involving only V_m and Φ_e:

$$n \cdot D_i(\nabla V_m + \nabla \Phi_e) = 0 \tag{2.93}$$

$$n \cdot D_e \nabla \Phi_e = 0 \tag{2.94}$$

It is important to note that the interstitial potential is thus governed by an *elliptic* partial differential equation (2.69) with *Neumann* boundary conditions. As a mathematical consequence, solutions for Φ_e are not unique (or only unique up to an additive constant) [78]. We therefore modify the boundary condition for Φ_e so that it includes a Dirichlet component at some region (even just one point will suffice):

$$n \cdot D_e \nabla \Phi_e = 0 \qquad x \in \partial H_1 \tag{2.95a}$$

$$\Phi_e = 0 \qquad x \in \partial H_2 \tag{2.95b}$$

where $H = \partial H_1 \cup \partial H_2$. For notational convenience, we can combine the above two equations into a single one as follows

$$\alpha(x)\Phi_e + \beta(x) n \cdot D_e \nabla \Phi_e = 0 \tag{2.96}$$

where

$$\alpha(x) = \begin{cases} 0 & \text{for } x \in \partial H_1 \\ 1 & \text{for } x \in \partial H_2 \end{cases} \qquad \beta(x) = \begin{cases} 1 & \text{for } x \in \partial H_1 \\ 0 & \text{for } x \in \partial H_2 \end{cases}$$

The Dirichlet condition ensures uniqueness of Φ_e and corresponds to having a grounding point in an experimental setup.

2.5 Extracardiac Potential

To determine the extracardiac potential, we assume that the bidomain region H is embedded in an isotropic and homogeneous volume conductor of infinite extent. In this case, the conductivity of the extracardiac region is a scalar constant, which we denote by g_o (mS/cm). The electric potential, Φ_o, in the extracardiac region is given by [32]

$$g_o \nabla^2 \Phi_o = \nabla \cdot j_s \tag{2.97}$$

where j_s is the impressed current density. Equation (2.97) is Poisson's equation for which the solution is readily found to be

$$\Phi_o(\boldsymbol{r}) = \frac{1}{4\pi g_o} \int_H \frac{-\nabla' \cdot j_s(\boldsymbol{r}')}{\|\boldsymbol{r} - \boldsymbol{r}'\|} dV' \tag{2.98}$$

where $\boldsymbol{r}$ represents the position vector to the *field* point and $\boldsymbol{r}'$ is the position vector to the *source* point. The prime on the del operator indicates that the gradient is with respect to the source point $\boldsymbol{r}'$. The impressed current density is due to the sources in the cardiac region, namely $j_s = -\boldsymbol{D}_i \nabla V_m$. Thus, the extracardiac potential is determined by

$$\Phi_o(\boldsymbol{r}) = \frac{1}{4\pi g_o} \int_H \frac{\nabla' \cdot \boldsymbol{D}_i \nabla' V_m}{\|\boldsymbol{r} - \boldsymbol{r}'\|} dV' \tag{2.99}$$

Chapter 3

Implementation of Monodomain Model

In this chapter, we present the numerical methods to solve the monodomain model. The solution is obtained via an alternating-direction implicit scheme. This scheme gives rise to sets of tridiagonal systems of equations which are easy to implement and solve.

3.1 Introduction

To reduce the computational complexity of the problem at hand, we make the assumption of an equal anisotropy ratio, as discussed in Section 2.3.1. Under this assumption, the membrane potential V_m is governed by

$$\chi\left(C_m\frac{\partial V_m}{\partial t} + I_{ion} - I_{app}\right) = \frac{r}{1+r}\nabla\cdot\boldsymbol{D}_i\nabla V_m \tag{3.1}$$

This is a nonhomogeneous, quasi-linear, parabolic PDE and it is used in this chapter to describe the propagation of electrical activity in the ventricular myocardium.

To complete the model, we impose initial and boundary conditions. All cells are initially assumed to be at resting potential; therefore,

$$V_m(\boldsymbol{x}, 0) = V_{rest}$$

for all $\boldsymbol{x} \in H$, where for simplicity we specify the initial time to be $t^{(0)} = 0$. The boundary conditions reflect the fact that there is no current flow across the boundary of H and are given by

$$\boldsymbol{n}\cdot\nabla V_m \equiv \frac{\partial V_m}{\partial \boldsymbol{n}} = 0$$

where $\boldsymbol{n}$ is the unit outward normal vector on ∂H, the boundary of H. Thus, the

full mathematical model used in this chapter is

$$\chi\left(C_{\mathrm{m}}\frac{\partial V_{\mathrm{m}}}{\partial t} + I_{\mathrm{ion}} - I_{\mathrm{app}}\right) = \frac{r}{1+r}\nabla \cdot \boldsymbol{D}_{\mathrm{i}}\nabla V_{\mathrm{m}} \tag{3.2}$$

$$\frac{\partial u}{\partial t} = f(V_{\mathrm{m}}, u) \tag{3.3}$$

$$\frac{\partial V_{\mathrm{m}}}{\partial n} = 0 \tag{3.4}$$

$$V_{\mathrm{m}}(x, 0) = V_{\mathrm{rest}} \tag{3.5}$$

$$u(0) = u_0 \tag{3.6}$$

The vector $u = [u_1, \ldots, u_7]^T$ represents the variables of the LR1 model, namely, u_1, u_2, ..., u_6 are gating parameters and $u_7 = [\mathrm{Ca}^{2+}]_{\mathrm{i}}$, the intracellular calcium concentration.

3.2 Numerical Methods

To reduce the mathematical and computational complexity of the problem, we restrict our simulations to a parallelepipedal domain. Specifically, we define the myocardial volume H to be a rectangular box with edges of length L_1, L_2, and L_3:

$$H = \{(x, y, z) \mid 0 \le x \le L_1, 0 \le y \le L_2, 0 \le z \le L_3\}$$

Simulations of the mathematical model involve updating the seven ODEs of the LR1 model at each point in the spatial domain, as well as integrating the parabolic PDE in the membrane potential V_{m}. Six of the seven LR1 variables are gating parameters, where each variable u is governed by the ODE

$$\frac{du}{dt} = \frac{u_\infty(V_{\mathrm{m}}) - u}{\tau_u(V_{\mathrm{m}})} \tag{3.7}$$

We employ the simplifying integration algorithm of Rush and Larsen [67]. Assuming V_{m} to be constant over the time step necessary to update u, then equation (3.7) can be integrated explicitly to yield

$$u(t^{(1)}) = u_\infty - \left(u_\infty - u(t^{(0)})\right)e^{-(t^{(1)} - t^{(0)})/\tau_u}$$

and in general,

$$u(t^{(n+1)}) = u_\infty - \left(u_\infty - u(t^{(n)})\right)e^{-(t^{(n+1)}-t^{(n)})/\tau_u}$$

where $t^{(n)}$ is the value of t at the nth time step. The intracellular calcium concentration is governed by the following ODE:

$$\frac{d[\mathrm{Ca}^{2+}]_\mathrm{i}}{dt} = -10^4 I_\mathrm{si} + 0.07\left(10^4 - [\mathrm{Ca}^{2+}]_\mathrm{i}\right) \tag{3.8}$$

Updating this equation is done by means of a fourth-order Runge-Kutta method.

For the numerical solution of the PDE, we use the Douglas-Brian finite difference scheme [9, 24] with modifications to incorporate the mixed and first-order spatial derivatives of V_m [12]. Equation (3.2) can be rewritten as

$$\frac{\partial V}{\partial t} = c_1\frac{\partial^2 V}{\partial x^2} + c_2\frac{\partial^2 V}{\partial y^2} + c_3\frac{\partial^2 V}{\partial z^2} + c_4\frac{\partial^2 V}{\partial x \partial y} + c_5\frac{\partial^2 V}{\partial x \partial z} + c_6\frac{\partial^2 V}{\partial y \partial z} + c_7\frac{\partial V}{\partial x} + c_8\frac{\partial V}{\partial y} + c_9\frac{\partial V}{\partial z} + f(x, y, z, t, V, \boldsymbol{u})$$

where the m in V_m has been dropped for notational clarity. The coefficients $c_1, c_2, \ldots, c_9$ are functions of the spatial variables (i.e., $c_l \equiv c_l(x, y, z)$), and f represents the current source term. Let Δx, Δy, and Δz denote the spatial step sizes, and Δt, the time step size. We impose a grid on the heart volume H as follows:

$$\begin{aligned}
x^{(i)} &= i \cdot \Delta x, & i &= 0, 1, 2, \ldots, N_1, N_1 + 1 & [\Delta x &= L_1/(N_1 + 1)] \\
y^{(j)} &= j \cdot \Delta y, & j &= 0, 1, 2, \ldots, N_2, N_2 + 1 & [\Delta y &= L_2/(N_2 + 1)] \\
z^{(k)} &= m \cdot \Delta z, & k &= 0, 1, 2, \ldots, N_3, N_3 + 1 & [\Delta z &= L_3/(N_3 + 1)]
\end{aligned}$$

We denote $V(x^{(i)}, y^{(j)}, z^{(k)}, t^{(n)})$ by $V^{(i,j,k,n)}$ and define the central-difference and average operators, δ and μ, respectively, in the usual way as

$$\begin{aligned}
\delta_x V^{(i,j,k,n)} &= V^{(i+1/2,j,k,n)} - V^{(i-1/2,j,k,n)} \\
\mu_x V^{(i,j,k,n)} &= \frac{V^{(i+1/2,j,k,n)} - V^{(i-1/2,j,k,n)}}{2}
\end{aligned}$$

and similarly for δ_y, δ_z, μ_y, and μ_z. Furthermore, let ρ represent mesh ratios such that $\rho_{xx} = \Delta t/(\Delta x)^2$, $\rho_x = \Delta t/\Delta x$ and similarly for other parameters. The values of

the membrane potential V on this grid are then approximated at time $t^{(n+1)}$ from the values of V at time $t^{(n)}$ according to the following finite-difference scheme

$$\left[1-\frac{\rho_{xx}}{2}c_1\delta_x^2\right]V_*^{(n+1)} = \left[1+\frac{\rho_{xx}}{2}c_1\delta_x^2+\rho_{yy}c_2\delta_y^2+\rho_{zz}c_3\delta_z^2+\rho_{xy}c_4\mu_x\delta_x\mu_y\delta_y\right.$$
$$+\rho_{xz}c_5\mu_x\delta_x\mu_z\delta_z+\rho_{yz}c_6\mu_y\delta_y\mu_z\delta_z+\rho_x c_7\mu_x\delta_x$$
$$\left.+\rho_y c_8\mu_y\delta_y+\rho_z c_9\mu_z\delta_z\right]V^{(n)}+\Delta t\cdot f^{(n)} \tag{3.9}$$

$$\left[1-\frac{\rho_{yy}}{2}c_2\delta_y^2\right]V_{**}^{(n+1)} = -\frac{\rho_{yy}}{2}c_2\delta_y^2V^{(n)}+V_*^{(n+1)} \tag{3.10}$$

$$\left[1-\frac{\rho_{zz}}{2}c_3\delta_z^2\right]V^{(n+1)} = -\frac{\rho_{zz}}{2}c_3\delta_z^2V^{(n)}+V_{**}^{(n+1)} \tag{3.11}$$

where the i, j, and k subscripts have been suppressed, so that

$$f^{(n)} = f^{(i,j,k,n)} \equiv f\left(x^{(i)},y^{(j)},z^{(k)},t^{(n)},V^{(i,j,k,n)},\boldsymbol{u}^{(i,j,k,n)}\right)$$

Likewise, $c_1 = c_1^{(i,j,k)} \equiv c_1(x^{(i)},y^{(j)},z^{(k)})$, and similarly for other values. To maintain second-order accuracy in time, the set of equations (3.9)–(3.11) is actually solved twice analogous to a predictor-corrector method. On the first pass, one replaces Δt by $\Delta t/2$ and proceeds with the finite difference scheme, along with the appropriate boundary-value approximations, to obtain a first estimate $\hat{V}^{(i,j,k,n+1/2)}$. Then one uses equation (3.9) with $f^{(n)}$ replaced by

$$\hat{f}^{(n)} = f\left(x^{(i)},y^{(j)},z^{(k)},t^{(n+1/2)},\hat{V}^{(i,j,k,n+1/2)},\boldsymbol{u}^{(i,j,k,n)}\right)$$

together with equations (3.10), (3.11) and suitable boundary value approximations to obtain $V^{(i,j,k,n+1)}$.

We now turn our attention to the boundary-value approximations. As a direct consequence of the boundary condition $\frac{\partial V_m}{\partial n} = 0$, we have

$$\frac{\partial V}{\partial x}(0,y,z,t) = \frac{\partial V}{\partial x}(L_1,y,z,t) = 0. \tag{3.12}$$

Approximating $\frac{\partial V}{\partial x}$ at $x = x^{(0)} = 0$ by means of a centered-difference Taylor series yields

$$\frac{\partial V}{\partial x}(x^{(0)},y^{(j)},z^{(k)},t^{(n)}) \approx \frac{V^{(1,j,k,n)}-V^{(-1,j,k,n)}}{2\cdot\Delta x}$$

and at $x = x^{(NI+1)} = L_1$

$$\frac{\partial V}{\partial x}(x^{(N_1+1)},y^{(j)},z^{(k)},t^{(n)}) = \frac{V^{(N_1+2,j,k,n)}-V^{(N_1,j,k,n)}}{2\cdot\Delta x}$$

Note that this introduces the two "fictitious" points $x^{(-1)}$ and $x^{(N_1+2)}$; that is, points that are outside the domain H. To use the above approximations for $\frac{\partial V}{\partial x}$, one must make the reasonable assumption that V can be extended to satisfy sufficient continuity conditions outside of H. Substituting these results into equation (3.12) thus gives the following order-two approximations (the common index n has been omitted)

$$V^{(-1,j,k)} = V^{(1,j,k)} \tag{3.13}$$

$$V^{(N_1+2,j,k)} = V^{(N_1,j,k)} \tag{3.14}$$

In a like manner, we also obtain the following second-order approximations by applying centered differences to $\frac{\partial V}{\partial y}$ and $\frac{\partial V}{\partial z}$:

$$V^{(i,-1,k)} = V^{(i,1,k)} \tag{3.15}$$

$$V^{(i,N_2+2,k)} = V^{(i,N_2,k)} \tag{3.16}$$

$$V^{(i,j,-1)} = V^{(i,j,1)} \tag{3.17}$$

$$V^{(i,j,N_3+2)} = V^{(i,j,N_3)} \tag{3.18}$$

Returning now to equation (3.9) and including the i, j, and k superscripts gives

$$\begin{aligned}\left[1 - \frac{\rho_{xx}}{2}c_1\delta_x^2\right]V_*^{(i,j,k,n+1)} = \Big[1 &+ \frac{\rho_{xx}}{2}c_1\delta_x^2 + \rho_{yy}c_2\delta_y^2 + \rho_{zz}c_3\delta_z^2 + \rho_{xy}c_4\mu_x\delta_x\mu_y\delta_y \\ &+ \rho_{xz}c_5\mu_x\delta_x\mu_z\delta_z + \rho_{yz}c_6\mu_y\delta_y\mu_z\delta_z + \rho_x c_7\mu_x\delta_x \\ &+ \rho_y c_8\mu_y\delta_y + \rho_z c_9\mu_z\delta_z\Big]V^{(i,j,k,n)} + \Delta t \cdot f^{(i,j,k,n)}\end{aligned} \tag{3.19}$$

If we fix the superscripts j and k—say $j = J$ and $k = K$ with $0 \le J \le N_2 + 1$ and $0 \le K \le N_3 + 1$—and allow the i superscript to range from 0 to $N_1 + 1$, then we obtain the following system of equations:

$$\begin{aligned}
-\frac{\rho_{xx}}{2}V_*^{(-1,J,K,n+1)} &+ (1+\rho_{xx})V_*^{(0,J,K,n+1)} - \frac{\rho_{xx}}{2}V_*^{(1,J,K,n+1)} &&= d^{(0,J,K,n)} \\
-\frac{\rho_{xx}}{2}V_*^{(0,J,K,n+1)} &+ (1+\rho_{xx})V_*^{(1,J,K,n+1)} - \frac{\rho_{xx}}{2}V_*^{(2,J,K,n+1)} &&= d^{(1,J,K,n)} \\
-\frac{\rho_{xx}}{2}V_*^{(1,J,K,n+1)} &+ (1+\rho_{xx})V_*^{(2,J,K,n+1)} - \frac{\rho_{xx}}{2}V_*^{(3,J,K,n+1)} &&= d^{(2,J,K,n)} \\
&\vdots \\
-\frac{\rho_{xx}}{2}V_*^{(N_1-1,J,K,n+1)} &+ (1+\rho_{xx})V_*^{(N_1,J,K,n+1)} - \frac{\rho_{xx}}{2}V_*^{(N_1+1,J,K,n+1)} &&= d^{(N_1,J,K,n)} \\
-\frac{\rho_{xx}}{2}V_*^{(N_1,J,K,n+1)} &+ (1+\rho_{xx})V_*^{(N_1+1,J,K,n+1)} - \frac{\rho_{xx}}{2}V_*^{(N_1+2,J,K,n+1)} &&= d^{(N_1+1,J,K,n)}
\end{aligned}$$

where $d^{(i,J,K,n)}$ is the right-hand side of equation (3.19). We assume that V_* and V_{**} satisfy the boundary condition (3.12), so that the approximations for V in equations (3.13)–(3.18) also hold for V_* and V_{***}. Therefore, the first and last equations in the above system now reduce to

$$\begin{aligned}(1+\rho_{xx})V_*^{(0,J,K,n+1)} - \rho_{xx}V_*^{(1,J,K,n+1)} &= d^{(0,J,K,n)} \\ -\rho_{xx}V_*^{(N_1,J,K,n+1)} + (1+\rho_{xx})V_*^{(N_1+1,J,K,n+1)} &= d^{(N_1+1,J,K,n)}\end{aligned}$$

Hence, we have a tridiagonal system, which can be expressed in matrix notation as

$$A\,V_*^{(n+1)} = d^{(n)}$$

where

$$\begin{aligned}d^{(n)} &= [d^{(0,J,K,n)}, d^{(1,J,K,n)}, \ldots, d^{(N_1+1,J,K,n)}]^T \\ V_*^{(n+1)} &= [V_*^{(0,J,K,n+1)}, V_*^{(1,J,K,n+1)}, \ldots, V_*^{(N_1+1,J,K,n+1)}]^T\end{aligned}$$

and

$$A = \begin{bmatrix} 1+\rho_{xx} & -\rho_{xx} & 0 & 0 & & \cdots & 0 \\ -\frac{\rho_{xx}}{2} & 1+\rho_{xx} & -\frac{\rho_{xx}}{2} & 0 & & \cdots & 0 \\ 0 & -\frac{\rho_{xx}}{2} & 1+\rho_{xx} & -\frac{\rho_{xx}}{2} & & \cdots & 0 \\ & & \ddots & \ddots & \ddots & & \vdots \\ \vdots & & & \ddots & \ddots & \ddots & \\ 0 & \cdots & & & -\frac{\rho_{xx}}{2} & 1+\rho_{xx} & -\frac{\rho_{xx}}{2} \\ 0 & \cdots & & & 0 & -\rho_{xx} & 1+\rho_{xx} \end{bmatrix}.$$

Thus, we compute $V_*^{(i,j,k,n+1)}$ for i, j, and k by solving $(N_2+2)\cdot(N_3+2)$ tridiagonal systems of (N_1+2) equations. Similarly, if we now fix the i and k superscripts and allow the j superscript to range from 0 to N_2+1, then equation (3.10) gives rise to another tridiagonal system of equations

$$A'\,V_{**}^{(n+1)} = d'^{(n)}$$

where

$$\begin{aligned}d'^{(I,j,K,n)} &\equiv -\frac{\rho_{yy}}{2}\delta_y^2 V^{(I,j,K,n)} + V_*^{(I,j,K,n)} \\ d'^{(n)} &= [d'^{(I,0,K,n)}, d'^{(I,1,K,n)}, \ldots, d'^{(I,N_2+1,K,n)}]^T \\ V_{**}^{(n+1)} &= [V_{**}^{(I,0,K,n+1)}, V_{**}^{(I,1,K,n+1)}, \ldots, V_{**}^{(I,N_2+1,K,n+1)}]^T\end{aligned}$$

and A' is the matrix A with ρ_{xx} replaced by ρ_{yy}. In a similar fashion, equation (3.11) results in the tridiagonal system

$$A''\, V^{(n+1)} = d''^{(n)}$$

where

$$\begin{aligned} d''^{(I,J,k,n)} &\equiv -\frac{\rho_{zz}}{2}\delta_z^2 V^{(I,J,k,n)} + V^{(I,J,k,n)}_{**} \\ d''^{(n)} &= [d''^{(I,J,0,n)}, d''^{(I,J,1,n)}, \ldots, d''^{(I,J,N_3+1)}]^T \\ V^{(n+1)} &= [V^{(I,J,0,n+1)}, V^{(I,J,1,n+1)}, \ldots, V^{(I,J,N_3+1,n+1)}]^T \end{aligned}$$

and A'' is the matrix A with ρ_{xx} replaced by ρ_{zz}. Thus, we simultaneously solve for V on the interior of H as well as along the boundary of H.

3.3 Numerical Experiments

3.3.1 Test Problem with Known Solution

To verify the accuracy of the spatial propagation component of the computer code, we used the program to solve a problem that has a known solution. This allowed comparison of the numerical solution with the exact value. Consider the following problem:

$$C_m \frac{\partial V_m}{\partial t} = \frac{r}{\chi(1+r)} \nabla \cdot D_i \nabla V_m + S(x,t) \tag{3.20a}$$

$$\frac{\partial V_m}{\partial n} = 0 \tag{3.20b}$$

$$V_m(x,0) = \prod_{i=1}^{3} \cos\left(\frac{\pi x_i}{L_i}\right) \tag{3.20c}$$

where

$$D_i = \begin{bmatrix} g_{i,x_1} & 0 & 0 \\ 0 & g_{i,x_2} & 0 \\ 0 & 0 & g_{i,x_3} \end{bmatrix}$$

$$S(x,t) = \left[\frac{\pi^2 r}{\chi(1+r)}\left(\sum_{i=1}^{3} \frac{g_{i,x_i}}{L_i^2}\right) - C_m\right] e^{-t} \prod_{i=1}^{3} \cos\left(\frac{\pi x_i}{L_i}\right)$$

The exact solution to this problem is given by

$$V_{\mathrm{m}}(x,t) = e^{-t}\prod_{i=1}^{3}\cos\left(\frac{\pi x_i}{L_i}\right) \tag{3.21}$$

Note that we have maintained the same notation has used earlier in this chapter, however, V_{m} no longer corresponds to membrane potential.

We solved problem (3.20) for $0 \leq t \leq 8$ on the rectangular volume $H = \{(x_1,x_2,x_3) \mid 0 \leq x_1 \leq 0.8, 0 \leq x_2 \leq 0.8, 0 \leq x_3 \leq 0.4\}$ for three uniform meshes: (i) $\Delta x = 0.08$ corresponding to $11 \times 11 \times 6$ grid points; (ii) $\Delta x = 0.04$ corresponding to $21 \times 21 \times 11$ grid points; and (iii) $\Delta x = 0.02$ corresponding to $41 \times 41 \times 21$ grid points. Furthermore, the problem was solved with two different time steps for each mesh: $\Delta t = 0.1$ and $\Delta t = 0.05$. Solution values were output at times $t = 1, 2, \ldots, 8$, and the root-mean-square (RMS) errors and maximum deviations were calculated by the following formulas:

$$\text{RMS error} = \left[\frac{1}{n}\sum_{i=1}^{n}\left(\hat{V}_{\mathrm{m}}^{(i)} - V_{\mathrm{m}}^{(i)}\right)^2\right]^{1/2} \tag{3.22}$$

$$\text{Maximum deviation} = \max_i |\hat{V}_{\mathrm{m}}^{(i)} - V_{\mathrm{m}}^{(i)}| \tag{3.23}$$

where $\hat{V}_{\mathrm{m}}^{(i)}$ is the numerical solution at some "point" i and $V_{\mathrm{m}}^{(i)}$ is the exact value computed by equation (3.21).

Table 3.1 shows the RMS errors and maximum deviations for the monodomain code when solving problem (3.20). As expected, the errors decrease as the spatial and temporal stepsizes are decreased. Also of note, the method developed in Section 3.2 is second-order accurate in both space and time. Therefore, reducing both the spatial and temporal stepsizes by a factor of two should reduce the error by at least a factor of four. One can verify that the errors listed in Table 3.1 indeed follow this relationship, indicating that the code is working as expected.

3.3.2 Block with Rotational Anisotropy

Methods: As a further test of the code, we replicated the 'Block Type I' of Colli Franzone and Guerri [17], which was also previously used by Horáček et al [37].

Table 3.1: RMS errors and maximum deviations for the monodomain code when solving a test problem that has a known solution.

(a) RMS Errors

	Δt	
Δx	0.1	0.05
0.08	0.000260	0.000150
0.04	0.000162	0.000061
0.02	0.000129	0.000038

(b) Maximum Deviations

	Δt	
Δx	0.1	0.05
0.08	0.000664	0.000383
0.04	0.000447	0.000166
0.02	0.000377	0.000110

The block consists of a small myocardial volume representing a 1 cm $\times$ 1 cm $\times$ 0.3 cm portion of the ventricular wall. The z-axis is vertical, and the planes $z = 0$ and $z = 0.3$ represent the endocardial and epicardial surfaces, respectively. The volume of ventricular myocardium, H, is therefore defined as $\{(x, y, z) | 0 \leq x, y \leq 1, 0 \leq z \leq 0.3\}$. We assume that the ventricular wall is composed of uniform layers of muscle fibers parallel with the xy-plane. The curvature of the fibers is neglected and the colatitude angle with respect to the z-axis is $\theta(x, y, z) \equiv \frac{\pi}{2}$. On each layer, the principal fiber direction is fixed but rotates 90° counterclockwise with depth proceeding from top to bottom of the block.

The rotation of the muscle fibers is described by the function

$$\phi(z) = \frac{\pi}{4}\left[-\sin\left(4\pi\left(\frac{z}{0.3} - 0.5\right)^3\right) + 1\right]. \tag{3.24}$$

This fiber rotation function, which depends on the vertical distance only, is an idealized representation of experimental data of Streeter [79] and is the same function used in previous simulations [17, 37]. At the epicardial surface, $\phi = 0$ and so the fiber direction is aligned with the x-axis. At the endocardial surface, $\phi = \frac{\pi}{2}$ and thus the fiber direction coincides with the y-axis.

The volume of tissue in 'Block Type I' was represented by 51 $\times$ 51 $\times$ 19 grid points. Excitation was initiated by applying a current stimulus at the upper layer of the block to 3 $\times$ 3 $\times$ 2 cubic elements for vertex stimulation and 4 $\times$ 3 $\times$ 2 cubic elements for edge stimulation. In particular, three different excitation sequences were elicited by stimulating the right vertex, midpoint of edge, and left vertex

Table 3.2: Propagation parameters for 'Block Type I' simulations. Values for equal anisotropy ratio, membrane capacitance, and intracellular transverse and longitudinal conductivities taken from Horáček et al [37]. Value of surface-to-volume ratio is the same used by Colli Franzone and Guerri [17].

Equal anisotropy ratio r	1.0
Intracellular transverse conductivity σ_t^i	0.5 mS/cm
Intracellular longitudinal conductivity σ_l^i	2.0 mS/cm
Membrane capacitance C_m	0.8 μF/cm^2
Surface-to-volume ratio χ	1000.0 cm^{-1}
Spatial steps	
$hx = hy$	0.020 cm
hz	0.01$\bar{6}$ cm
Time step k	0.02 ms
Current stimulus I_{app}	100.0 μA/cm^2
Duration of stimulus t_{off}	0.5 ms

with an applied current of 100 μA/cm^2 and 0.5 ms duration. A fourth excitation sequence was also initiated by delivering a current stimulus of the same magnitude and duration to $4 \times 4 \times 2$ cubic elements located in the center of the upper layer of the block. The propagation parameters used in all 'Block Type I' simulations are listed in Table 3.2.

To track the action potential propagation throughout the block of ventricular myocardium, we use isochrones of activation. The activation time was defined as the time instant at which the transmembrane potential exceeds -20 mV. Successive isochrones were plotted at 1-ms increments.

All computer programs were written in Fortran 77. The simulations were performed on an IBM RS/6000 model 590 with version 3.1.2 of the IBM XL Fortran compiler.

Results: Figure 3.1 shows the excitation sequences simulated with a time step of 0.02 ms initiated by stimulation of the right vertex (Figure 1a), midpoint of edge (Figure 1b), and left vertex (Figure 1c). Isochrones are displayed for selected

horizontal cross-sections through the block. From top to bottom, the fiber directions in the panels make angles of 0°, 42.4°, 47.6°, and 90°, respectively, relative to the horizontal side of the figures. The block was completely excited within 23–32 ms, and on average, the run time was approximately 90 minutes on an IBM RS/6000 model 590. Figure 3.1 clearly illustrates an asymmetric behaviour of the propagated activation. For right vertex stimulation (column 1), the fiber rotation increases the velocity of wave propagation with the lower left corner of the top layer being excited within 23 ms after the onset of the applied stimulus. Compare this with left vertex stimulation (column 3) where the wave propagation velocity is decreased by fiber rotation, and in contrast, the lower right corner of the top layer is not excited until 32 ms after the applied stimulus. As well, in the lower layers of the block, the curvature of the wavefront is enhanced by fiber rotation for right vertex stimulation which is in stark contrast to left vertex stimulation where there is a flattening of the wavefront. This asymmetric behaviour is also clearly present in the propagated activation for midpoint of edge stimulation where the left and right halves of the activation isochrones approximately resemble right and left vertex stimulations, respectively.

To illustrate the stability and efficiency of our numerical methods, we ran the previous simulations for a time step of 0.1 ms. The results are shown in Figure 3.2. A comparison of this figure with Figure 3.1 shows nearly identical results. The runtime, however, on an IBM RS/6000 model 590 was reduced from 90 minutes in the previous case to a mere 15 minutes for complete block excitation.

To see even more clearly the combined effects of anisotropy and fiber rotation, yet another excitation sequence was initiated by applying a current stimulus to the center of the upper face of the block of tissue. The isochrones of activation are shown in Figure 3.3. Note that the isochrones are ellipsoidal in shape. This is due to the anisotropy: the leading edge of the wavefront moves faster along the fiber direction than in the transverse direction. At the upper layer of the block, the orientation of the major axis of the ellipse coincides with the fiber direction; similarly, the minor axis is aligned with the transverse direction. Also apparent from Figure 3.3 is the rotation of the elliptical shape from top to bottom of the block.

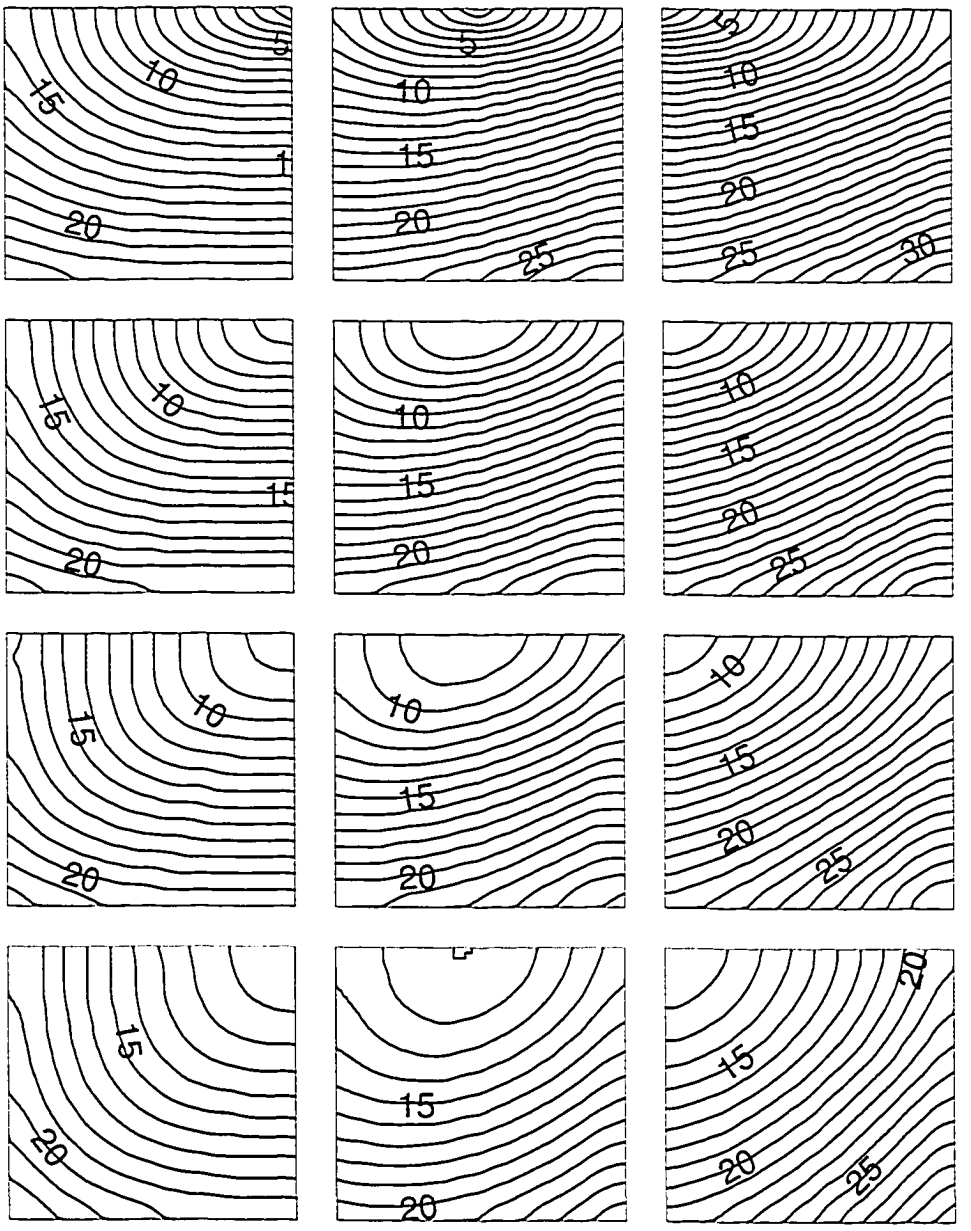

Figure 3.1: Isochrones of propagated excitation for right vertex, midpoint of edge and left vertex stimulation on 51×51×19 nodes representing a 1 cm × 1 cm × 0.3 cm block of tissue. Successive isochrones are displayed at 1 ms intervals and the simulation was run with a time step of 0.02 ms. Layers illustrated here refer to slices through the block parallel with the xy-plane. The top (bottom) layer corresponds to the epi(endo)-cardial surface. From top to bottom, the fiber directions in the panels make angles, relative to the horizontal side of the figures, of 0°, 42.4°, 47.6°, and 90°, respectively. Compare with Figure 2 in [17] and Figure 1 in [37].

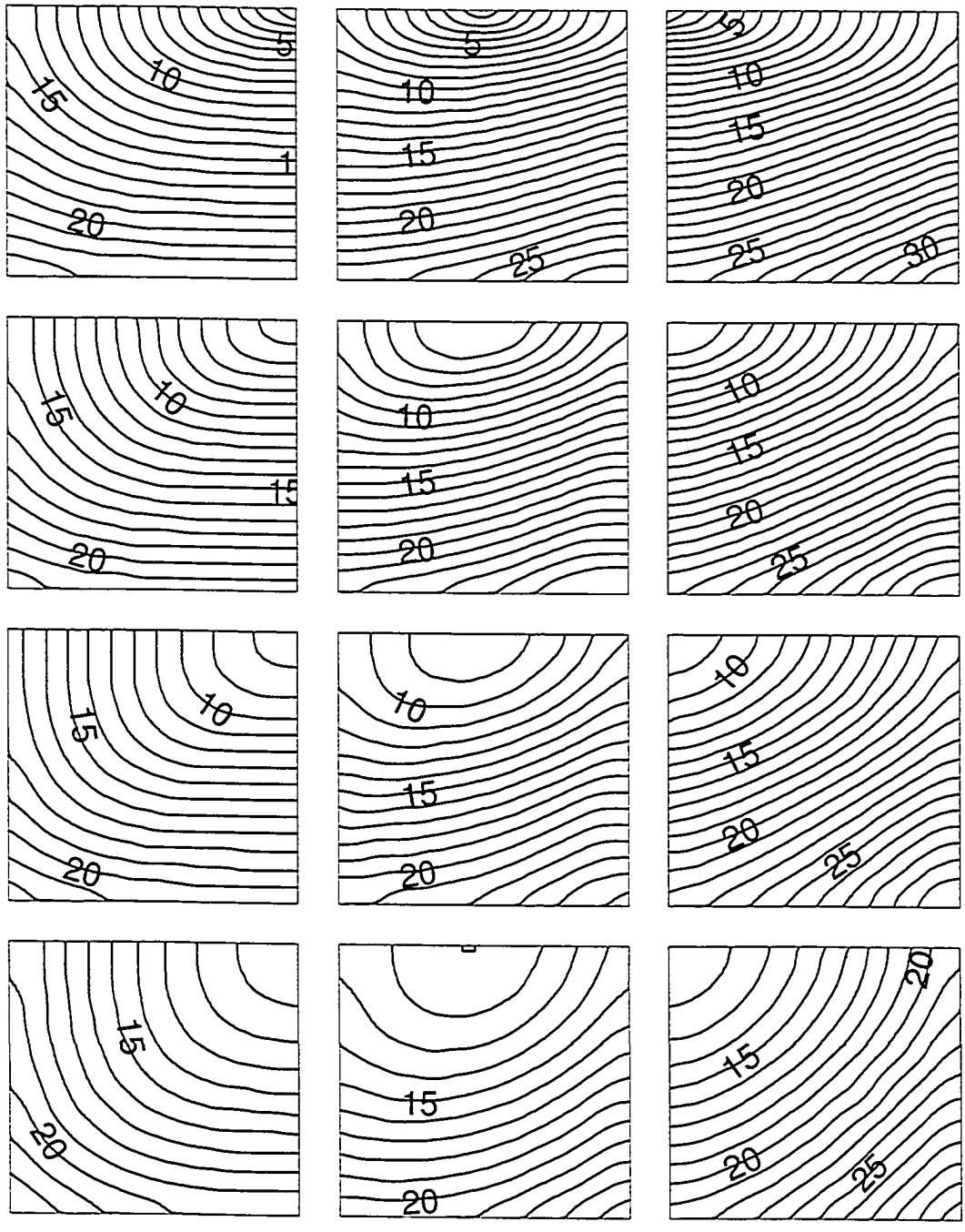

Figure 3.2: Isochrones of propagated excitation for right vertex, midpoint of edge and left vertex stimulation, computed with a time step of 0.1 ms. Same setup as in Figure 3.1.

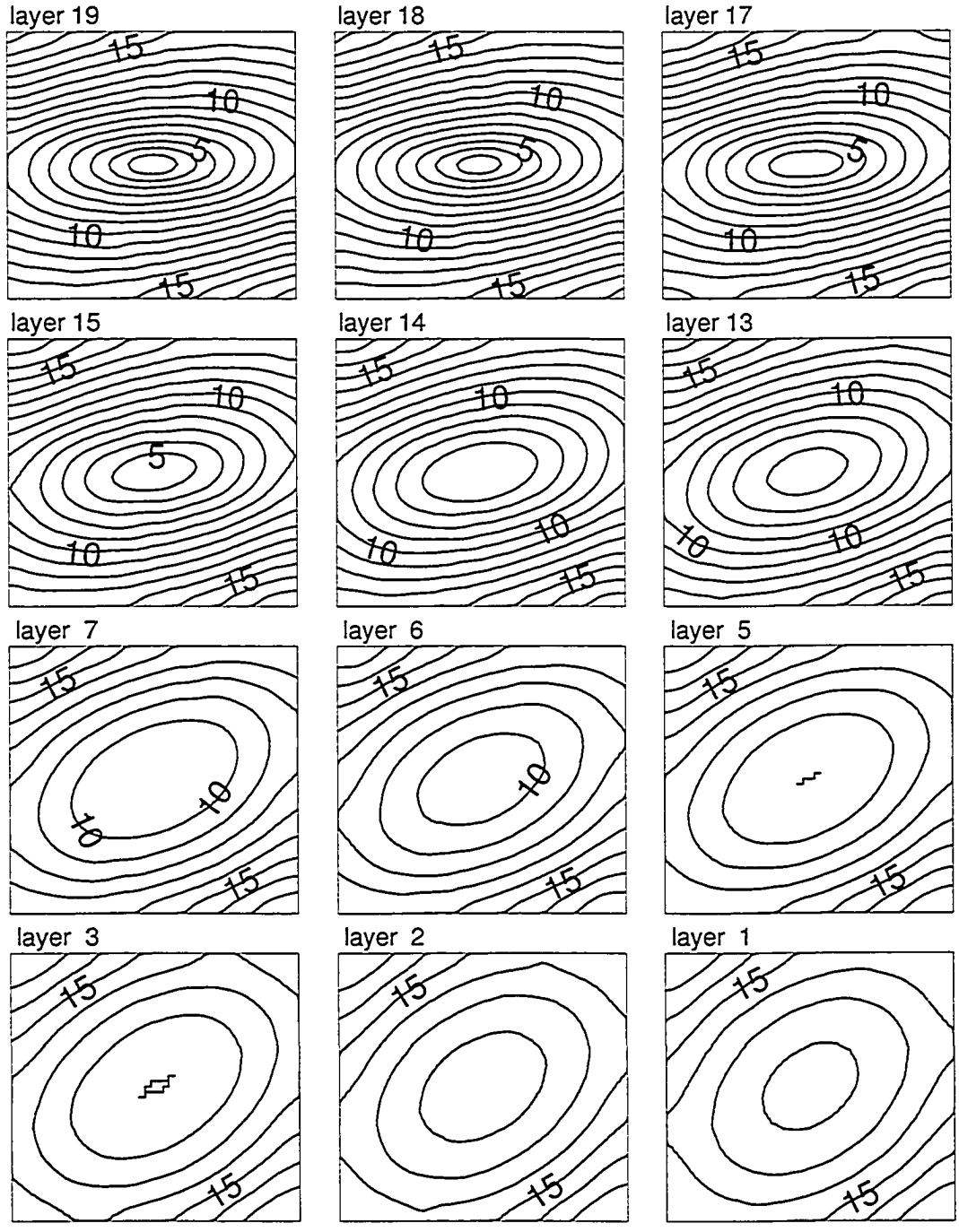

Figure 3.3: Rotational anisotropy: the combined effects of anisotropy and fiber rotation. Isochrones of activation have an elliptical shape due to the anisotropic property of the cardiac tissue. Note that the elliptical shapes rotate from top to bottom of the block, but less than that of the fiber direction.

However, this rotation is less than that of the 90° counterclockwise rotation of fiber direction, and is due to a phase lag in the rotational wave.

3.4 Scroll Waves in an Anisotropic Ventricular Myocardium

3.4.1 Introduction

Mathematical models for simulating the electrical propagation phenomena in the heart can provide valuable insight into the normal and pathological process of cardiac depolarization and repolarization. Of particular importance is the formation and termination of reentrant excitation. Reentry occurs when the propagating wave of electrical activity re-invades previously excited tissue and excites it again. If this happens repeatedly, it can lead to rapid, self-sustaining electrical activity in the heart which underlies the life-threatening cardiac arrhythmias such as ventricular tachycardia, and atrial and ventricular fibrillation. Spiral-wave activity has been proposed as a mechanism for this reentrant excitation in two-dimensional media [42, 50, 90, 88]. Recent experimental evidence [20, 21, 22, 27, 51] supports this claim. Scroll waves, the three-dimensional analogue of spiral waves, have similarly been proposed as a mechanism for reentry in three-dimensional tissue [90, 88], but experimental evidence for this is still scanty [27, 91], mostly due to the difficulty of measuring electrical activity in three-dimensional tissue.

Reentrant rotating waves in mathematical models of cardiac electrical activity have been studied by many investigators [5, 7, 19, 20, 22, 49, 51, 52, 60, 84]. Much of this work is restricted to two-dimensional simulations using the simple FitzHugh-Nagumo (FN) membrane model. Some exceptions do apply. Courtemanche and Winfree [19] showed reentrant patterns in a two-dimensional sheet of cells using the ionic model of Beeler and Reuter [6], and Pertsov and Jalife [52] used FN equations to demonstrate vortex-like reentry in three dimensions. The nature of three-dimensional reentry with the LR1 ionic model has been investigated [5, 60]; however, in each case the authors used simple explicit schemes to solve the differential equations.

The primary goal of this section is to investigate the formation of scroll waves in

a simplified slab model of the ventricular myocardium, using the implicit numerical methods developed in Chapter 3. To describe the ionic currents, we shall use the LR1 model [43].

3.4.2 Methods

A rough estimate of the wavelength, and hence the size of rotating waves for LR1 media is given by $s \times \text{APD}$, where s is the wave speed and APD is the action potential duration. For our propagation model, the wave speeds in the transverse and longitudinal directions are approximately 0.025 cm/ms and 0.035 cm/ms, respectively, and the APD of the LR1 model is 366 ms. An investigation of reentrant rotating waves would therefore require simulations of blocks of tissue on the order of 10 cm $\times$ 10 cm. To reduce this requirement, and hence the computational load, we modified the LR1 model to produce an action potential with the same essential shape but with a reduced duration. To reduce its action potential duration to approximately 200 ms, the time constants for calcium channel activation and inactivation were replaced by $\tau_{d,\text{new}} = 0.5\tau_d$ and $\tau_{f,\text{new}} = 0.5\tau_f$, respectively; the time constant for activation of the time-dependent potassium current was changed to $\tau_{X,\text{new}} = 0.4\tau_X$; and the maximum conductance for the plateau potassium current was increased to $\hat{G}_{\text{Kp, new}} = 0.0583\,\text{mS/cm}^2$. Figure 3.4 shows the action potential as calculated from both the modified and unmodified LR1 model.

Tissue Block for Cross-field Stimulation: We consider a 5 cm $\times$ 5 cm $\times$ 0.5 cm block that consists of homogeneous myocardial tissue with *uniform anisotropy*; that is, we neglect the rotation and curvature of the fibers, and furthermore, the fibers are assumed to run parallel with the x-axis. The z-axis is vertical, and the planes $z = 0$ and $z = 0.5$ represent the endo- and epicardial surfaces, respectively. Using a uniform spatial step of 0.05 cm, the block was discretized by $100 \times 100 \times 10$ nodes. To initiate rotating waves, we used the cross-field stimulation method [20]. Excitation was begun with a basic stimulus applied to the entire left lateral face of the block of tissue. This initiated a planar wave that propagated from left to right. A second premature stimulus was then applied to the entire front lateral face. The propagation parameters are given in Table 3.3.

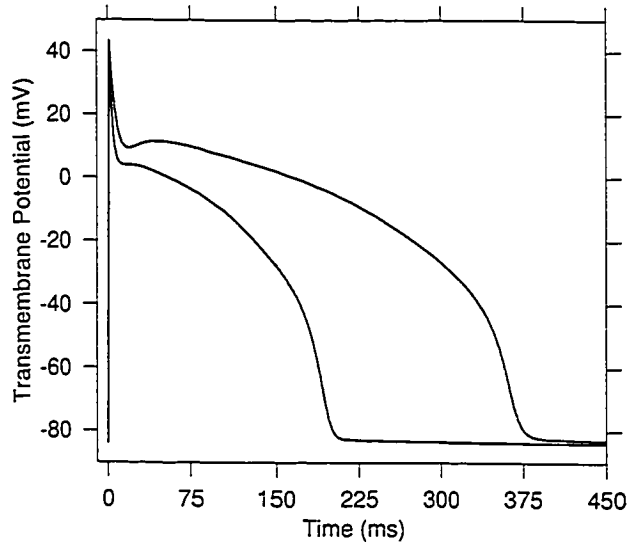

Figure 3.4: Action potentials from the original and modified LR1 model.

Table 3.3: Propagation parameters for reentrant rotating wave simulations.

Equal anisotropy ratio r	1.0
Intracellular transverse conductivity σ_t^i	0.5 mS/cm
Intracellular longitudinal conductivity σ_l^i	1.0 mS/cm
Membrane capacitance C_m	1.0 μF/cm^2
Surface-to-volume ratio χ	1000.0 cm^{-1}
Spatial step $hx = hy = hz$	0.05 cm
Time step k	0.2 ms
Basic current stimulus I_{app}	30.0 μA/cm^2
Duration of basic stimulus t_{off}	2.5 ms
Premature current stimulus I_{app}	12.0 μA/cm^2
Duration of premature stimulus t_{off}	4.0 ms

Tissue Block for Pinwheel Stimulation: Here we used the exact same setup as above, except the block size was increased to 5 cm × 5 cm × 1 cm and subsequently discretized by 100×100×20 nodes. Rotating waves were initiated with the pinwheel stimulation protocol as follows. As before, excitation was begun with a basic stimulus applied to the entire left lateral face of the block, which initiated a planar wave that propagated from left to right. However, the second premature stimulus was applied to an area on the top face of the block just behind the propagating refractory tail of the first wave. The propagation parameters are given in Table 3.3.

All computer programs were written in FORTRAN 77. The simulations were performed on an IBM RS/6000 model 590 with version 3.1.2 of the IBM XL Fortran compiler.

3.4.3 Results

Figure 3.5 shows the sequential time plots of the electrical activity resulting from cross-field stimulation on the top face or epicardial surface of a 5 cm × 5 cm × 0.5 cm block. The first panel shows the propagating refractory tail of the first wave that propagated from left to right just before onset of the second stimulus occurred. Panels 2 through 4 show the initiation of a second planar wave that propagated from front to back except at the right where it encountered the refractory tail of the first wave. In panel 5, we see the first formation of a wave break that propagated to the right in the now recovered zone. The remaining panels show that this wave break began to curl and led to the formation of a clockwise rotating scroll wave.

Figure 3.6 shows the sequential time plots of the electrical activity on the epicardial surface resulting from the pinwheel stimulation protocol. As before, panel 1 shows the propagating refractory tail of the first wave that propagated from left to right. Panel 2 shows the activated region resulting from the second stimulus. This premature stimulus was applied to a rectangular patch of cells (30 × 40) on the top layer of the block of tissue. Excitation from this stimulus initially propagates in all directions, except towards the right. In panel 6 we see the formation of two counter-rotating waves that are subsequently terminated when they hit the left border before curling around to complete another rotation.

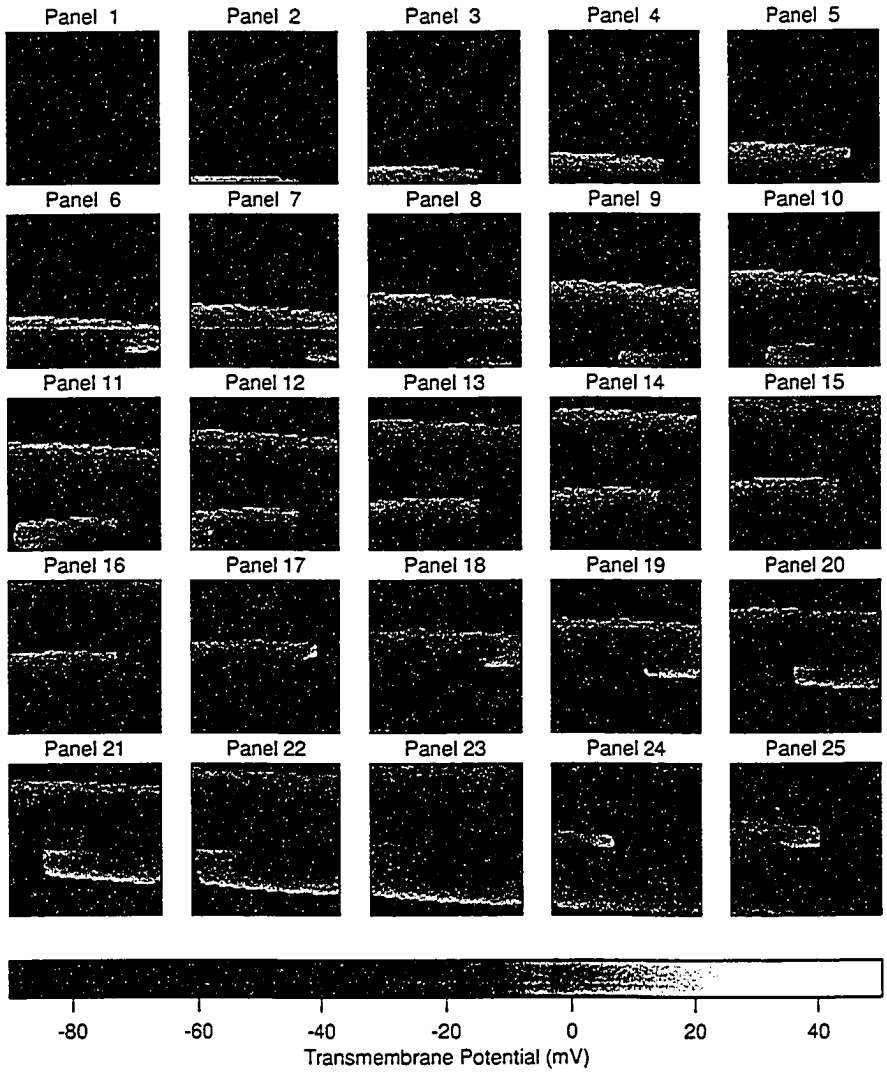

Figure 3.5: Initiation of reentrant activity in the form of a scroll wave in a 5 cm × 5 cm × 0.5 cm homogeneous block of myocardial tissue with uniform anisotropy. Panels 1 through 25 show the time variation of electrical activity on the top face of the block only. Panel 1 is a snapshot at t = 400 ms and the time interval between subsequent panels is 50 ms. Transmembrane voltage is shaded according to the grey-scale shown in the bottom panel.

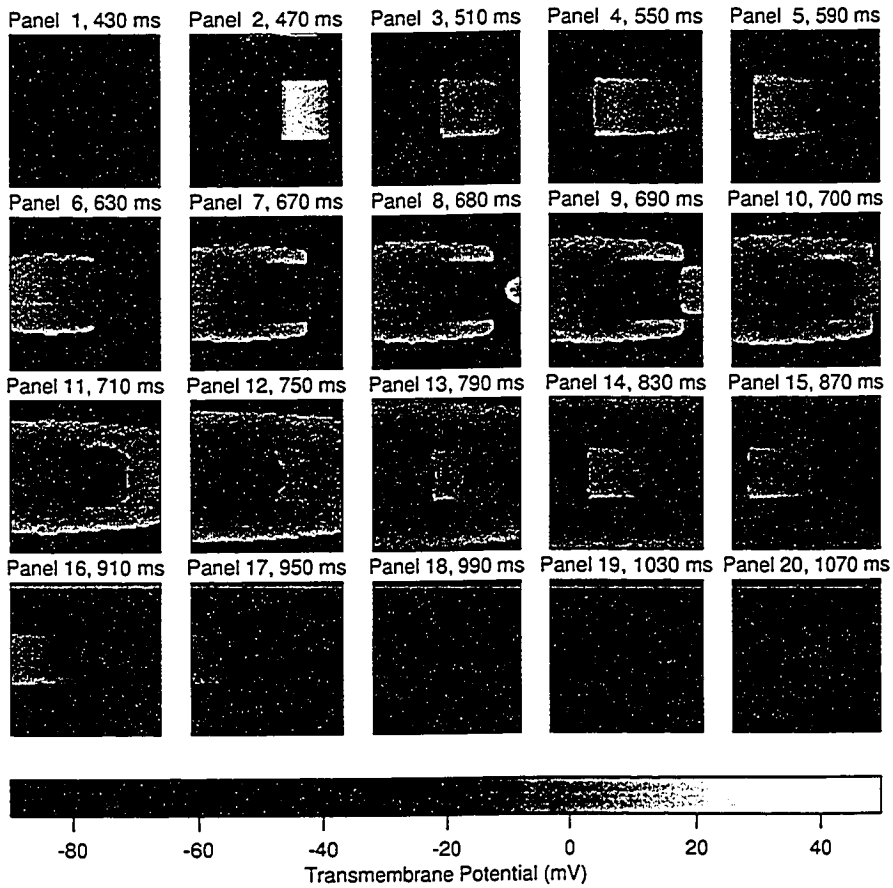

Figure 3.6: Initiation of reentrant activity in the form of counter-rotating waves in a 5 cm × 5 cm × 1 cm homogeneous block of myocardial tissue with uniform anisotropy. Other explanations as in Figure 3.5.

3.4.4 Conclusions

Despite the uniform anisotropy of the medium, the scroll waves were not stationary. In the case of the cross-field stimulation, the resulting scroll wave drifted from front to back, and then right to left and left to right several times. At approximately $t = 2900\,\text{ms}$, the wave front struck the left border before it could curl around. This led to termination of the scroll wave. In addition, timing of the the second, premature stimulus was critical in initiating the rotating waves. Applying the second stimulus at a later time shifts the wave break seen in panel 5 of Figure 3.5, for example, towards the right. If the stimulus was applied too late, this wave break struck the right border and was extinguished before it could curl around. In a similar fashion, applying the premature stimulus too soon shifted the wave break towards the left. In this case, the wavefront did curl around, but it subsequently struck the left border and was extinguished before it could curl around again to complete a full cycle.

We have investigated the propagation of electrical activation in the three-dimensional anisotropic ventricular myocardium using a mathematical model based on bidomain theory. A key feature of the model is a physiologically accurate formulation of the ionic currents describing the transmembrane action potential. This feature allows for simulation of the phenomena of action-potential propagation which fully incorporates the recovery phase of the process. Many propagation models to date often lack this feature, particularly in three-dimensional simulations. Though we present only the results for the case of uniform anisotropy, the mathematical model and corresponding numerical methods allow incorporation of anatomically accurate properties of cardiac tissue such as fiber rotation and curvature.

3.5 Discussion

In this chapter, we have implemented a monodomain model of the propagation of electrical activity in the anisotropic ventricular myocardium. For the ionic current term we utilized the LR1 model of Hodgkin-Huxley type gating equations,

which incorporates an accurate description of the membrane action potential. In Section 3.2 we focused on the numerical methods needed to solve such a problem. We then employed these methods to perform numerical simulations of cardiac action-potential propagation in a block of tissue representing a portion of the ventricular wall. The results are presented in Section 3.3.

We have ignored the curvature of the myocardial fibers. However, since these simulations are performed on a small block of tissue, it is reasonable to assume that the curvature of the fibers is negligible within this block.

A comparison of our results with those of Colli Franzone and Guerri [17, see Fig. 2] and Horáček et al [37, see Fig. 1] reveals striking qualitative similarities, despite the fact that they have used a *simplified* ionic current model of the membrane potential. Moreover, though our model assumes an equal anisotropy ratio, the results are still similar to the model of Colli Franzone and Guerri, which does not make this assumption.

One noticeable difference, however, occurs at the boundaries. Colli Franzone and Guerri reported a change in the curvature of the activation wavefront along the boundaries. We have also observed this same effect, but there appears to be a greater degree of flattening of the wavefront in the results obtained here. This may be an effect of the boundary conditions used in our model; Colli Franzone and Guerri have utilized more general boundary conditions (see equation (2.4) in [17]). Briefly, the boundary conditions of our model are

$$\boldsymbol{n} \cdot \nabla V_{\mathrm{m}} = 0$$

and those of Colli Franzone and Guerri,

$$\boldsymbol{n} \cdot \boldsymbol{D}_i \nabla V_{\mathrm{m}} = 0$$

where $\boldsymbol{n}$ is the unit outward normal vector. Both conditions reflect the fact that there is no current flow across the boundary; however, the latter equation includes the tensor $\boldsymbol{D}_i$ and so incorporates the anisotropy and fiber geometry.

The boundary condition $\boldsymbol{n} \cdot \nabla V_{\mathrm{m}} = 0$ was used due to the limitations of the finite-difference scheme employed. General boundary conditions destroy the tridiagonal nature of the system of equations, and greatly reduces the efficiency of the method.

In summary, we have established the feasibility of three-dimensional numerical simulations of the propagated activation in cardiac tissue. Moreover, the results obtained in this chapter show strong agreement with that of others, such as Colli Franzone and Guerri [17].

Chapter 4

Implementation of Bidomain Model

In this chapter, we present the numerical methods to solve the bidomain model. The solution is obtained via the method of lines approach. In short, this involves discretizing all spatial variables, which results in a system of differential-algebraic equations (DAEs). The system of DAEs is then handed off to a robust DAE solver, which takes on the job of time discretization and of evolving the system in time accurately, while maintaining stability.

4.1 Computer Implementation of the Bernus Model

The Bernus model contains dozens of parameters. It is important to first catagorize these parameters. The independent variable is t, while V_m, m, v, f, to, and X constitute the dependent variables. All remaining parameters are either constants (e.g., C_m, $\bar{G}_{Na}$, E_{Na}) or, in the majority of cases, functions of the other parameters (e.g., α_m, β_m, τ_m, m_∞). Therefore, the Bernus model was implemented essentially as a collection of function definitions.

The software is written in the Fortran 90 programming language. This programming language offers several advantages. First, a great deal of existing numerical software is written in Fortran[1], and it is therefore relatively easy to reuse such software. Second, use of a feature called kind attributes allows one to easily switch from single-precision floating-point variables to double-precision, or vice-versa. And third, the `module` feature provided by Fortran 90 allows convenient packaging and reuse of related constants, functions, subroutines, etc. For example, this feature allows an AP model to be encapsulated in a self-contained package.

The complete implementation of the Bernus model is extensive and will not be

[1]To a large extent though, this existing software is written in FORTRAN 77.

given here. However, in the next few sections we discuss some specific details of the implementation that do warrant mention. We begin with an overivew of how one ionic current is implemented.

4.1.1 An Example: The Fast Sodium Current

Let us first familiarize ourselves with the formulation of the fast Na^+ current. This current is defined as

$$I_{Na} = \bar{G}_{Na} \cdot m^3 \cdot v^2 \cdot (V_m - E_{Na}) \tag{4.1}$$

where

$$\bar{G}_{Na} = 16.0 \text{ nS/pF} \tag{4.2}$$

$$E_{Na} = \frac{RT}{F} \cdot \log\left(\frac{[Na^+]_o}{[Na^+]_i}\right) \tag{4.3}$$

The parameters m and v are gating variables, each governed by an ODE of the form of equation (2.4) with associated parameters

$$\alpha_m = \frac{0.32(V_m + 47.13)}{1 - e^{-0.1(V_m+47.13)}} \tag{4.4}$$

$$\beta_m = 0.08e^{-V_m/11} \tag{4.5}$$

$$v_\infty = 0.5\,[1 - \tanh(7.74 + 0.12 \cdot V_m)] \tag{4.6}$$

$$\tau_v = 0.25 + 2.24\frac{1 - \tanh(7.74 + 0.12 \cdot V_m)}{1 - \tanh[0.07 \cdot (V_m + 92.4)]} \tag{4.7}$$

The parameters F and R are the Faraday's and gas constants, respectively. The Na^+ concentrations and the temperature T are assumed to be constant in the Bernus model. This additionally means that E_{Na} is constant throughout an AP simulation.

To implement this current, first the constants are declared; they are later assigned values once at the beginning of the simulation. Implementation of the gating variable m is accomplished by the definition of five functions:

- `alpha_m`, the opening rate constant;
- `beta_m`, the closing rate constant;
- `m_inf`, the steady-state value;

- `tau_m`, the time constant; and
- `mdot`, the rate of change of X.

All of the functions depend on V_m, but the last function additionally depends on m. The first two functions are defined by using the formulations in equations (4.4) and (4.5). The remaining three functions are then defined in terms of `alpha_m` and `beta_m`. For the most part this implementation is straightforward. However, The `alpha_m` function requires special attention because when $V_m = -47.13$ mV, the denominator in (4.4) is zero. Details of how this is dealt with are the subject of the next section.

4.1.2 Treatment of Singular Functions

Recall that the function α_m is defined as

$$\alpha_m = \frac{0.32(V_m + 47.13)}{1 - e^{-0.1(V_m+47.13)}} \tag{4.4}$$

As it stands, this function is undefined when $V_m = -47.13$ mV, but the limit of the function as V_m approaches this value exists and is finite; indeed, we have

$$\lim_{V_m \to -47.13} \alpha_m(V_m) = 3.2 \tag{4.8}$$

This function thus requires special attention to implement as a Fortran procedure. An initial attempt at implementing this function might involve the following pseudocode:

```
if V_m = -47.13 then
   Set α_m = 3.2
else
   Compute α_m from equation (4.4)
endif
```

This method, however, is not suitable for two reasons. First, one should never test for strict equality of floating-point variables. And second, as V_m approaches -47.13, the denominator (and numerator) involves the subtraction of two nearly

equal numbers; this can lead to a loss of accuracy in floating-point arithmetic and thereby produce inaccurate values for α_m even when V_m is not just equal to, but *near* the singular point. The approach taken here is to evaluate α_m in the neighbourhood of -47.13 using a Taylor series expansion. It is easy to verify that α_m can be written as

$$\alpha_m = 3.2 \cdot F(-0.1(V_m + 47.13)) \tag{4.9}$$

where

$$F(y) = \frac{-y}{1 - e^y} \tag{4.10}$$

(Observe that the $\lim_{y \to 0} F(y)$ is easily found to be 1, and from this the result in equation (4.8) follows immediately.) The Taylor series expansion of $F(y)$ about $y = 0$ is

$$F(y) = 1 - \frac{1}{2}y + \frac{1}{12}y^2 - \frac{1}{720}y^4 + \frac{1}{30240}y^6 + \cdots \tag{4.11}$$

Furthermore, we will only use this Taylor series when the membrane potential is within 0.5 mV of -47.13 mV, i.e., $|V_m + 47.13| \leq 0.5$. With this restriction, a sixth order Taylor polynomial suffices, and so we have

$$\alpha_m \approx 3.2\left(1 - \frac{1}{2}y + \frac{1}{12}y^2 - \frac{1}{720}y^4 + \frac{1}{30240}y^6\right), \quad y = -0.1(V + 47.13) \tag{4.12}$$

Thus, the function `alpha_m` is implemented as follows:

```
if |V_m + 47.13| ≤ 0.5 then
   Compute alpha_m from equation (4.12)
else
   Compute alpha_m from equation (4.4)
endif
```

4.1.3 Table Look-up for Expensive Functions

Many of the functions in the Bernus model are expensive to evaluate in terms of computation time, particularly those functions which call the intrinsic exponential or logarithm functions. (This is especially a problem for propagation simulations where more than half of the CPU time may be spent in evaluating the exponential function rather than solving the actual system.) To circumvent this problem, costly

functions can be replaced by table look-up routines [83, 85]. This is the general method adopted here. For a given expensive function, say $f(x)$, this function is pre-computed for the set of x values $\{x_i\}_{i=1}^{N}$ where $x_1 = x_{\min}$, $x_N = x_{\max}$, and $x_i - x_{i-1}$ is constant. The tabluated values $f_i \equiv f(x_i)$ are stored in a one-dimensional array of size N. The table look-up function, when called with some arbitrary value $\bar{x}$, returns the value $\bar{f}$ such that $\bar{f}$ is a linear interpolation between the values f_i and f_{i+1} where $x_i \leq \bar{x} \leq x_{i+1}$. (This assumes that $x_{\min} \leq \bar{x} \leq x_{\max}$.) The table look-up algorithm is implemented in a generic function called `table_lookup` as follows.

```
function table_lookup (value, table, min_value, max_value, &
   stepinv) result (result)
   real(WP), intent(in) :: value, table(:)
   real(WP), intent(in) :: min_value, max_value, stepinv
   real(WP) :: result
   integer :: ivalue
   real(WP) :: A, B

   ivalue = int( (value - min_value) * stepinv ) + 1
   A      = table(ivalue)
   B      = table(ivalue + 1)
   result = A + (B - A) &
      * ( (value - min_value) * stepinv - real(ivalue - 1, WP) )
end function table_lookup
```

The argument `value` corresponds to x; `table` is the one-dimensional array of tabluated values f_i; `min_value` and `max_value` correspond to $x_{\min}$ and $x_{\max}$, respectively; and `stepinv` is the inverse of the step between x_i values, i.e., `stepinv` $= 1/(x_2 - x_1)$. (Note again that a constant step is assumed.) The calculation of `ivalue` determines i such that $x_i \leq$ `value` $\leq x_{i+1}$. The corresponding function values are then easily obtained. And finally, a simple linear interpolation between the tabulated values `A` and `B` is done. Note this function assumes that the argument `value` falls within the pre-tabulated range; i.e., it assumes `min_value` $\leq$ `value` $\leq$ `max_value` and does not perform error-checking to verify this.

4.2 Numerical Methods for AP Models

We wish to solve the problem

$$C_m \frac{dV_m}{dt} = I_{app}(t) - I_{ion}(V_m, u)$$
$$\frac{du}{dt} = w(V_m, u)$$

subject to appropriate initial conditions. Due to the nonlinearity inherent in the I_{ion} term, an analytical solution of the problem is unlikely; hence, we must resort to numerical methods. Depending on the actual AP model, the above system of equations is often stiff and can pose challenges to solve numerically. If the numerical method is not chosen carefully, instabilities or inaccuracies can arise in the solution process. Fortunately, a lot of robust software, which is capable of solving a problem such as ours, already exists. We will use the software package DASPK written by Petzold and colleagues [8, 10]. All modern, professionally-written ODE solvers—such as DASPK—perform adaptive time-stepping and reduce the stepsize in response to instability. "Thus the codes do not give a faulty solution because of the instability for large stepsizes, but instead reduce the stepsize and become very inefficient." [8, p. 127] Furthermore, DASPK is capable of solving systems of differential-algebraic equations (DAEs), not just systems of ODEs. This feature allows us to later use the same software to solve models of propagation.

4.2.1 The Jacobian Matrix

Use of the software DASPK requires that the differential-algebraic system be specified as

$$F(t, y, y') = 0 \tag{4.13}$$

For our problem this is easily arrived at by simply rewriting the equations as

$$C_m \frac{dV_m}{dt} + I_{ion} - I_{app} = 0$$
$$\frac{du}{dt} - w = 0$$

If we denote $y_1 = V_m$ and $y_{i+1} = u_i$ for $i = 1, \eta$, then the above equations are

$$C_m y_1' + I_{ion} - I_{app} = 0$$
$$y_{i+1}' - w_{i+1} = 0 \qquad i = 1, \eta$$

and this can be expressed in the form of equation (4.13) by further defining

$$F_1 = C_m y_1' + I_{ion} - I_{app} \tag{4.14}$$
$$F_{i+1} = y_{i+1}' - w_{i+1} \tag{4.15}$$

The Jacobian matrix J amd mass matrix M of the DAE system (4.13) are defined as

$$J_{i,j} = \frac{\partial F_i}{\partial y_j} \tag{4.16}$$
$$M_{i,j} = \frac{\partial F_i}{\partial y_j'} \tag{4.17}$$

In its solution process the DASPK software requires the iteration matrix of the DAE system. Each element of this matrix is given by $J_{i,j} + \delta M_{i,j}$. The parameter δ is a scalar determined by DASPK. From equations (4.14) and (4.15), the mass matrix is easily seen to be a constant diagonal matrix, and is therefore trivial to compute. Hereafter, we shall thus focus our attention on the Jacobian matrix.

Applying the definition of the Jacobian to the AP model, we arrive at the following equations

$$J_{1,1} = \frac{\partial I_{ion}}{\partial V_m}$$
$$J_{i+1,1} = -\frac{\partial w_i}{\partial V_m} \qquad i = 1, \eta$$
$$J_{1,j+1} = \frac{\partial I_{ion}}{\partial u_j} \qquad j = 1, \eta$$
$$J_{i,i+1} = -\frac{\partial w_i}{\partial u_i} \qquad i = 1, \eta$$
$$J_{i+1,j+1} = -\frac{\partial w_i}{\partial u_j} \qquad i = 1, \eta;\ j = 1, \eta$$

Except when $i = 1$, $j = 1$, or $i = j$, $J_{i,j}$ will usually be 0. However, there may be a few nonzero elements that are not in the first column or row, nor on the main diagonal. Examples of the structure of the Jacobian matrix are given in Figure 4.1.

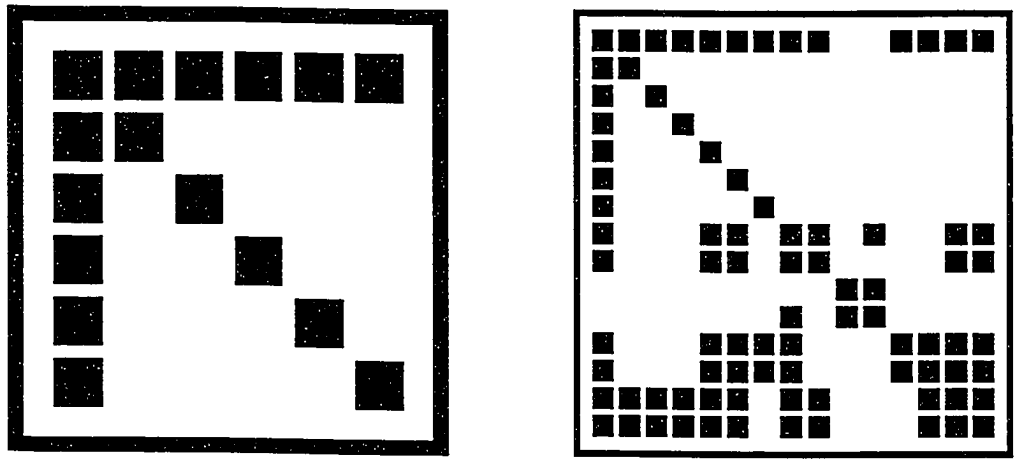

Figure 4.1: Structure of the Jacobian matrix for two AP models: (a) Bernus model; (b) LR2 model. Nonzero elements are indicated by the shaded squares. In the Jacobian for the Bernus model, the order of the AP variables is V_m, m, v, X, to, and f. The structure of the Jacobian will be the same regardless of the ordering of the auxiliary variables. The Jacobian for the LR2 model, however, will vary slightly in structure for different orderings of the auxiliary variables. In the above plot, the order of the AP variables for the LR2 model is V_m, m, h, j, d, f, X, $[Ca^{2+}]_i$, $[Ca^{2+}]_o$, $[Ca^{2+}]_{JSR}$, $[Ca^{2+}]_{NSR}$, $[K^+]_i$, $[K^+]_o$, $[Na^+]_i$, and $[Na^+]_o$.

4.2.2 Numerical Experiments

The numerical methods were implemented and simulations were performed on a desktop computer with two Intel Pentium III 733 MHz processors running the Linux operating system (Redhat 7.3). None of the simulations took advantage of the two processors; that is, the software was not parallelized. Computation time for the simulations was insignificant: 500 ms of simulated activity took on the order of one second.

Validation of the Implementation

The Bernus model has provisions for three cell types. Our implementation correctly reproduces the APs of these cells, as shown in Figure 4.2 (cf. Figure 6 in [7]). The durations, measured at 90 % repolarization, of the epicardial, M cell, and endocardial APs were found to be 357, 396, and 359 ms, respectively. These values

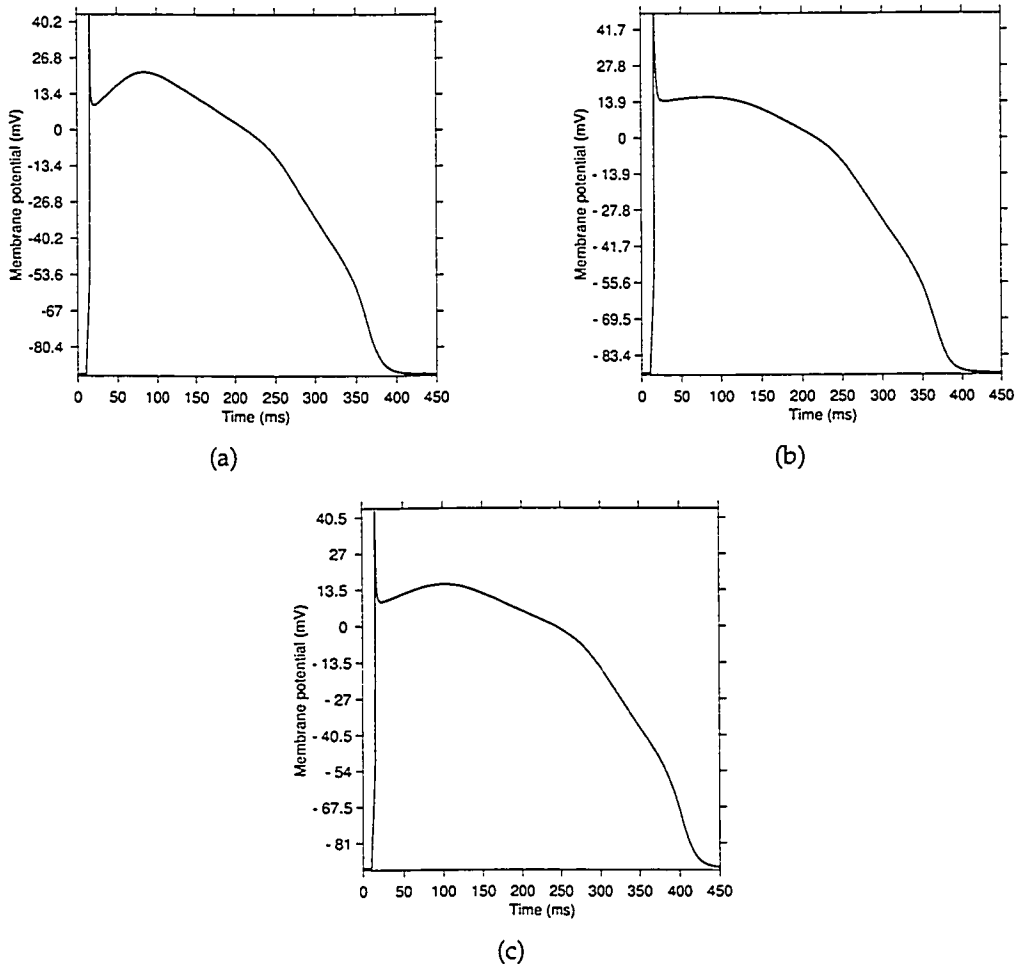

Figure 4.2: Action potentials for three different configurations of the Bernus model: (a) an epicardial cell; (b) an endocardial cell; (c) a midmyocardial cell (M cell). The important characteristics of the three APs are apparent: the epicardial AP has a notch and spike-and-dome shape, the M cell AP has a prolonged APD and less pronounced notch, and the endocardial AP is nearly triangular in shape with no notch.

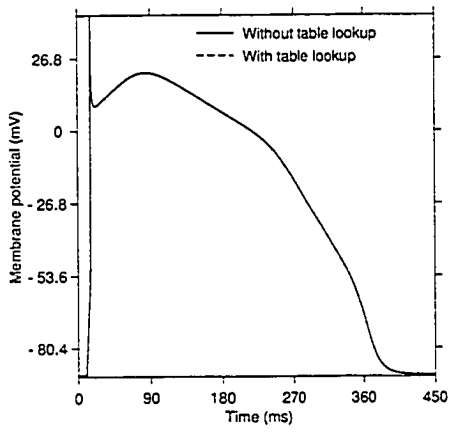

Figure 4.3: Epicardial action potential of the Bernus model both with and without table-lookup. In the table-lookup code, expressions involving the membrane potential only were pretabulated from −300 to 300 mV with a step of 2 mV. The excellent agreement of the table-lookup AP with the standard AP (without table-lookup) is illustrated by the near-perfect coincidence of the two curves.

compare well with those given in [7]: 360, 400, and 362 ms.

Validation of the Use of Lookup Tables

The accuracy of the table-lookup code is affected by the resolution of the tables; some experimentation is necessary to find the proper resolution. In this section, we compare results with the use of lookup tables to results from the standard model (i.e., without lookup tables).

Figure 4.3 shows the standard epicardial AP and the same AP computed with the use of lookup tables. All expressions involving the membrane potential only were pretabulated from −300 to 300 mV with a step of 2 mV. The fact that only one curve is apparent in the figure indicates the excellent agreement of the two APs.

The previous results are from simulations of one AP initiated by a single stimulus. A more stressful test of the performance of the table-lookup code is achieved by simulated pacing. Figure 4.4(a) shows results from simulations where an initial stimulus is given at $t = 10$ ms, followed by subsequent stimuli given every 340 ms. Some minor discrepancies between the standard and table-lookup APs

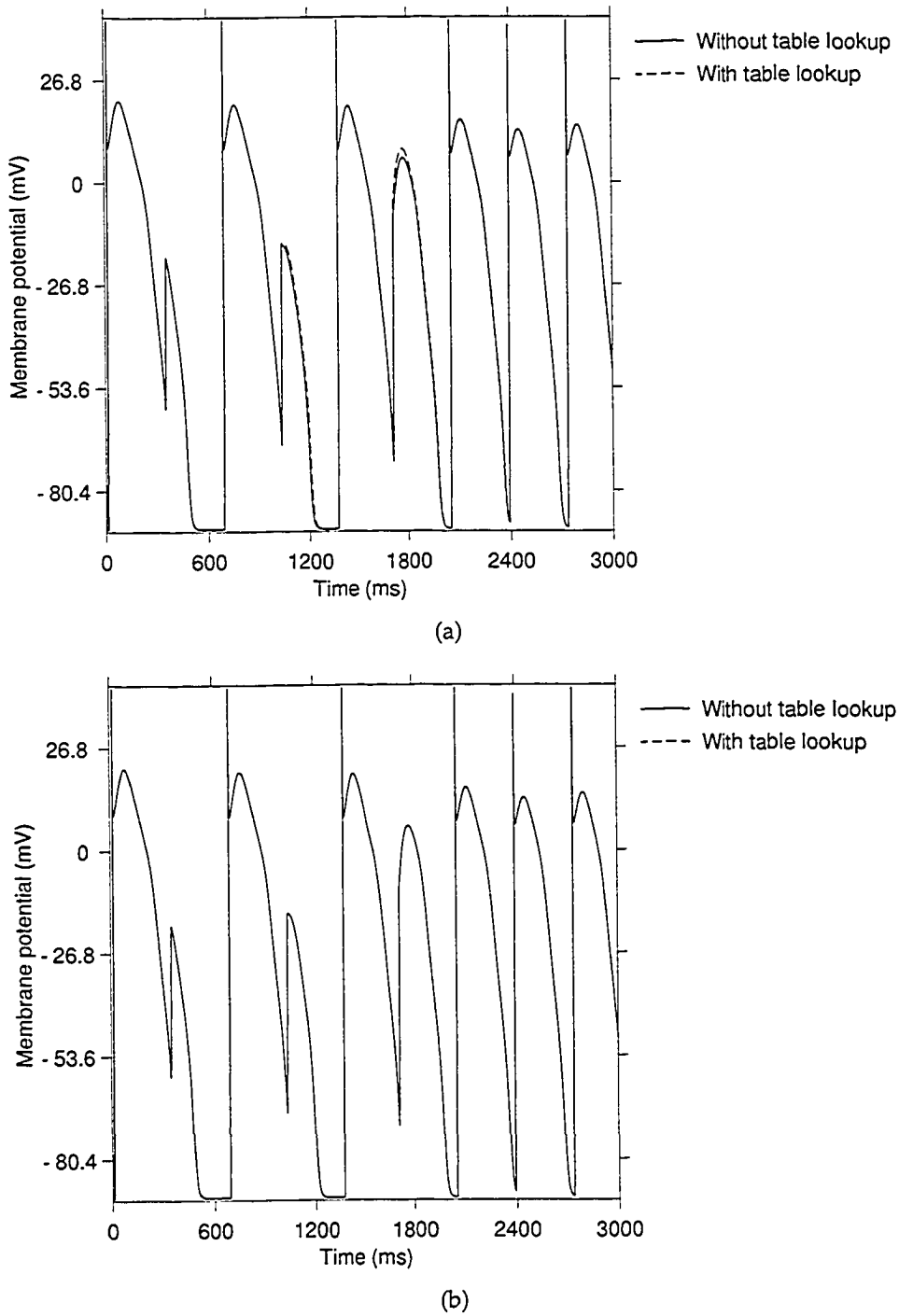

Figure 4.4: Simulated pacing of the Bernus epicardial model with and without table-lookup. In (a), the pretabulated values were computed from −300 to 300 mV with a step of 2 mV. In (b), the pretabulated values were computed on the same range, but with a step of 0.1 mV.

are apparent. Figure 4.4(b) shows results from the same simulations with higher-resolution lookup tables: the voltage step for the pretabulated values was decreased to 0.1 mV. Once again, excellent agreement between the standard and table-lookup APs is achieved. Further simulations revealed no appreciable difference between the standard and table-lookup code at the 0.1 mV voltage step; a table-lookup model employing this increment was therefore deemed acceptable.

4.3 Numerical Methods for 1-D Propagation Models

In this section we present the methods used to solve the 1-D model numerically. For clarity, we restate the complete equations here. The mathematical model to be solved is

$$C_m \frac{\partial V_m}{\partial t} = \frac{1}{\chi}\left(g_i \frac{\partial^2 V_m}{\partial x^2} + g_i \frac{\partial^2 \Phi_e}{\partial x^2}\right) + S(x, t, V_m, u) \tag{4.18}$$

$$\frac{1}{\chi}\left[(g_i + g_e)\frac{\partial^2 \Phi_e}{\partial x^2} + g_i \frac{\partial^2 V_m}{\partial x^2}\right] = 0 \tag{4.19}$$

$$\frac{\partial u}{\partial t} = w(V_m, u) \tag{4.20}$$

$$g_i\left(\frac{\partial V_m}{\partial n} + \frac{\partial \Phi_e}{\partial n}\right) = \gamma_1 \tag{4.21}$$

$$\alpha \Phi_e + \beta g_e \frac{\partial \Phi_e}{\partial n} = \gamma_2 \tag{4.22}$$

$$V_m(x, 0) = V_{m0}(x) \tag{4.23}$$

$$\Phi_e(x, 0) = \Phi_{e0}(x) \tag{4.24}$$

$$u(x, 0) = u_0(x) \tag{4.25}$$

where

$$S(x, t, V_m, u) = -I_{ion} + I_{app}$$

To compute a numerical solution to the above model, we use the following general approach:

- first discretize the spatial variables;
- then solve the resulting system of DAEs.

This is known as the *method of lines* approach [1, 45, 73].

4.3.1 Spatial Discretization

First, some notation and definitions are in order. Let N be a positive integer and let $\{x^{(i)}\}_{i=0}^{N}$ be a partition of $[0, l]$ such that

$$0 = x^{(0)} < x^{(1)} < x^{(2)} < \cdots < x^{(N-1)} < x^{(N)} = l$$

For simplicity, we consider an equally spaced grid; i.e., $x^{(i)} = i \cdot \Delta x$ where $\Delta x = l/N$. Let $V_{\mathrm{m}}^{(i)}(t)$ denote $V_{\mathrm{m}}(x^{(i)}, t)$, $\Phi_{\mathrm{e}}^{(i)}(t)$ denote $\Phi_{\mathrm{e}}(x^{(i)}, t)$, and similarly, $u^{(i)}(t)$ denotes $u(x^{(i)}, t)$. We also define $u_j^{(i)}(t) = u_j(x^{(i)}, t)$, which is the jth element of $u(x^{(i)}, t)$.

For the discretization, we replace all of the spatial derivatives on the interior of the domain with second-order finite-difference approximations. For example, the term $\frac{\partial^2 V_{\mathrm{m}}}{\partial x^2}$ is replaced with the following

$$\left.\frac{\partial^2 V_{\mathrm{m}}}{\partial x^2}\right|_{x=x^{(i)}} \approx \frac{V_{\mathrm{m}}^{(i+1)} - 2V_{\mathrm{m}}^{(i)} + V_{\mathrm{m}}^{(i-1)}}{\Delta x^2} \quad \text{for } i = 1, 2, \ldots, N-1 \tag{4.26}$$

An analogous approximation is used for $\frac{\partial^2 \Phi_{\mathrm{e}}}{\partial x^2}$.

The boundary conditions involve the spatial derivatives $\frac{\partial V_{\mathrm{m}}}{\partial x}$ and $\frac{\partial \Phi_{\mathrm{e}}}{\partial x}$. Here we have an option: we can use either first-order or second-order approximations. For first-order finite differences, we would replace $\frac{\partial V_{\mathrm{m}}}{\partial x}$ with

$$\left.\frac{\partial V_{\mathrm{m}}}{\partial x}\right|_{x=x_0} \approx \frac{V_{\mathrm{m}}^{(1)} - V_{\mathrm{m}}^{(0)}}{\Delta x} \tag{4.27a}$$

$$\left.\frac{\partial V_{\mathrm{m}}}{\partial x}\right|_{x=x_N} \approx \frac{V_{\mathrm{m}}^{(N)} - V_{\mathrm{m}}^{(N-1)}}{\Delta x} \tag{4.27b}$$

For second-order finite differences, we would replace $\frac{\partial V_{\mathrm{m}}}{\partial x}$ with

$$\left.\frac{\partial V_{\mathrm{m}}}{\partial x}\right|_{x=x_0} \approx \frac{-3V_{\mathrm{m}}^{(0)} + 4V_{\mathrm{m}}^{(1)} - V_{\mathrm{m}}^{(2)}}{2\Delta x} \tag{4.28a}$$

$$\left.\frac{\partial V_{\mathrm{m}}}{\partial x}\right|_{x=x_N} \approx \frac{3V_{\mathrm{m}}^{(N)} - 4V_{\mathrm{m}}^{(N-1)} + V_{\mathrm{m}}^{(N-2)}}{2\Delta x} \tag{4.28b}$$

Ideally, we would like to use the second-order approximations so as to maintain an accuracy level consistent with that used at the interior grid points. However, employing the approximations in (4.28) leads to a Jacobian matrix with a larger bandwidth than using (4.27), and, as we will see later, this increases the amount of

CPU time and memory required for simulations. Our software implements both sets of approximations and allows the user to choose at compile time which set to use. The default is the first-order approximations.

Discretization of equation (4.20) is simple: since there is no explicit spatial dependence in the equation, we merely replace it with the following

$$\frac{du^{(i)}}{dt} = w(V_{\mathrm{m}}^{(i)}, u^{(i)}) \tag{4.29}$$

for $0 \le i \le N$.

Some more notation is in order. Define:

$$v = \begin{bmatrix} V_{\mathrm{m}}^{(0)} \\ V_{\mathrm{m}}^{(1)} \\ \vdots \\ V_{\mathrm{m}}^{(N)} \end{bmatrix} \qquad \phi = \begin{bmatrix} \Phi_{\mathrm{e}}^{(0)} \\ \Phi_{\mathrm{e}}^{(1)} \\ \vdots \\ \Phi_{\mathrm{e}}^{(N)} \end{bmatrix} \qquad z = \begin{bmatrix} u^{(0)} \\ u^{(1)} \\ \vdots \\ u^{(N)} \end{bmatrix}$$

and let N_{pts} represent the total number of grid points; i.e., $N_{\mathrm{pts}} = N + 1$. The discretized equations can be written as

$$\tilde{I}\frac{dv}{dt} - L_1 v - L_2 \phi - f(t, v, z) = 0 \tag{4.30a}$$

$$\tilde{L}_1 v + \tilde{L}_2 \phi = 0 \tag{4.30b}$$

$$\frac{dz}{dt} - q(v, z) = 0 \tag{4.30c}$$

subject to the initial conditions

$$v = v_0 \qquad \phi = \phi_0 \qquad z = z_0 \tag{4.30d}$$

In the above equations $\tilde{I}$ is an $N_{\mathrm{pts}} \times N_{\mathrm{pts}}$ matrix where if k corresponds to an interior point, then row k is equal to e_k^T (e_k is a unit vector with a 1 at position k and 0's elsewhere); otherwise, row k is equal to 0^T. Furthermore, L_1 is an $N_{\mathrm{pts}} \times N_{\mathrm{pts}}$ matrix resulting from disretization of the terms $g_{\mathrm{i}} \frac{\partial V_{\mathrm{m}}}{\partial n}$ and $\frac{g_{\mathrm{i}}}{\chi} \frac{\partial^2 V_{\mathrm{m}}}{\partial x^2}$ in equations (4.21) and (4.18), respectively. Likewise, the matrix L_2 results from disretization of the terms $g_{\mathrm{i}} \frac{\partial \Phi_{\mathrm{e}}}{\partial n}$ and $\frac{g_{\mathrm{i}}}{\chi} \frac{\partial^2 \Phi_{\mathrm{e}}}{\partial x^2}$ in the same equations. The matrices $\tilde{L}_1$ and $\tilde{L}_2$ are closely related to L_1 and L_2 as they arise from discretization of similar terms in equations (4.22) and (4.19). Also, f is a vector of dimension N_{pts} for which each element corresponds to

the source term for either the boundary condition (0 in equation (4.21)) or the PDE (S in equation (4.18)). Finally, q is a vector of dimension $\eta \cdot N_{\text{pts}}$ that corresponds to the source term, w, of equation (4.20).

4.3.2 Solution of A System of Differential-Algebraic Equations

Consider the general system of DAEs

$$F(t, y, y') = 0 \tag{4.31}$$

where consistent initial conditions $y(t_0)$ and $y'(t_0)$ are assumed to be given. To obtain a numerical solution to this problem at some time step t_n, one typically begins by replacing y'_n with a finite difference approximation. One of the simplest approximations is the difference:

$$y'_n \approx \frac{y_n - y_{n-1}}{\Delta t_n}$$

where $\Delta t_n = t_n - t_{n-1}$. Substituting the above approximation into (4.31) gives rise to a system of algebraic equations in y_n:

$$F\left(t_n, y_n, \frac{y_n - y_{n-1}}{\Delta t_n}\right) = 0 \tag{4.32}$$

This system of equations is quite often nonlinear, and so Newton's method is applied. Starting with an initial approximation y_n^0 based on information from previous time steps, the kth Newton iterate is given by

$$y_n^k = y_n^{k-1} - \left(\frac{\partial F}{\partial y} + \frac{1}{\Delta t_n}\frac{\partial F}{\partial y'}\right)^{-1} F\left(t_n, y_n^{k-1}, \frac{y_n^{k-1} - y_{n-1}}{\Delta t_n}\right) \tag{4.33}$$

Typically, this iteration is repeated until some preset tolerance is achieved. The method outlined above is known as the *backward Euler* or *implicit Euler* method, and it is a member of a larger class of methods based on *backward differentiation formulae* (BDF), which was pioneered by the work of Gear [28].

Solution of DAE systems can often be done using the same numerical methods for solving stiff ODE systems, for which a great deal of software already exists. However, DAE systems can exhibit properties very different from ODE

systems [54]. It is therefore preferrable to use software which addresses the issues specific to DAEs. Two such software packages written by Linda Petzold and colleagues are DASSL [55] and its derivative, DASPK [10]. Both packages can solve general systems of DAEs. On each time step, they use backward differentiation formulas of order one through five to reduce the DAE system to a system of nonlinear algebraic equations. The linear systems that arise from subsequent application of Newton's method are solved using a direct method with either a dense or banded Jacobian matrix. In DASPK the linear systems may also be solved with a preconditioned Krylov method, which often proves beneficial for large-scale DAE systems. As such, DASPK will be used to solve the DAE systems arising from the models investigated in this work.

4.3.3 Use of DASPK

The software DASPK is written in FORTRAN 77. In order to use this code, the user must provide a main program, which need not be written in FORTRAN 77, that performs the following basic tasks:

1. Define problem parameters.
2. Allocate work storage required by DASPK.
3. Provide consistent initial conditions.
4. Call DASPK.
5. Output solution.

Step 1 involves retrieval of several model parameters from a data file (such as the cable length, the number of grid points, the conductivity values, etc.) and calculation of remaining parameters (such as the space step). In a FORTRAN 77 program, step 2 would be performed first and would involve allocation of work storage for some *maximum* problem size. However, all programs for this study are written in Fortran 90, which has several new features not available in FORTRAN 77. In particular, Fortran 90 allows dynamic memory allocation, and so in step 2

the program allocates the precise amount of memory required for the current problem parameters. In step 3, the initial values are set according to the model (see Section 2.4). Steps 4 and 5 are normally performed many times. In our programs, post-processing of data is kept to a minimum; this task is usually handled off-line in separate programs.

DASPK also requires the user to supply a subroutine RES that defines the system of DAEs. This subroutine is called from within DASPK, often many times, as a part of step 4 outlined above. Further routines may be required from the user depending on the solution method selected. Recall the Newton iterate that arises as part of the solution process of the DAE system:

$$y_n^k = y_n^{k-1} - \left(\frac{\partial F}{\partial y} + \frac{1}{\Delta t_n}\frac{\partial F}{\partial y'}\right)^{-1} F\left(t_n, y_n^{k-1}, \frac{y_n^{k-1} - y_{n-1}}{\Delta t_n}\right)$$

Of special importance in this equation is the term $\frac{\partial F}{\partial y} + \frac{1}{\Delta t_n}\frac{\partial F}{\partial y'}$, which is known as the *iteration matrix*. Note that the iteration matrix is itself the sum of two important matrices: the Jacobian matrix, J, and the mass matrix, M, of the DAE system (4.31) are defined as

$$J = \frac{\partial F}{\partial y} \tag{4.34}$$

$$M = \frac{\partial F}{\partial y'} \tag{4.35}$$

For the DAE systems arising from the propagation models investigated in this work (see equation (4.30)), the mass matrix is a constant matrix with a simple structure, and is therefore easy to compute. We shall thus focus our attention on the Jacobian matrix.

4.3.4 The Jacobian Matrix

The Jacobian matrix can either be supplied by the user or approximated internally by DASPK. Implementing the Jacobian, particularly an analytical one, can be tedious and error prone. As a first step, we therefore use the approximation option provided by DASPK. Let N_{eqs} represent the total number of equations in the DAE system. For the discretized 1-D bidomain model (4.30), we have $N_{eqs} = (\eta+2)\cdot N_{pts}$.

(Recall that η is the number of auxiliary variables in the AP model and N_{pts} the total number of grid points.) The full Jacobian matrix is thus of order $N_{\text{eqs}} \times N_{\text{eqs}}$. The amount of work space required by DASPK is dominated by this matrix. Furthermore, the time to form this matrix and solve the associated linear system often dominates the time involved to solve the DAE system.

The structure of the Jacobian matrix is influenced by how the variables in the DAE system are ordered. There are two natural orderings that can be used: one where the dominant ordering is by dependent variable and a second by grid point. In the first scheme, the DAE system is arranged as follows:

$$V_{\text{m}}^{(0)}, \ldots, V_{\text{m}}^{(N)}, \Phi_{\text{e}}^{(0)}, \ldots, \Phi_{\text{e}}^{(N)}, u_1^{(0)}, \ldots, u_1^{(N)}, \ldots, u_\eta^{(0)}, \ldots, u_\eta^{(N)} \tag{4.36}$$

For the grid-point ordering, we have the variables listed as:

$$V_{\text{m}}^{(0)}, \Phi_{\text{e}}^{(0)}, u_1^{(0)}, \ldots, u_\eta^{(0)}, V_{\text{m}}^{(1)}, \Phi_{\text{e}}^{(1)}, u_1^{(1)}, \ldots, u_\eta^{(1)}, \ldots, V_{\text{m}}^{(N)}, \Phi_{\text{e}}^{(N)}, u_1^{(N)}, \ldots, u_\eta^{(N)} \tag{4.37}$$

To illustrate, consider a 1-D bidomain model with 11 grid points, and with a Bernus AP, for which $\eta = 5$. Thus, the total number of equations in the DAE system is $N_{\text{eqs}} = 77$. Figure 4.5 shows the structure (i.e., the nonzero entries) of the Jacobian for each of the two orderings. (Note that the structure of the Jacobian for the Bernus AP model as shown in Figure 4.1(a) is repeated in these structures; it is best seen on the interior of the grid-point ordering scheme.) Observe that the ordering by grid point yields a more compact Jacobian, in the sense that the elements fit in a smaller band about the main diagonal. Indeed, the upper and lower bandwidths are equal, and are found to be $\eta + 2$.

In solving the linear systems, DASPK can take advantage of the bandwidth information, and it will result in a reduction of the storage needed and faster execution of several important algorithms, such as the numerical differencing algorithm that computes the approximate Jacobian. The grid-point ordering has therefore been adopted as the scheme used in the programs implemented for this study.

Another important feature of the Jacobian matrix is apparent from Figure 4.5(b): the actual matrix for our problem has many zero entries, even within the band about the main diagonal. That is, the Jacobian is highly *sparse*. Table 4.1 summarizes the information about the Jacobian. For the current problem, the total number of

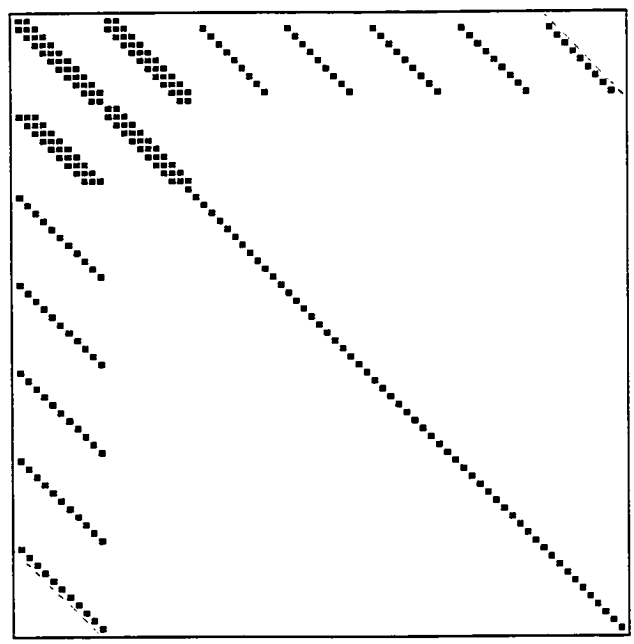

(a)

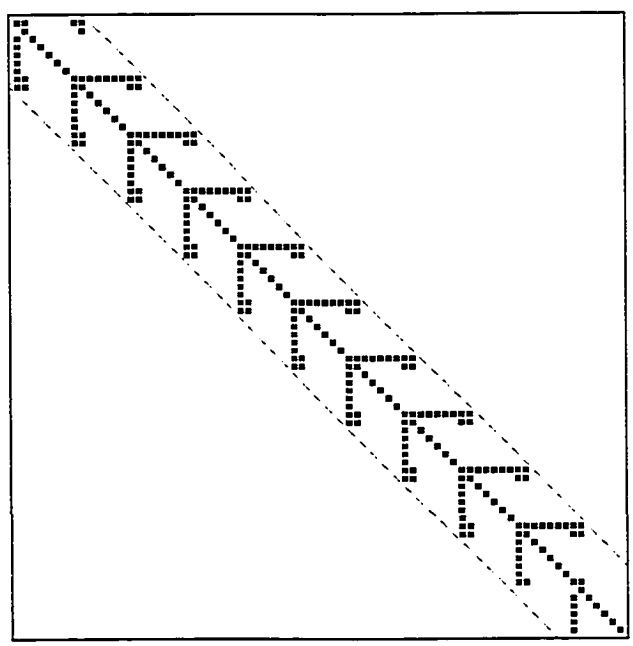

(b)

Figure 4.5: Structure of the Jacobian matrix for a 1-D bidomain cable with I_{ion} described by the Bernus AP model. Nonzero elements are indicated by the shaded squares. In (a), the ordering is by variable, while in (b) it is by grid point. The dashed lines indicate the bandwidths. The above plots are for a cable with 11 points; a cable with more points will have the same basic structure.

Table 4.1: Summary of the Jacobian storage requirements for a 1-D bidomain model.

Number of grid points		11
Number of AP variables		5
Number of equations		77
Type	Number of elements	Memory (kB)
Dense	5929	47.432
Banded	1309	10.472
Sparse	274	3.6

equations is 77, and to store the full (dense) Jacobian requires 77^2 or 5929 elements. In comparison, taking advatage of its banded structure requires only 1309 elements of storage. However, a mere 274 elements are actually nonzero, which is less than 5 % of the full Jacobian.

While the storage requirements listed in Table 4.1 are trivial compared to the memory capacity of today's computers (on the order of gigabytes), it is for a small illustrative problem. Figure 4.6 shows how the storage requirements increase as function of the number of grid points. It is easy to see how the dense scheme can quickly become prohibitive for large problem sizes, especially those in 3-D. It is obvious from this example that the sparse scheme is the clear winner in terms of memory requirements.

To take advantage of the highly sparse nature of the Jacobian matrix, DASPK was modified to allow a sparse option in the solution of the linear systems. The Scientific Computing Software Library (SCSL) by SGI [72] was chosen to solve the sparse systems for several reasons. First, it provides both iterative and direct sparse solvers. Second, the linear solvers have a simple interface that allowed calls to the library to be incorporated into DASPK with little change to the actual DASPK code. And third, this library has both sequential and parallel versions. Furthermore, the parallel version of the library can be used simply by relinking—no code change is required.

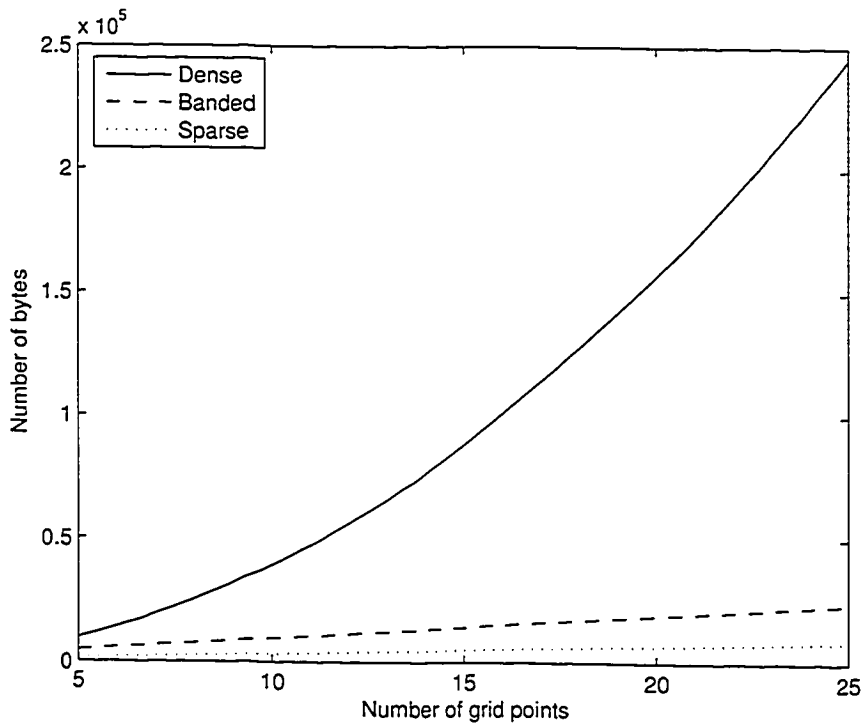

Figure 4.6: Storage requirements for the Jacobian matrix as a function of the number of grid points for a 1-D bidomain cable.

4.4 Numerical Methods for 3-D Propagation Models

The mathematical model to be solved is

$$C_{\mathrm{m}}\frac{\partial V_{\mathrm{m}}}{\partial t} = \frac{1}{\chi}\nabla\cdot D_{\mathrm{i}}\nabla V_{\mathrm{m}} + \frac{1}{\chi}\nabla\cdot D_{\mathrm{i}}\nabla\Phi_{\mathrm{e}} + S(x,t,V_{\mathrm{m}},u) \quad x\in H \tag{4.38}$$

$$\nabla\cdot(D_{\mathrm{i}}+D_{\mathrm{e}})\nabla\Phi_{\mathrm{e}} + \nabla\cdot D_{\mathrm{i}}\nabla V_{\mathrm{m}} = 0 \quad x\in H \tag{4.39}$$

$$\frac{\partial u}{\partial t} = w(V_{\mathrm{m}},u) \tag{4.40}$$

$$n\cdot D_{\mathrm{i}}(\nabla V_{\mathrm{m}} + \nabla\Phi_{\mathrm{e}}) = 0 \quad x\in\partial H \tag{4.41}$$

$$n\cdot D_{\mathrm{e}}\nabla\Phi_{\mathrm{e}} = 0 \quad x\in\partial H \tag{4.42}$$

$$V_{\mathrm{m}}(x,0) = V_{\mathrm{m}0}(x) \tag{4.43}$$

$$\Phi_{\mathrm{e}}(x,0) = \Phi_{\mathrm{e}0}(x) \tag{4.44}$$

$$u(x,0) = u_0(x) \tag{4.45}$$

where

$$S(x,t,V_{\mathrm{m}},u) = -I_{\mathrm{ion}} + I_{\mathrm{app}}$$

We use the same general approach as described in Section 4.3: first discretize the spatial variables and then solve the resulting system of DAEs.

4.4.1 Spatial Discretization

We assume that H is a regular region, or more specifically, a rectangular parallelepiped and so mathematically, $H = [0,l_1]\times[0,l_2]\times[0,l_3]$. First, some notation and definitions are in order. Let N_i for $i = 1,2,3$ be a positive integer and let $\{x_i^{(j)}\}_{j=0}^{N_i}$ be a partition of $[0,l_i]$ such that

$$0 = x_i^{(0)} < x_i^{(1)} < \cdots < x_i^{(N_i-1)} < x_i^{(N_i)} = l_i$$

For simplicity, we consider an equally spaced grid; that is,

$$x_i^{(j)} = j\cdot\Delta x_i$$

where $\Delta x_i = l_i/N_i$. Furthermore, we adopt the following notation:

$$V_{\mathrm{m}}^{(j_1,j_2,j_3)}(t) \equiv V_{\mathrm{m}}(x_1^{(j_1)}, x_2^{(j_2)}, x_3^{(j_3)}, t)$$
$$\Phi_{\mathrm{e}}^{(j_1,j_2,j_3)}(t) \equiv \Phi_{\mathrm{e}}(x_1^{(j_1)}, x_2^{(j_2)}, x_3^{(j_3)}, t)$$
$$\boldsymbol{u}^{(j_1,j_2,j_3)}(t) \equiv \boldsymbol{u}(x_1^{(j_1)}, x_2^{(j_2)}, x_3^{(j_3)}, t)$$
$$u_i^{(j_1,j_2,j_3)}(t) \equiv u_i(x_1^{(j_1)}, x_2^{(j_2)}, x_3^{(j_3)}, t)$$

Interior of the Domain: In the general case where D_{i} is a full matrix, the term $\nabla \cdot D_{\mathrm{i}} \nabla V_{\mathrm{m}}$ will have first-order, second-order, and mixed partial derivatives. For the spatial discretization, we replace all of these derivatives with second-order finite-difference approximations. For example, the terms $\frac{\partial V_{\mathrm{m}}}{\partial x_1}$, $\frac{\partial^2 V_{\mathrm{m}}}{\partial x_1^2}$, and $\frac{\partial^2 V_{\mathrm{m}}}{\partial x_1 \partial x_2}$ are replaced with the following approximations

$$\left.\frac{\partial V_{\mathrm{m}}}{\partial x_1}\right|_{(j_1,j_2,j_3)} \approx \frac{V_{\mathrm{m}}^{(j_1+1,j_2,j_3)} - V_{\mathrm{m}}^{(j_1-1,j_2,j_3)}}{2\Delta x_1} \tag{4.46}$$

$$\left.\frac{\partial^2 V_{\mathrm{m}}}{\partial x_1^2}\right|_{(j_1,j_2,j_3)} \approx \frac{V_{\mathrm{m}}^{(j_1+1,j_2,j_3)} - 2V_{\mathrm{m}}^{(j_1,j_2,j_3)} + V_{\mathrm{m}}^{(j_1-1,j_2,j_3)}}{(\Delta x_1)^2} \tag{4.47}$$

$$\left.\frac{\partial^2 V_{\mathrm{m}}}{\partial x_1 \partial x_2}\right|_{(j_1,j_2,j_3)} \approx \frac{V_{\mathrm{m}}^{(j_1+1,j_2+1,j_3)} - V_{\mathrm{m}}^{(j_1+1,j_2-1,j_3)} - V_{\mathrm{m}}^{(j_1-1,j_2+1,j_3)} + V_{\mathrm{m}}^{(j_1-1,j_2-1,j_3)}}{4\Delta x_1 \Delta x_2} \tag{4.48}$$

$$\text{for } 1 \le j_1 \le N_1 - 1, 1 \le j_2 \le N_2 - 1, 1 \le j_3 \le N_3 - 1$$

Note that equation (4.47) is analogous to the 1-D case given in (4.26). Approximations for other derivatives follow directly from equations (4.46)–(4.48).

Boundary of the Domain: In the case where D_{i} is a general matrix, the term $\boldsymbol{n} \cdot D_{\mathrm{i}} \nabla V_{\mathrm{m}}$ will involve first-order derivatives of V_{m} with respect to all spatial variables. To begin, along the plane $x_1 = 0$, the derivatives $\frac{\partial V_{\mathrm{m}}}{\partial x_2}$ and $\frac{\partial V_{\mathrm{m}}}{\partial x_3}$ can be replaced with approximations analogous to (4.46); for example, $\frac{\partial V_{\mathrm{m}}}{\partial x_2}$ would be replaced by

$$\left.\frac{\partial V_{\mathrm{m}}}{\partial x_2}\right|_{(0,j_2,j_3)} \approx \frac{V_{\mathrm{m}}^{(0,j_2+1,j_3)} - V_{\mathrm{m}}^{(0,j_2-1,j_3)}}{2\Delta x_2} \tag{4.49}$$

For $\frac{\partial V_{\mathrm{m}}}{\partial x_1}$, however, we must use a forward finite difference, and as with the 1-D case, we can use either first-order or second-order approximations. The first-order approximation is

$$\left.\frac{\partial V_{\mathrm{m}}}{\partial x_1}\right|_{(0,j_2,j_3)} \approx \frac{V_{\mathrm{m}}^{(1,j_2,j_3)} - V_{\mathrm{m}}^{(0,j_2,j_3)}}{\Delta x_1} \tag{4.50}$$

while the second-order approximation is

$$\left.\frac{\partial V_m}{\partial x_1}\right|_{(0,j_2,j_3)} \approx \frac{-3V_m^{(0,j_2,j_3)} + 4V_m^{(1,j_2,j_3)} - V_m^{(2,j_2,j_3)}}{2\Delta x_1} \tag{4.51}$$

Likewise, we use backward finite differences to approximate $\frac{\partial V_m}{\partial x_1}$ along the plane $x_1 = l_1$. This same approach is applied along all other boundary regions.

In the end, the discretization process gives rise to a set of DAEs of the same form as the 1-D case:

$$\tilde{I}\frac{dv}{dt} - L_1 v - L_2 \phi - f(t, v, z) = 0 \tag{4.52}$$

$$L_1' v + L_2' \phi = 0 \tag{4.53}$$

$$\frac{dz}{dt} - q(v, z) = 0 \tag{4.54}$$

$$v = v_0 \qquad \phi = \phi_0 \qquad z = z_0 \tag{4.55}$$

The vectors z and q are of size $\eta \cdot N_{pts}$, while the remaining vectors and matrices in the above equations are of size N_{pts} and $N_{pts} \times N_{pts}$, respectively, where now $N_{pts} = (N_1 + 1) \cdot (N_2 + 1) \cdot (N_3 + 1)$.

4.4.2 The Jacobian Matrix

As discussed previously, the total number of equations, N_{eqs}, in the DAE system is $N_{eqs} = (\eta+2) \cdot N_{pts}$, where η is the number of auxiliary variables in the AP model and N_{pts} is the total number of grid points. For a discretized 2-D bidomain model, we have $N_{pts} = (N_1+1) \cdot (N_2+1)$, while for a 3-D model, $N_{pts} = (N_1+1) \cdot (N_2+1) \cdot (N_3+1)$. Consider a 2-D sheet discretized with 8×8 points, and a 3-D block discretized with $4 \times 4 \times 4$ points. The total number of grid points, and therefore the total number of equations, is the same in each case. The structure of the corresponding Jacobian matrix for each of these bidomain models, assuming a Bernus AP, is shown in Figure 4.7. It is apparent from the figure.

4.5 Parallelization of the Source Code

There are several types of parallel computer architectures, as depicted in Figure 4.8. The target architecture influences what method of parallelization we can use, or

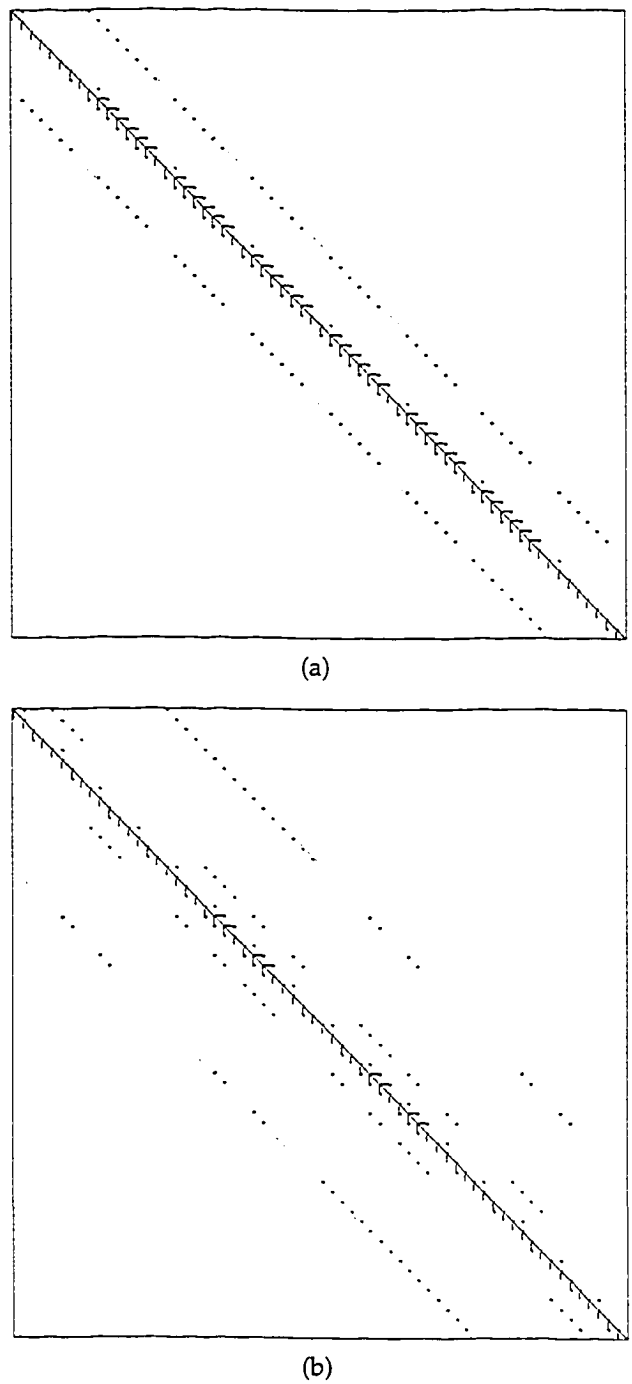

Figure 4.7: Structure of the Jacobian matrix for (a) 2-D and (b) 3-D bidomain models with I_{ion} described by the Bernus AP model. Nonzero elements are indicated by the shaded squares. The dashed lines indicate the bandwidths. The above plots are for a 2-D sheet with 8×8 points and a 3-D block with $4 \times 4 \times 4$ points.

vice versa, our choice of parallelization influences what arhictecture we can run the resultant program on. A *shared memory* architecture is a system in which all CPUs have access to common memory. An example of this type is a symmetric multiprocessor (SMP) computer with two CPUs. A *distributed memory* architecture is a system in which each CPU has private memory. An example of this type is a collection of single-CPU systems connected via a network backbone; such a system is often referred to as a *cluster*. A third *hybrid* architecture exists, which is a combination of the previous two. A networked collection of dual-CPU systems is an example of this architecture; the term cluster is also applied to these types of systems. Yet another type of parallel computers not depicted in Figure 4.8 is the *distributed shared memory* architecture in which memory is physically distributed, but through a hardware (or software) layer it is shared. To the programmer, this type of system behaves as shared memory computer.

Parallelization of software on distributed memory systems necessarily involves the distribution of data across the local memories. This process of data distribution is referred to as *message passing* and it must be explicity coded by the programmer. In contrast, since each CPU has direct and equal access to the memory, software parallelization on shared memory systems does not involve such data copying. Parallel programs are thus easier to implement on these systems.

OpenMP is an industry standard specification for multiprocessing on shared memory systems. Message Passing Interface (MPI) is an application programming interface targeted for multiprocessing on distributed memory systems, though it can also be used on shared memory systems.

4.5.1 Parallelization of the Source Code for Shared Memory Systems: Use of OpenMP

The routine that defines the system of DAEs (the RES routine that DASPK calls many times) was identified as accounting for most of the CPU time of the sequential program. This routine contains a do statement that loops over all grid points in setting up the DAE system. In essence, for each grid point i the loop computes row i of the equations (4.30a), (4.30b), and (4.30c). Using OpenMP compiler directives,

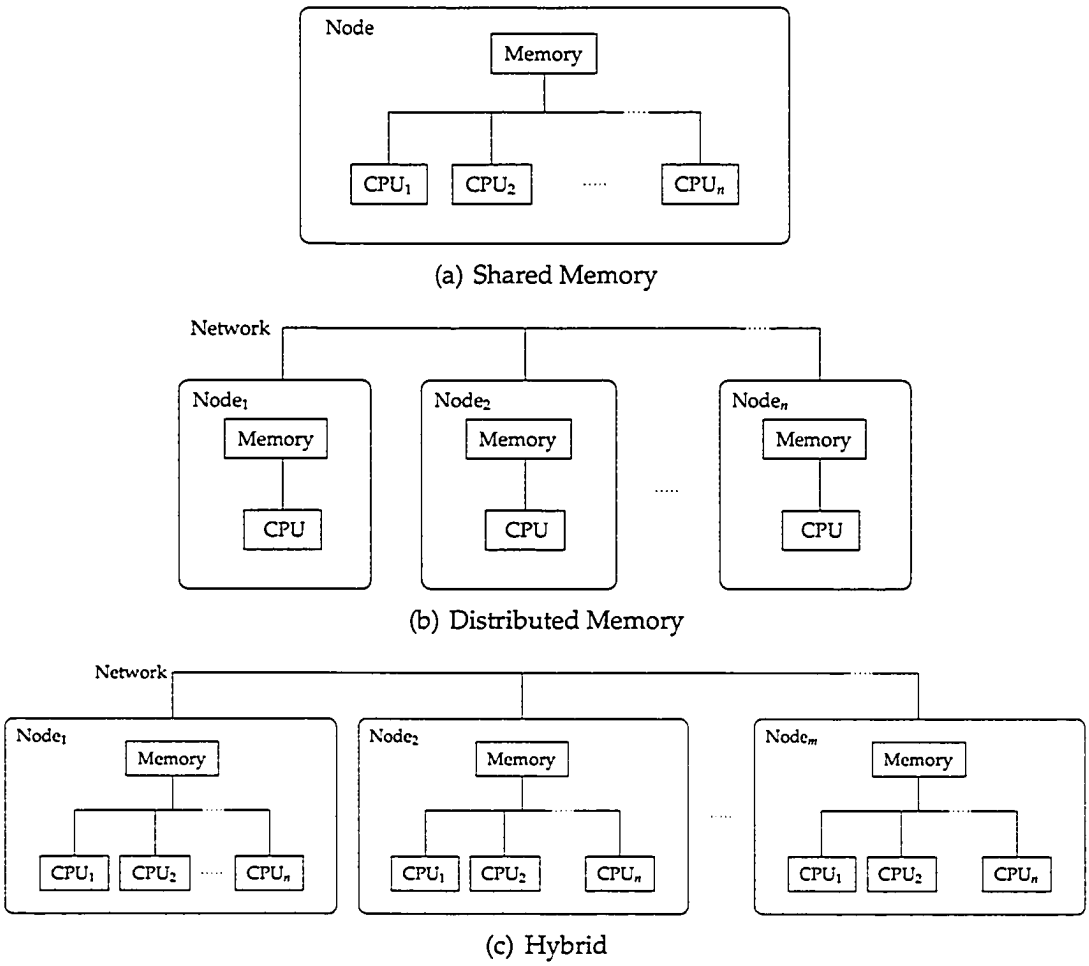

(a) Shared Memory

(b) Distributed Memory

(c) Hybrid

Figure 4.8: Depiction of several types of parallel computer architectures.

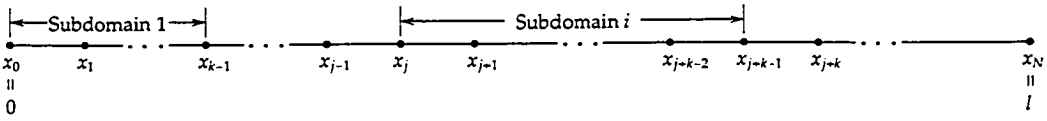

Figure 4.9: Domain decomposition of a 1-D model.

this routine was quickly and easily parallelized. No other sections of the code were parallelizaed, at least not directly. The SCS library mentioned previously provides BLAS, LAPACK, and FFT routines, in addition to the sparse solvers discussed in Section 4.3.4. Parallel versions of many of these routines, particularly the BLAS ones, are provided for shared memory systems and can be used by simply relinking the code with the parallel version of SCS. As DASPK makes use of the BLAS routines, this allowed an indirect parallelization of the code without making any changes.

4.5.2 Parallelization of the Source Code for Distributed Memory Sytems: Use of MPI

Parallelization of the code for a distributed memory system required substantial changes. The data distribution that is inherent in this type of parallelization was accomplished via *domain decomposition*. We begin by illustrating the method for a 1-D model. Consider a cable where the region of interest is $H = [0, l]$ and assume we wish to solve the problem at hand on a distributed memory system with m nodes (and hence m CPUs). A grid of $(N + 1)$ points $\{x^{(i)}\}_{i=0}^{N}$ is imposed on H as before. This set of grid points is then decomposed into m (nearly) equal subsets. Each node solves the portion of the DAE system that corresponds to its grid points. However, the solution of these "subproblems" can not be done independently. Consider subdomain i illustrated in Figure 4.9. In doing the finite-differencing of the spatial derivatives on this region, we require the values of dependent variables at points x_{j-1} and x_{j+k}, which are located on the neighbouring subdomains $i - 1$ and $i + 1$. Our software solves each subproblem independently for some short time interval T_{sync}, after which the nodes exchange information with their neighbours using MPI, and then the process repeats.

4.6 Numerical Experiments

4.6.1 Test Problem with Known Solution

To verify the accuracy of the spatial propagation component of the computer code, we used the program to solve a problem that has a known solution. Consider the following problem:

$$C_{\mathrm{m}}\frac{\partial V_{\mathrm{m}}}{\partial t} = \chi^{-1}\left(\nabla\cdot\boldsymbol{D}_{\mathrm{i}}\nabla V_{\mathrm{m}} + \nabla\cdot\boldsymbol{D}_{\mathrm{i}}\nabla\Phi_{\mathrm{e}}\right) + S(x,t) \tag{4.56a}$$

$$\nabla\cdot(\boldsymbol{D}_{\mathrm{i}}+\boldsymbol{D}_{\mathrm{e}})\nabla\Phi_{\mathrm{e}} + \nabla\cdot\boldsymbol{D}_{\mathrm{i}}\nabla V_{\mathrm{m}} = 0 \tag{4.56b}$$

$$\frac{\partial V_{\mathrm{m}}}{\partial \boldsymbol{n}} = 0 \tag{4.56c}$$

$$\frac{\partial \Phi_{\mathrm{e}}}{\partial \boldsymbol{n}} = 0 \tag{4.56d}$$

$$V_{\mathrm{m}}(x,t) = -\frac{\sum_{i=1}^{3}\frac{g_{\mathrm{i},x_i}+g_{\mathrm{e},x_i}}{L_i^2}}{\sum_{i=1}^{3}\frac{g_{\mathrm{i},x_i}}{L_i^2}}\prod_{i=1}^{3}\cos\left(\frac{\pi x_i}{L_i}\right) \tag{4.56e}$$

$$\Phi_{\mathrm{e}}(x,0) = \prod_{i=1}^{3}\cos\left(\frac{\pi x_i}{L_i}\right) \tag{4.56f}$$

where

$$\boldsymbol{D}_{\mathrm{i}} = \begin{bmatrix} g_{\mathrm{i},x_1} & 0 & 0 \\ 0 & g_{\mathrm{i},x_2} & 0 \\ 0 & 0 & g_{\mathrm{i},x_3} \end{bmatrix}, \qquad \boldsymbol{D}_{\mathrm{e}} = \begin{bmatrix} g_{\mathrm{e},x_1} & 0 & 0 \\ 0 & g_{\mathrm{e},x_2} & 0 \\ 0 & 0 & g_{\mathrm{e},x_3} \end{bmatrix}$$

$$S(x,t) = \left[C_{\mathrm{m}}\frac{\sum_{i=1}^{3}\frac{g_{\mathrm{i},x_i}+g_{\mathrm{e},x_i}}{L_i^2}}{\sum_{i=1}^{3}\frac{g_{\mathrm{i},x_i}}{L_i^2}} - \frac{\pi^2}{\chi}\sum_{i=1}^{3}\frac{g_{\mathrm{e},x_i}}{L_i^2}\right]e^{-t}\prod_{i=1}^{3}\cos\left(\frac{\pi x_i}{L_i}\right)$$

The exact solution to this problem is given by

$$V_{\mathrm{m}}(x,t) = -\frac{\sum_{i=1}^{3}\frac{g_{\mathrm{i},x_i}+g_{\mathrm{e},x_i}}{L_i^2}}{\sum_{i=1}^{3}\frac{g_{\mathrm{i},x_i}}{L_i^2}}e^{-t}\prod_{i=1}^{3}\cos\left(\frac{\pi x_i}{L_i}\right) \tag{4.57}$$

$$\Phi_{\mathrm{e}}(x,t) = e^{-t}\prod_{i=1}^{3}\cos\left(\frac{\pi x_i}{L_i}\right) \tag{4.58}$$

Note that we have maintained the same notation has used earlier in this chapter, however, V_{m} and Φ_{e} no longer correspond to potentials.

The code developed in Chapter 3 uses a constant time step to advance the solution. In contrast, the code developed in this chapter employs the software package DASPK, which uses adaptive time-stepping [10]. Time steps are chosen to control the local error on each step according to tolerances provided by the user. Briefly, if $atol_i$ and $rtol_i$ are the absolute and relative tolerances provided by the user for variable i, then DASPK chooses the time steps so that

$$\text{local error in } y_i \leq rtol_i|y_i| + atol_i$$

where y_i is the value of variable i. As with practically all modern ODE/DAE software packages, DASPK monitors the local error and does not attempt to control the global or true error (see either references [4] or [8] for further discussion of this topic). In short though, the global error in the numerical solution is comparable to the error tolerances, and in general, reducing the tolerances will usually result in a more accurate solution.

We solved problem (4.56) for $0 \leq t \leq 8$ on the rectangular volume $H = \{(x_1, x_2, x_3) \mid 0 \leq x_1 \leq 0.8, 0 \leq x_2 \leq 0.8, 0 \leq x_3 \leq 0.4\}$ for three uniform meshes: (i) $\Delta x = 0.08$ corresponding to $11 \times 11 \times 6$ grid points; (ii) $\Delta x = 0.04$ corresponding to $21 \times 21 \times 11$ grid points; and (iii) $\Delta x = 0.02$ corresponding to $41 \times 41 \times 21$ grid points. Furthermore, the problem was solved with two different absolute tolerances for each mesh: $atol$ = 1.0E−3 and $atol$ = 1.0E−4. In all cases, the relative tolerance was set to zero, thus giving pure absolute error control. Solution values were output at times $t = 1, 2, \ldots, 8$, and the RMS errors and maximum deviations were calculated as before (see equations (3.22) and (3.23)).

Table 4.2 shows the RMS errors and maximum deviations for the bidomain code when solving problem (4.56). As can be seen from the data, decreasing the absolute tolerance results in smaller errors. Likewise, decreasing the spatial stepsize also produces a more accurate numerical solution, indicating that the code is working as expected.

4.6.2 Block with Rotational Anisotropy

Methods: To further test the bidomain code, we repeated the 'Block Type I' simulation from Chapter 3. In short, we simulated propagated electrical activity

Table 4.2: RMS errors and maximum deviations for the bidomain code when solving a test problem that has a known solution.

(a) RMS Errors for V_m

	atol	
Δx	1.0E−3	1.0E−4
0.08	0.009115	0.008993
0.04	0.000470	0.000442
0.02	0.000046	0.000042

(b) Maximum Deviations for V_m

	atol	
Δx	1.0E−3	1.0E−4
0.08	0.080717	0.080112
0.04	0.005838	0.005457
0.02	0.000608	0.000448

(c) RMS Errors for Φ_e

	atol	
Δx	1.0E−3	1.0E−4
0.08	0.001555	0.001539
0.04	0.000119	0.000081
0.02	0.000066	0.000011

(d) Maximum Deviations for Φ_e

	atol	
Δx	1.0E−3	1.0E−4
0.08	0.013244	0.013160
0.04	0.001259	0.000980
0.02	0.000477	0.000049

in a 3-D block of cardiac tissue with rotational anisotropy. Description of the block geometry is given on page 34. Unlike the previous monodomain simulation, we make no assumption of an equal anisotropy ratio. Excitation was initiated by applying a current stimulus to $4 \times 4 \times 2$ points at the center of the top of the block. The propagation parameters for the bidomain simulation are listed in Table 4.3.

Simulations were performed on the Westgrid complex of SGI computers located at the University of Alberta. The program was compiled with version 7.4 of the MIPSpro Fortran compiler and parallelized using OpenMP.

Results: Figure 4.10 shows the results of the bidomain 'Block Type I' simulation. Selected cross-sections through the block are displayed. From top to bottom, the fiber directions in the panels make angles of 0°, 42.4°, 47.6°, and 90°, respectively, relative to the horizontal side of the figures. Column (a) shows the isochrones of activation time; the block was completely activated within 22 ms. Due to the rotational anisotropy, the isochrones are elliptical in shape and rotate counterclockwise from top to bottom with the fiber direction, though the amount of rotation is less than that of the fibers. Columns (b) and (c) display snapshots of the interstitial potential at 8 and 12 ms from the start of the simulation. In the

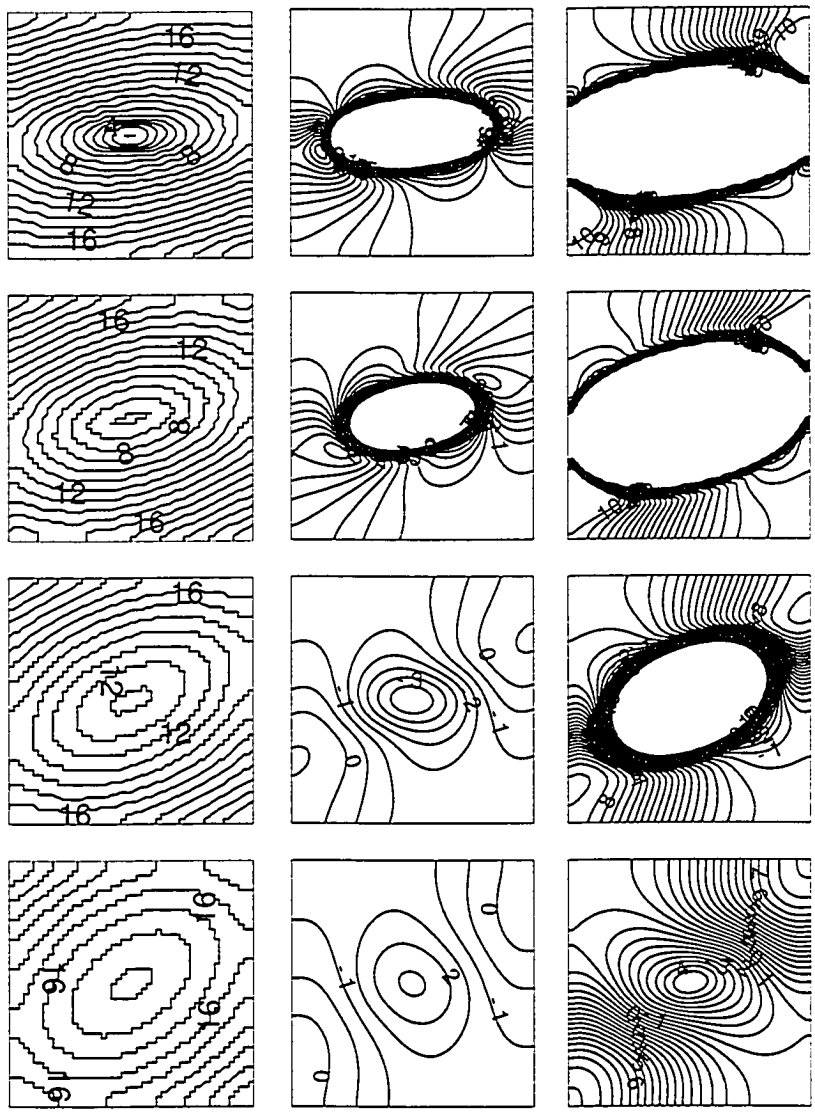

Figure 4.10: Isochrones of propagated excitation and contour lines of interstitial potential for the bidomain model solved via the method of lines. Stimulation was applied at the center of the two upper planes of a block of cardiac tissue of dimension 1 cm × 1 cm × 0.3 cm. Column (a) shows successive isochrones adisplayed at 1 ms intervals with every fourth one labeled. Columns (b) and (c) show contour lines of interstitial potential at $t = 8$ and 12 ms from the beginning of the simulation. Interstitial potential lines are labeled in millivolts and traced only for values between −10 and 10 mV. Layers illustrated here refer to slices through the block parallel with the xy-plane. The top (bottom) layer corresponds to the epi(endo)-cardial surface. From top to bottom, the fiber directions in the panels make angles, relative to the horizontal side of the figures, of 0°, 42.4°, 47.6°, and 90°, respectively.

Table 4.3: Propagation parameters for bidomain 'Block Type I' simulation. Values for surface-to-volume ratio and conductivities are taken from Colli Franzone and Guerri [17].

Intracellular transverse conductivity g_{it}	0.417 mS/cm
Intracellular longitudinal conductivity g_{il}	2.0 mS/cm
Interstitial transverse conductivity g_{et}	1.25 mS/cm
Interstitial longitudinal conductivity g_{el}	2.5 mS/cm
Membrane capacitance C_m	1.0 μF/cm^2
Surface-to-volume ratio χ	1000.0 cm^{-1}
Spatial steps	
$hx = hy$	0.020 cm
hz	$0.01\bar{6}$ cm
Current stimulus I_{app}	200.0 μA/cm^2
Duration of stimulus	0.5 ms

top panel of column (b), the potential map has two maxima and two minima that lie approximately along the major and minor axis, respectively, of the elliptical isochrones in column (a). Proceeding through the depth of the tissue, the two maxima and two minima rotate like the axes of the elliptical isochrones, which is illustrated best in the second panel down in column (b) and the third panel down in column (c). Again, this rotation is less than that of the fiber rotation. These results agree with those of Colli Franzone and Guerri [17].

Chapter 5

Implementing Unequal Anisotropy Ratio

Bidomain models for simulating the propagation of electrical activation in the heart treat the myocardium as an anisotropic excitable medium with conductivity coefficients g_{il}, g_{it}, g_{el}, and g_{et}, where i and e refer to intracellular and extracellular space, and l and t indicate whether conductivity is along (l) or transverse (t) to the local fiber direction. These models are made computationally tractable by the *equal anisotropy ratio assumption*, which states that $g_{el}/g_{il} = g_{et}/g_{it} = r$, for some scalar constant r. Although it is doubtful that this assumption is valid, it has been the only means of reducing the complex coupled systems of nonlinear partial differential equations to a single reaction-diffusion problem. In this chapter, we introduce a simple perturbation argument that yields an equivalent reduction—with a de-coupling tensor expressed in terms of the harmonic means $g_{il}g_{el}/(g_{il}+g_{el})$ and $g_{it}g_{et}/(g_{it}+g_{et})$ of the conductivity parameters—thus preserving the critical information conveyed by conductivity parameters without resorting to the assumption regarding their ratios. Numerical simulations in a realistic tissue volume were performed to assess the consequences of this alternate formulation.

5.1 Introduction

Bidomain models of the propagation of electrical activation in the anisotropic cardiac tissue have been developed in the form of coupled systems of ordinary and partial differential equations [13, 18, 17, 23, 29, 37]. In these models, the elliptic partial differential equations arise from the laws of conservation of current, a nonlinear parabolic equation describes propagation, and ordinary differential equations describe the transmembrane ionic currents of cardiac cells. The anisotropy in the ventricular wall is usually defined by the transmural rotation of the myocardial fibers.

Recall from Chapter 2 that the bidomain model is

$$\chi C_m \frac{\partial V_m}{\partial t} - \nabla \cdot \boldsymbol{D}_i \nabla V_m = \nabla \cdot \boldsymbol{D}_i \nabla \Phi_e - \chi I_{ion} + \chi I_{app} \quad x \in H \tag{5.1a}$$

$$\nabla \cdot (\boldsymbol{D}_i + \boldsymbol{D}_e) \nabla \Phi_e + \nabla \cdot \boldsymbol{D}_i \nabla V_m = 0 \quad x \in H \tag{5.1b}$$

$$\boldsymbol{n} \cdot \boldsymbol{D}_i (\nabla V_m + \nabla \Phi_e) = 0 \quad x \in \partial H \tag{5.1c}$$

$$\boldsymbol{n} \cdot \boldsymbol{D}_e \nabla \Phi_e = 0 \quad x \in \partial H \tag{5.1d}$$

$$V_m(x, 0) = V_{m0}(x) \tag{5.1e}$$

$$\Phi_e(x, 0) = \Phi_{e0}(x) \tag{5.1f}$$

Solving this system is a formidable task. The problem can be made computationally tractable by introducing the *equal anisotropy ratio assumption,* which states that $g_{el}/g_{il} = g_{et}/g_{it} = r$ for some scalar constant r (typically with $r = 1$) [18, 17, 37]. This is precisely the assumption that we made in Chapter 3, because it permits the decoupling of (5.1a) and (5.1b) to yield the single reaction-diffusion problem for V_m in H

$$\chi C_m \frac{\partial V_m}{\partial t} = \nabla \cdot \boldsymbol{D}_b \nabla V_m - \chi I_{ion} + \chi I_{app} \quad x \in H \tag{5.2a}$$

$$\boldsymbol{n} \cdot \boldsymbol{D}_i \nabla V_m = 0 \quad x \in \partial H \tag{5.2b}$$

$$V_m(x, 0) = V_{m0}(x) \tag{5.2c}$$

where $\boldsymbol{D}_b = r/(r+1)\boldsymbol{D}_i$ is the bulk conductivity tensor. Although there is still some uncertainty regarding the values of g, it is generally acknowledged that they do *not* satisfy the equal anisotropy ratio assumption [66, 89]. In fact, there have been studies [34, 40] which suggest that adopting this assumption may lead to an incorrect analysis of the propagation dynamics in the myocardium. The most recent studies have used values close to $g_{el} : g_{il} = 2.5 : 2$ and $g_{et} : g_{it} = 3 : 1$ [17, 34]. In Section 5.2, we introduce a simple perturbation argument based on independent analytical and experimental evidence [14, 66, 89], which permits the decoupling of equations (5.1a) and (5.1b) and leads to a reaction-diffusion problem where the decoupling tensor is $\boldsymbol{D}_h = A\boldsymbol{D}_h^* A^T$, with $\boldsymbol{D}_h^* = \operatorname{diag}\left(\frac{g_{il}g_{el}}{g_{il}+g_{el}}, \frac{g_{it}g_{et}}{g_{it}+g_{et}}, \frac{g_{it}g_{et}}{g_{it}+g_{et}}\right)$ given in terms of the harmonic means of the original conductivity coefficients. $\boldsymbol{D}_h$ reduces to $\boldsymbol{D}_b$ in the special case of equal anisotropy ratios.

In Section 5.3, we discuss the methods employed. In Section 5.4, the decouple model is solved numerically for a uniformly anisotropic myocardial tissue volume, and the propagation dynamics associated with the *equal anisotropy ratio assumption* and the harmonic mean decoupling procedure are examined. The tissue volume is of realistic size (5 cm×5 cm×1 cm) consisting of 100×100×20 excitable cells. Since the propagation of cardiac activation is highly dependent on the excitatory mechanism involved, one must also incorporate realistic cell-membrane dynamics in order to obtain an accurate measure of the effect of the two decomposition approaches. Consequently, we utilize the Bernus model of transmembrane ionic currents [7]. Finally, we compare the results of the decoupled monodomain model using the implementation of Chapter 3 with the bidomain model and the implementation detailed in Chapter 4.

5.2 Derivation of Decoupled Equations

We now introduce an alternative method of de-coupling, which avoids the equal anisotropy ratio assumption and preserves much of the critical information conveyed by the conductivity values g in $\boldsymbol{D}_\mathrm{i}$ and $\boldsymbol{D}_\mathrm{e}$. Recall that the intracellular and extracellular conductivity tensors are given by $\boldsymbol{D}_\mathrm{i} = A\boldsymbol{D}_\mathrm{i}^{*}A^T = A\,\mathrm{diag}(g_\mathrm{il}, g_\mathrm{it}, g_\mathrm{it})A^T$ and $\boldsymbol{D}_\mathrm{e} = A\boldsymbol{D}_\mathrm{e}^{*}A^T = A\,\mathrm{diag}(g_\mathrm{el}, g_\mathrm{et}, g_\mathrm{et})A^T$, where the longitudinal fiber direction at each point is defined by A in terms of the angles ϕ and θ relative to the global coordinate system. Let M be the diagonal matrix $M = \mathrm{diag}(\alpha g_\mathrm{il}, \beta g_\mathrm{it}, \beta g_\mathrm{it})$ with $\alpha = \frac{g_\mathrm{il}}{g_\mathrm{il}+g_\mathrm{el}}$ and $\beta = \frac{g_\mathrm{it}}{g_\mathrm{it}+g_\mathrm{et}}$. Then adding $\nabla\cdot AMA^T\nabla V_\mathrm{m}$ to both sides of the differential equation in (5.1a) and substituting $\nabla\cdot(\boldsymbol{D}_\mathrm{i}+\boldsymbol{D}_\mathrm{e})\nabla\Phi_\mathrm{e} + \nabla\cdot\boldsymbol{D}_\mathrm{i}\nabla V_\mathrm{m} = 0$ from (5.1b) into the result gives

$$\chi C_\mathrm{m}\frac{\partial V_\mathrm{m}}{\partial t} - \nabla\cdot\left(A\,\mathrm{diag}\left(\tfrac{g_\mathrm{il}g_\mathrm{el}}{g_\mathrm{il}+g_\mathrm{el}}, \tfrac{g_\mathrm{it}g_\mathrm{et}}{g_\mathrm{it}+g_\mathrm{et}}, \tfrac{g_\mathrm{it}g_\mathrm{et}}{g_\mathrm{it}+g_\mathrm{et}}\right)A^T\right)\nabla V_\mathrm{m} = -\chi I_\mathrm{ion} + \chi I_\mathrm{app}$$
$$+\epsilon\left\{\nabla\cdot\left(A\,\mathrm{diag}(g_\mathrm{il}+g_\mathrm{el}, 0, 0)A^T\right)\nabla\Phi_\mathrm{e} + \nabla\cdot\left(A\,\mathrm{diag}(g_\mathrm{il}, 0, 0)A^T\right)\nabla V_\mathrm{m}\right\} \quad (5.3)$$

where the dimensionless ϵ is given by

$$\epsilon = \frac{g_\mathrm{il}g_\mathrm{et} - g_\mathrm{it}g_\mathrm{el}}{(g_\mathrm{il}+g_\mathrm{el})(g_\mathrm{it}+g_\mathrm{et})}$$

and satisfies $\epsilon < 1$ for all possible values of the parameters g. For example, $\epsilon < 0.06$ for the parameter values used in the studies [17, 34], Let

$$V_{\mathrm{m}}(x,t) = \sum_{n=0}^{\infty} \epsilon^n V_{\mathrm{m},n}(x,t)$$

Then, up to the leading order term in the expansion, the differential equation in (5.3) is satisfied with $\epsilon = 0$. However, there is additional evidence to support the argument that the ϵ term can be neglected in computing the membrane potentials. It has long been known that continuous models cannot entirely explain the propagation of excitation in myocardial tissue. For example, heart action potentials have different risetimes and durations depending on direction (particularly transversely) and this cannot be adequately simulated in a continuous model [89]. This is due to many factors, such as the shape and packing of individual heart cells, the fact that g_{il} is 5 to 10 times greater than g_{it}, and the fact that there are more intracellular gap junctions in the longitudnal direction than in the transverse direction [74].

Thus, there is a discrete component to the overall propagation in myocardial tissue, and the medium can be interpreted as behaving in part as if it were composed of collections of one-dimensional cables. Therefore, one would expect that the conservation of current law in the fiber direction (i.e., $\nabla \cdot (A\,\mathrm{diag}(g_{\mathrm{il}} + g_{\mathrm{el}}, 0, 0)A^T)\nabla\Phi_{\mathrm{e}} + \nabla \cdot (A\,\mathrm{diag}(g_{\mathrm{il}}, 0, 0)A^T)\nabla V_{\mathrm{m}} = 0$; cf. (5.1b)) would be satisfied locally, and this is precisely the term multiplying ϵ in (5.3). Furthermore, it is known from analytical and experimental evidence [14, 66] that the ratio of transverse to longitudinal conduction velocities of the wave front in myocardial tissue satisfies

$$\frac{\theta_{\mathrm{t}}}{\theta_{\mathrm{l}}} = \left(\frac{g_{\mathrm{it}} g_{\mathrm{et}}/(g_{\mathrm{it}} + g_{\mathrm{et}})}{g_{\mathrm{il}} g_{\mathrm{el}}/(g_{\mathrm{il}} + g_{\mathrm{el}})} \right)^{1/2}$$

which again will be the case if ϵ is set to zero in (5.3). Hence, there are sound physiological as well as analytical reasons for assuming that, in the case of myocardial tissue, the term $\epsilon\{\nabla \cdot (A\,\mathrm{diag}(g_{\mathrm{il}} + g_{\mathrm{el}}, 0, 0)A^T)\nabla\Phi_{\mathrm{e}} + \nabla \cdot (A\,\mathrm{diag}(g_{\mathrm{il}}, 0, 0)A^T)\nabla V_{\mathrm{m}}\}$ will be sufficiently small to justify neglecting its influence on propagating wave

patterns and that (5.1a) and (5.1b) can be replaced by the decoupled problem

$$\chi C_m \frac{\partial V_m}{\partial t} - \nabla \cdot \boldsymbol{D}_h \nabla V_m = -\chi I_{ion} + \chi I_{app} \quad x \in H \tag{5.4a}$$

$$\boldsymbol{n} \cdot \boldsymbol{D}_i \nabla V_m = 0 \quad x \in \partial H \tag{5.4b}$$

$$V_m(x,0) = V_{m0}(x) \tag{5.4c}$$

with $D_h = AD_h^* A^T$ and $D_h^* = \mathrm{diag}\left(\frac{g_{il}g_{el}}{g_{il}+g_{el}}, \frac{g_{it}g_{et}}{g_{it}+g_{et}}, \frac{g_{it}g_{et}}{g_{it}+g_{et}}\right)$.

5.3 Methods

Numerical Methods: Let H be represented by a uniformly anisotropic slab $H = [0, L_1] \times [0, L_2] \times [0, L_3]$ in which the longitudinal fiber direction is taken to be parallel to the x-axis at each point, so that l refers to the x direction and t to the y and z directions. The decoupled problem (5.4) for the membrane potential V_m is then

$$\chi C_m \frac{\partial V_m}{\partial t} - \left\{ \frac{g_{il}g_{el}}{g_{il}+g_{el}} \frac{\partial^2 V_m}{\partial x^2} + \frac{g_{it}g_{et}}{g_{it}+g_{et}} \frac{\partial^2 V_m}{\partial y^2} + \frac{g_{it}g_{et}}{g_{it}+g_{et}} \frac{\partial^2 V_m}{\partial z^2} \right\} = -\chi I_{ion} + \chi I_{app} \tag{5.5a}$$

$$\left.\frac{\partial V_m}{\partial x}\right|_{x=0,L_1} = 0, \quad \left.\frac{\partial V_m}{\partial y}\right|_{y=0,L_2} = 0, \quad \left.\frac{\partial V_m}{\partial z}\right|_{z=0,L_3} = 0 \tag{5.5b}$$

$$V_m(x,y,z,0) = V_{m0}(x,y,z) \tag{5.5c}$$

We solve the above system using the numerical methods developed in Chapter 3. For comparison purposes, we solve the corresponding bidomain model using the methods developed in Chapter 4.

Tissue Block for Comparison of Equal and Unequal Anisotropy Ratio: We consider a 5 cm × 5 cm × 1 cm block that consists of homogeneous myocardial tissue with uniform anisotropy; that is, we neglect the rotation and curvature of the fibers. Furthermore, the fibers are assumed to run parallel with the x-axis. The z-axis is vertical, and the planes $z = 0$ and $z = 1$ represent the endo- and epicardial surfaces, respectively. Using a uniform spatial step of 0.05 cm, the block was discretized by 101 × 101 × 21 nodes. To initiate wave propagation, a current stimulus was applied to the right vertex of the top plane (the epicardial surface). With only modification of the conductivity values, this same setup was used for both the

Table 5.1: Simulation parameters for equal and unequal anisotropy.

Common parameters	
Membrane capacitance C_m	1.0 $\mu F/cm^2$
Surface-to-volume ratio χ	500.0 cm^{-1}
Spatial step $\Delta x = \Delta y = \Delta z$	0.05 cm
Time step Δt	0.1 ms
Current stimulus I_{app}	100.0 $\mu A/cm^2$
Duration of current stimulus	0.5 ms
Equal anisotropy parameters	
Intracellular transverse conductivity g_{it}	0.5 mS/cm
Intracellular longitudinal conductivity g_{il}	2.0 mS/cm
Anisotropy ratio r	1.0
Unequal anisotropy parameters	
Intracellular transverse conductivity g_{it}	$0.41\bar{6}$ mS/cm
Intracellular longitudinal conductivity g_{il}	2.0 mS/cm
Interstitial transverse conductivity g_{et}	1.25 mS/cm
Interstitial longitudinal conductivity g_{el}	2.5 mS/cm

equal- and unequal-anisotropy-ratio case. The propagation parameters are given in Table 5.1.

Tissue Block for Comparison of Monodomain and Bidomain Models: We consider a 0.8 cm × 0.8 cm × 0.2 cm block that consists of homogeneous myocardial tissue with uniform anisotropy. As before, the fibers are assumed to run parallel with the x-axis, and the z-axis is vertical, so that the planes $z = 0$ and $z = 0.2$ represent the endo- and epicardial surfaces, respectively. The block was discretized into 51 × 51 × 26 points. To initiate wave propagation, a current stimulus was applied to the center of the bottom plane (the endocardial surface). The propagation parameters are given in Table 5.2.

5.4 Results

Figure 5.1 shows the wave fronts elicited by current stimulation applied to 3×3×3 points at the top right corner of the block. The wave fronts are qualitatively similar for both the equal-anisotropy case (panel A) and the unequal-anisotropy case (panel B). However, the time required for total activation of the block is

Table 5.2: Simulation parameters for comparison of monodomain and bidomain models.

Common parameters	
Membrane capacitance C_m	1.0 $\mu F/cm^2$
Surface-to-volume ratio χ	1400.0 cm^{-1}
Intracellular transverse conductivity g_{it}	0.19 mS/cm
Intracellular longitudinal conductivity g_{il}	1.74 mS/cm
Interstitial transverse conductivity g_{et}	2.36 mS/cm
Interstitial longitudinal conductivity g_{el}	6.25 mS/cm
Spatial step $\Delta x = \Delta y$	0.016 cm
Spatial step Δz	0.008 cm
Current stimulus I_{app}	100.0 $\mu A/cm^2$
Duration of current stimulus	2.0 ms
Monodomain parameters	
Time step Δt	0.01 ms
Bidomain parameters	
Time step Δt	Adaptive

considerably different in these two cases: for the equal-anisotropy case, the bottom left corner of the block was activated at $t = 246$ ms; for the unequal-anisotropy case, activation reached this same point at $t = 197$ ms. Difference in total activation times coincides with differences in propagation velocities. In the equal-anisotropy case, the measured longitudinal and transverse velocities were 0.75 m/s and 0.23 m/s, respectively, whereas these velocities in the unequal-anisotropy case were 0.80 m/s and 0.29 m/s.

Figure 5.2 shows the wave fronts elicited by current stimulation applied to $3 \times 3 \times 2$ points at the center of the endocardial surface of the block. The wave fronts are qualitatively similar for both the monodomain model (panel (a)) and the bidomain model (panel (b)). Moreover, the time required for total activation of the block shows good agreement. For the monodomain model, all points were activated within 33 ms, while all points in the bidomain model were activated within 32 ms. The root-mean-square (RMS) error between the two results was found to be 0.550 ms. Figure 5.3 shows the membrane potential from sample points.

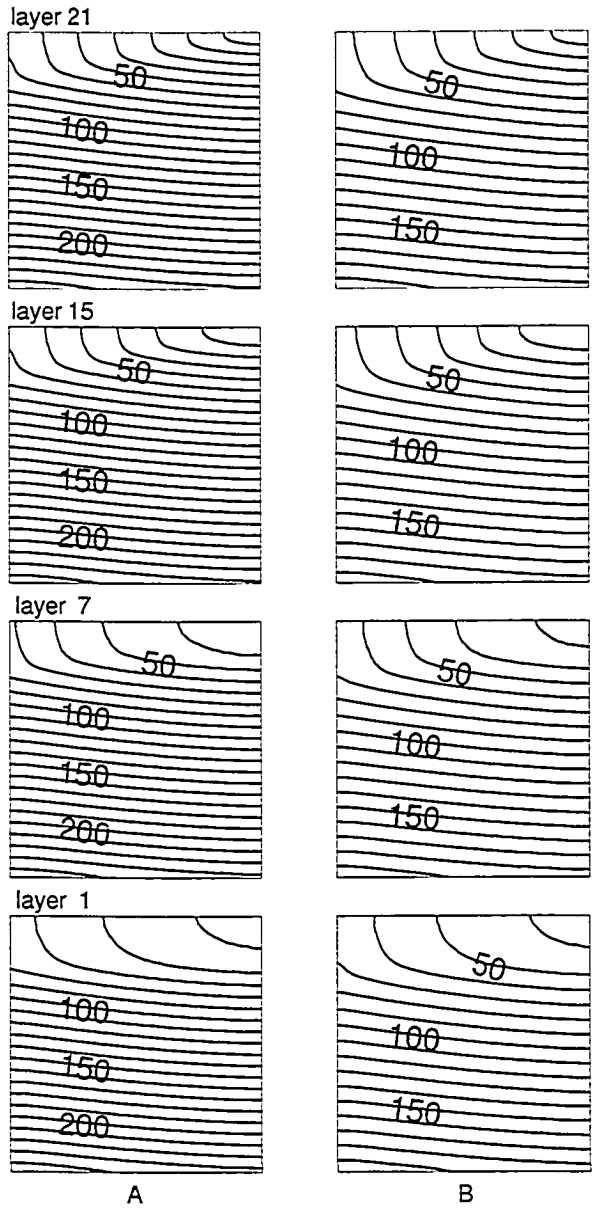

Figure 5.1: Wave fronts evoked by current stimulation applied to the top right vertex of the block. Successive isochrones (i.e., contour lines of activation time in milliseconds) are displayed at 10 ms intervals. The block represents a 5 cm × 5 cm × 1 cm homogeneous slab of myocardial tissue with uniform anisotropy. Layers illustrated here refer to slices through the block parallel to the xy-plane, with layer 1 representing the bottom of the block. Panel A is the equal-anisotropy case, and panel B the unequal-anisotropy case. The computational mesh is $101 \times 101 \times 21$ points.

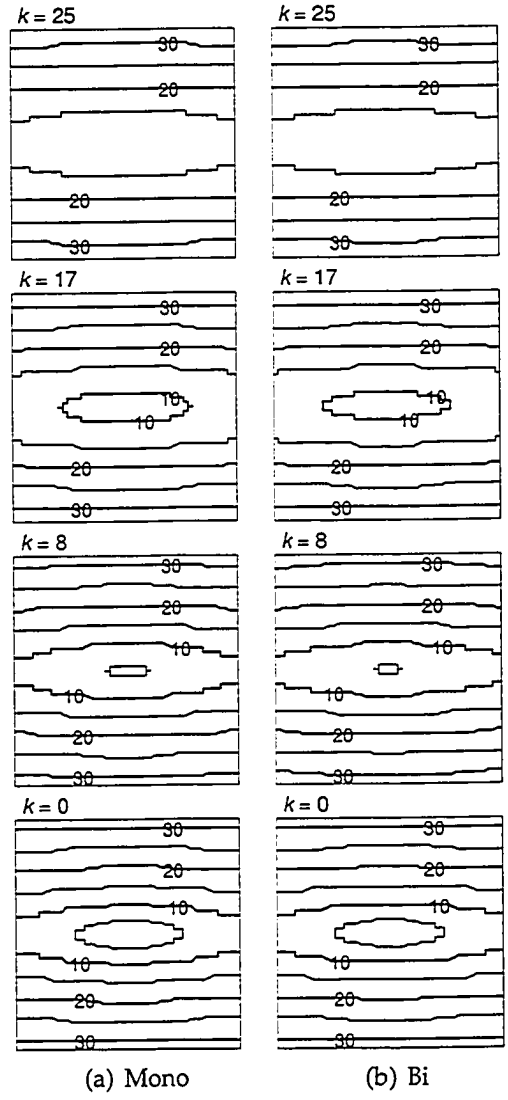

(a) Mono (b) Bi

Figure 5.2: Comparison of wave fronts from the monodomain model using harmonic means with the bidomain model. The applied stimulus and conductivities are the same in each case. Activation isochrones are displayed at 5 ms intervals with every 10 ms isochrone labelled. The block represents a $0.8 \times 0.8 \times 0.2$ cm homogeneous slab of myocardial tissue with uniform anisotropy; i.e., the fiber direction is constant and parallel with the horizontal side of the figure. A computational grid of $51 \times 51 \times 26$ points was imposed on the block of tissue. A brief 100 μA/cm^2 stimulus was applied to points $(x^{(i)}, y^{(j)}, z^{(k)})$ where $24 \leq i \leq 26$, $24 \leq j \leq 26$, and $1 \leq k \leq 2$. Layers illustrated here refer to slices through the block parallel to the xy-plane at the indicated k value, where $k = 0$ is the bottom of the block. The conductivity values (mS/cm) were $g_{il} = 1.74$, $g_{it} = 0.19$, $g_{el} = 6.25$, and $g_{et} = 2.36$.

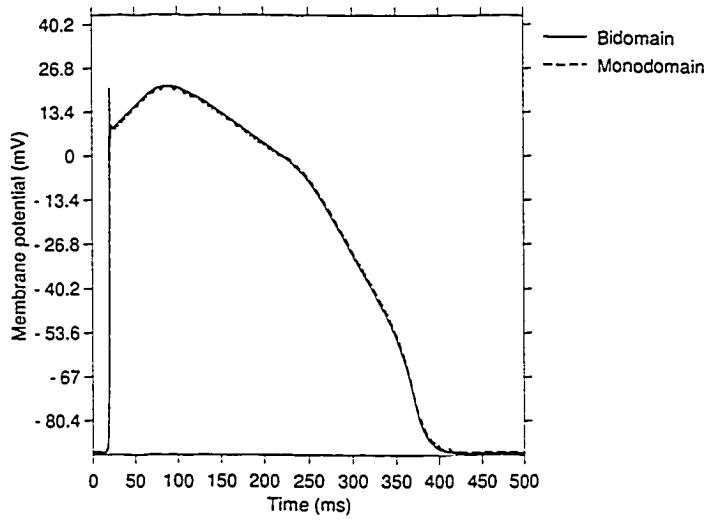

(a) $k = 0$

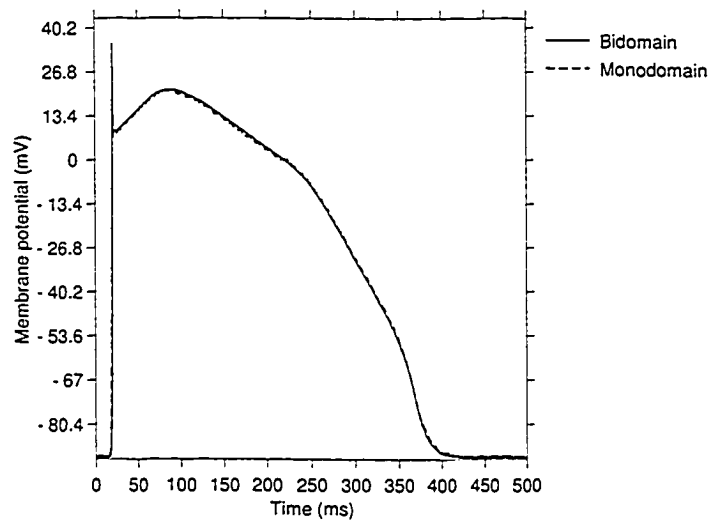

(b) $k = 25$

Figure 5.3: Comparison of membrane potential from the monodomain model using harmonic means with the bidomain model. The plot shows the membrane potential corresponding to Figure 5.2 for a point on the 20 ms activation isochrone. For the bottom layer (i.e., $k = 0$), the point is $(25, 40, 0)$ for both the monodomain and bidomain models. For the top layer (i.e., $k = 25$), the point is $(25, 37, 25)$ for the monodomain model and $(25, 38, 25)$ for the bidomain model. Note the excellent agreement between the monodomain and bidomain models.

To achieve a better agreement between the two models, the conductivity values in the monodomain model were varied and the results compared against the 'default' bidomain model. Figure 5.2 shows the wave fronts for the case where the interstitial conductivity values in the monodomain model were increased by 20%. The root-mean-square (RMS) error between the two results was determined to be 0.414 ms.

5.5 Discussion

Bidomain models for simulating the propagation of electrical activation in the heart usually adopt the *equal anisotropy ratio assumption* to reduce the complex coupled systems of nonlinear partial differential equations to a single reaction-diffusion problem for the myocardial tissue alone. We achieved an equivalent reduction by using the decoupling tensor expressed in terms of the harmonic means of the conductivity parameters; this approach preserves the critical information conveyed by the conductivity parameters without making any assumption regarding their ratios. The decoupled problem yields results that are qualitatively similar to those produced under the assumption of an equal-anisotropy ratio. Moreover, there is close agreement bewteen the decoupled and the original bidomain model, which justifies use of the decoupled model when computational resources are limited.

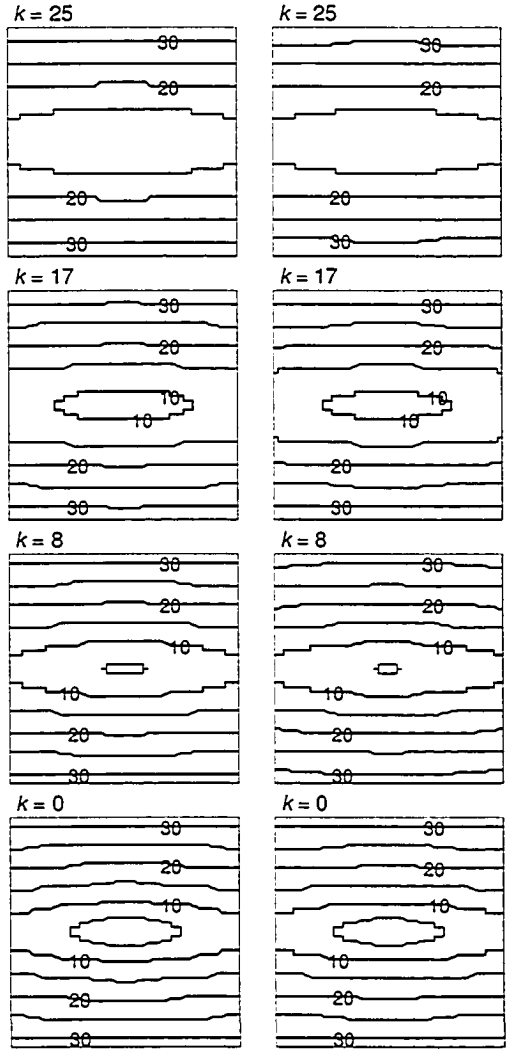

(a) Mono (b) Bi

Figure 5.4: Comparison of wave fronts from the monodomain model using harmonic means with the bidomain model. The applied stimulus is the same in each case. Interstitial conductivity values for the monodomain model were increased by 20%. The setup is the same as described in Figure 5.2.

Chapter 6

Transmural Electrical Heterogeneity as the Basis for Electrocardiographic Waveforms

In this chapter, we investigate the relationship between ECG waveforms and cellular mechanisms from a theoretical standpoint. Electrical propagation in 2-D strips of cardiac tissue will be simulated using the bidomain model derived in Chapter 2 and the numerical methods implemented in Chapter 4, Heterogeneity in AP shape and duration will be introduced into the strip of tissue, and the resultant effect on the ECG will be studied.

6.1 Introduction

Electrocardiogram recordings are used extensively as a tool for diagnosing cardiac electrophysiological disorders. However, the relationship between ECG waveforms and cellular mechanisms—established on a primarily empirical basis—has not been well understood.

Though heterogeneities in the ventricular myocardium had been observed for some time [33, 87, 82], repolarization of the ventricles was thought to be largely homogeneous. Recently, a distinct subpopulation of cells has been identified [71]. Substantial experimental evidence now suggests the existence of three distinct cell types within the ventricular wall: endocardial, midmyocardial (M), and epicardial cells (see [2] for a review). The epicardial and M cells contain a prominent transient outward current (I_{to}), which produces an early repolarization in phase 1 of the AP and gives rise to a notched appearance. In contrast, the endocardial cell contains little or no I_{to} and does not exhibit a notch in phase 1 of its AP.

Further experiments have shown that the transmural ventricular heterogeneity is the basis of electrocardiographic waveforms. In particular, the transmural

dispersion of repolarization (due to the difference in the duration of the AP of the three cell types) inscribes the T wave of the ECG [92], while the transmural gradient resulting from the AP notch produces the J wave [70].

Previous simulation studies have primarily treated the ventricular myocardium as a homogeneous medium. Such uniform models yield a T wave in the ECG that has opposite polarity of the QRS complex, contrary to what is observed. In this chapter, we will introduce heterogeneity in AP shape and duration into a strip of cardiac tissue and investigate the resultant effect on the ECG.

6.2 Methods

We consider a 0.8 cm × 0.8 cm strip of cardiac tissue. To simulate the propagation of electrical activity in this tissue, we used the following mathematical model

$$
\begin{aligned}
C_{\mathrm{m}}\frac{\partial V_{\mathrm{m}}}{\partial t} &= \frac{1}{\chi}\nabla\cdot\boldsymbol{D}_{\mathrm{i}}\nabla V_{\mathrm{m}} + \frac{1}{\chi}\nabla\cdot\boldsymbol{D}_{\mathrm{i}}\nabla\Phi_{\mathrm{e}} - I_{\mathrm{ion}} + I_{\mathrm{app}} \quad x\in H\\
\nabla\cdot(\boldsymbol{D}_{\mathrm{i}}+\boldsymbol{D}_{\mathrm{e}})\nabla\Phi_{\mathrm{e}} + \nabla\cdot\boldsymbol{D}_{\mathrm{i}}\nabla V_{\mathrm{m}} &= 0 \quad x\in H\\
\frac{\partial u}{\partial t} &= w(V_{\mathrm{m}},u)\\
\boldsymbol{n}\cdot\boldsymbol{D}_{\mathrm{i}}(\nabla V_{\mathrm{m}}+\nabla\Phi_{\mathrm{e}}) &= 0 \quad x\in\partial H\\
\boldsymbol{n}\cdot\boldsymbol{D}_{\mathrm{e}}\nabla\Phi_{\mathrm{e}} &= 0 \quad x\in\partial H
\end{aligned}
$$

where for initial conditions all cells were assumed to be at rest. The model was solved numerically by the method of lines presented in Chapter 4.

To describe the AP, we used the Bernus model [7] of human ventricular cells. This model is less computationally demanding than other AP models, yet incorporates nine ionic currents and reproduces important physiological properties. In particular, through variation in expression of the currents I_{K} and I_{to}, the Bernus model provides configurations for endocardial, M, and epicardial APs. For a heterogeneous setup, these three cell types were distributed in the strip of cardiac tissue as illustrated in Figure 6.1. The APD at 90% repolarization was measured by using a threshold potential of −76 mV [7].

The model parameters used are summarized in Table 6.1. The ventricular conductivities were chosen based on the values of Clerc [14]. Action-potential

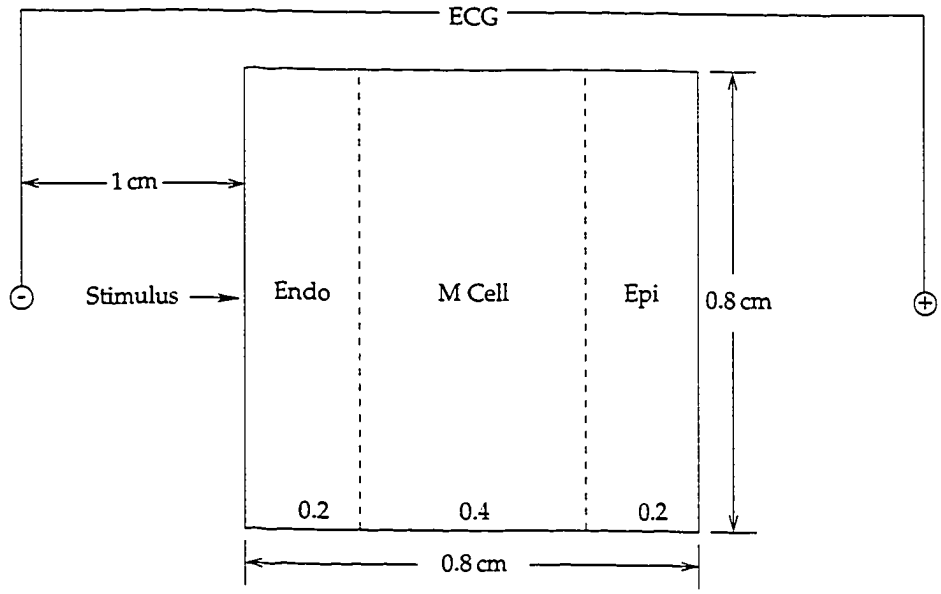

Figure 6.1: Schematic of a 2-D strip of cardiac tissue showing cell distribution and placement of "electrodes" for recording of transmural ECG.

Table 6.1: Simulation parameters for the 0.8 cm × 0.8 cm strip of cardiac tissue.

Membrane capacitance C_m	1.0 μF/cm^2
Surface-to-volume ratio χ	1400.0 cm^{-1}
Spatial step $\Delta x = \Delta y$	0.008 cm
Current stimulus I_{app}	75.0 μA/cm^2
Duration of current stimulus	2.0 ms
Intracellular transverse conductivity g_{it}	0.19 mS/cm
Intracellular longitudinal conductivity g_{il}	1.74 mS/cm
Interstitial transverse conductivity g_{et}	2.36 mS/cm
Interstitial longitudinal conductivity g_{el}	6.25 mS/cm
Extracardiac conductivity g_o	6.25 mS/cm

propagation was initiated by a current stimulus applied to 2×3 points at the center of the endocardial edge.

The extracardiac potential, Φ_o, was determined from the membrane potential, V_m, according to a formula derived in Chapter 2:

$$\Phi_o(r) = \frac{1}{4\pi g_o} \int_H \frac{\nabla' \cdot \boldsymbol{D}_i \nabla' V_m}{\|r - r'\|} dV' \tag{6.1}$$

Unipolar extracardiac potential was thus caculated at "electrodes" located 1 cm from the center of the endocarium and epicardium along the transmural axis, as shown in Figure 6.1. The difference in these two potential tracings constitutes the ECG waveforms presented later. The conductivity of the extracardiac medium, g_o, was set equal to the value of the interstitial conductivity in the longitudinal direction. The precise value of this parameter is not critical. Indeed, it is easily seen from equation (6.1) that this parameter will affect the amplitude of the ECG, but not the overall morphology.

Simulations were performed on an SGI Onyx 300 using version 7.4 of the MIPSpro Fortran compiler. The program was parallelized using OpenMP. Simulation of 500 ms of activity using 5 CPUs took on the order of 30 minutes of wall-clock time.

6.3 Results

Homogeneity and Effects of the Amplitude of I_{to}: Figure 6.2 shows the AP morphology and ECG waveforms for three separate homogeneous cases where all cells are either endocardial, M, or epicardial. This figure reveals the effect on the ECG of the amplitude of the transient outward current, I_{to}. In the Bernus model, the maximum conductance for the transient outward channel, $\bar{G}_{to}$ (which determines the amplitude of I_{to}) is 0.13, 0.35, and 0.4 mS/μF for endocardial, M, and epicardial cells, respectively. The top panel in column (c) of Figure 6.2 shows AP traces for the epicardial case, for which I_{to} produces a distinctive notch in phase 1 of the APs. The corresponding transmural ECG, shown in the lower panel of column (c), exhibits a prominent J wave. In contrast, the endocardial APs (column (a) top

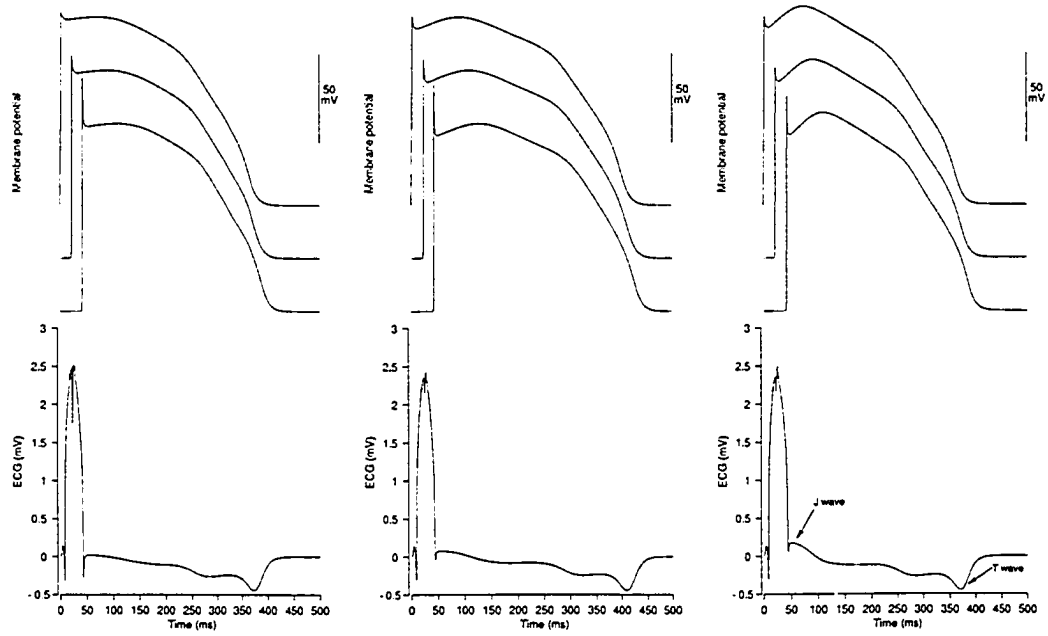

Figure 6.2: Propagated APs and ECG signal for homogeneous cell distribution in a 2-D strip of cardiac tissue with one region of (a) endocardial, (b) M, or (c) epicardial cells. The top panel shows APs from the left edge, middle, and right edge of the strip of tissue. The bottom panel shows the corresponding transmural ECG. The amplitude of I_{to} corresponds with the prominence of the J wave. The contribution of I_{to} is greatest in epicardial cells, and correspondingly, the homogeneous epicardial tissue shows a prominent J wave in the ECG. In contrast, the J wave is barely discernible in the endocardial tissue, where the contribution of I_{to} is minimal. The T wave is inverted in all cases.

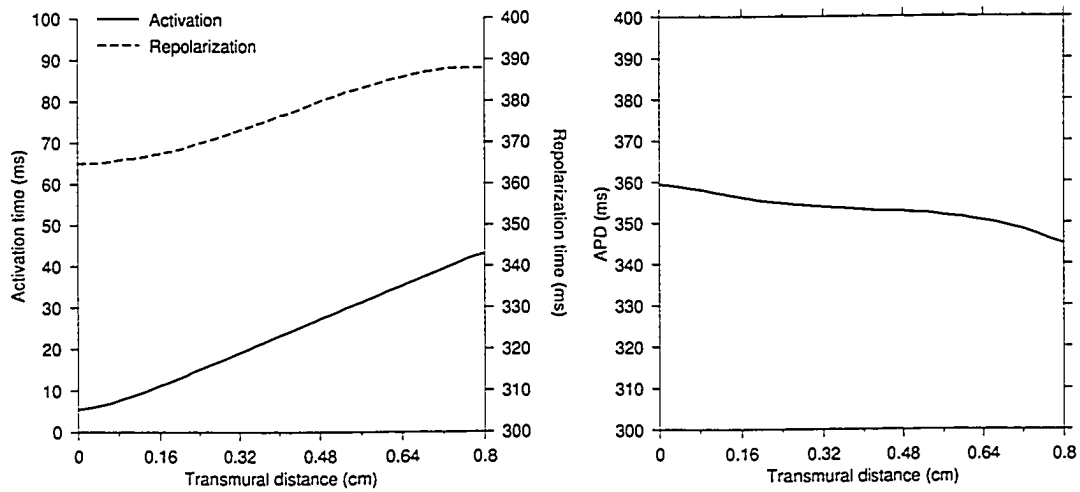

Figure 6.3: Activation time, repolarization time, and APD as a function of transmural distance for a homogeneous strip of epicardial cells. The transmural distance is measured from the "endocardial" edge, so that a distance of 0 cm represents the "endocardium" and 0.8 cm represents the "epicardium".

panel) have no notched appearance, and the J wave of the corresponding ECG is barely discernible.

Figure 6.2 also shows the resultant T wave for these homogeneous cell distributions. In each case the T wave is inverted; that is, it has opposite polarity of the QRS complex. The inverted T wave is the result of the repolarization sequence proceeding in the same direction as the depolarization sequence. Figure 6.3(a) shows the activation and repolarization times as a function of the transmural distance for the homogeneous epicardial case. It is apparent from the figure that the first area to depolarize is also the first area to repolarize. The activation times range from 5.5 ms to 43.0 ms, while the variation in repolarization times is smaller, ranging from 365.0 ms to 388.0 ms. The difference in the gradient of activation and repolarization times is due to the transmural gradient in APD, as shown in Figure 6.3(b). Despite uniform cellular properties across the tissue, the first cell to be activated has the longest APD and the last activated cell has the shortest APD. This heterogeneity is the result of electrotonic interactions and has been observed by other investigators [11, 68, 77].

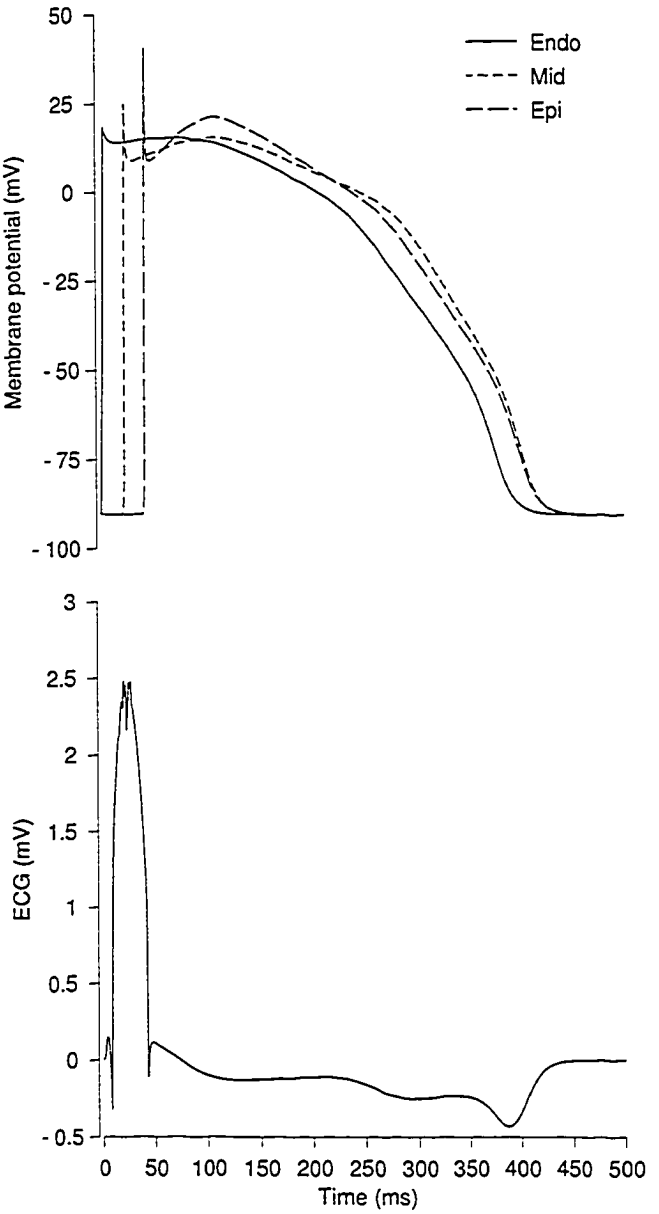

Figure 6.4: AP morphology and ECG waveforms for heterogeneous cell distribution in a 2-D strip of 0.8 cm×0.8 cm cardiac tissue with three regions: one of endocardial cells ($0 \leq x < 0.16$), one of M cells ($0.16 \leq x < 0.64$), and one of epicardial cells ($0.64 \leq x \leq 0.8$). The top panel shows one AP from each of the three regions. The bottom panel shows the corresponding transmural ECG. The APs are as described by the Bernus model with default parameters. Note that the T wave is inverted.

Effects of Heterogeneity: Figure 6.4 shows AP traces and the transmural ECG for a heterogeneous 2-D strip of tissue with default parameters from the Bernus model. The T wave is still inverted. This figure reveals, and agrees with, the important point made by Antzelevitch and colleagues [70, 92]: it is not simply a transmural AP heterogeneity that generates the T wave, but rather the transmural dispersion of repolarization resulting from the opposing voltage gradients on either side of the M region. To elaborate, in our present setup the T wave begins when the endocardial AP separates from that of the other cells. This creates a negative voltage gradient between the endocarial and M regions, and gives rise to the descending limb of the T wave. The voltage gradient increases until the last endocardial cell fully repolarizes, at which time the T wave reaches a peak. As the M cells repolarize, the voltage gradient between the endocardium and M region begin to decrease, and this inscribes the ascending limb of the T wave. Upon full repolarization of the last cell, the T wave is extinguished. There is little opposing voltage gradient on the epicardial side of the M region because, as we see in the AP traces, repolarization of the epicardial and M cells nearly coincides.

To further illustrate how transmural dispersion of repolarization gives rise to the T wave, we performed simulations of heterogeneous tissue with different endocardial AP profiles. Column (a) of Figure 6.5 shows the result of a simulation where $\bar{G}_K$ for the endocardial cells was reduced from 0.019 to 0.015 mS/μF. This change of $\bar{G}_K$ has the effect of lengthening the endocardial AP to the point where the endocardial and epicardial cells repolarize at the same time, but slightly ahead of the M cells. As a result, there is a small negative voltage gradient between the endocardium and M region, which is matched by an equal and *positive* gradient between the *epicardium* and M region. Thus, no T wave is generated. Reducing $\bar{G}_K$ to 0.014 mS/μF lengthens the endocardial AP to the point where repolarization of the endocardium and M region coincides. Hence, there is no voltage gradient between these two regions. On the other hand, the epicardium repolarizes slightly ahead of the M region, creating a positive voltage gradient. The end result is a positive T wave. With a further reduction of $\bar{G}_K$ to 0.011 mS/μF, the endocardium repolarizes last. This produces a positive voltage gradient between the M region and

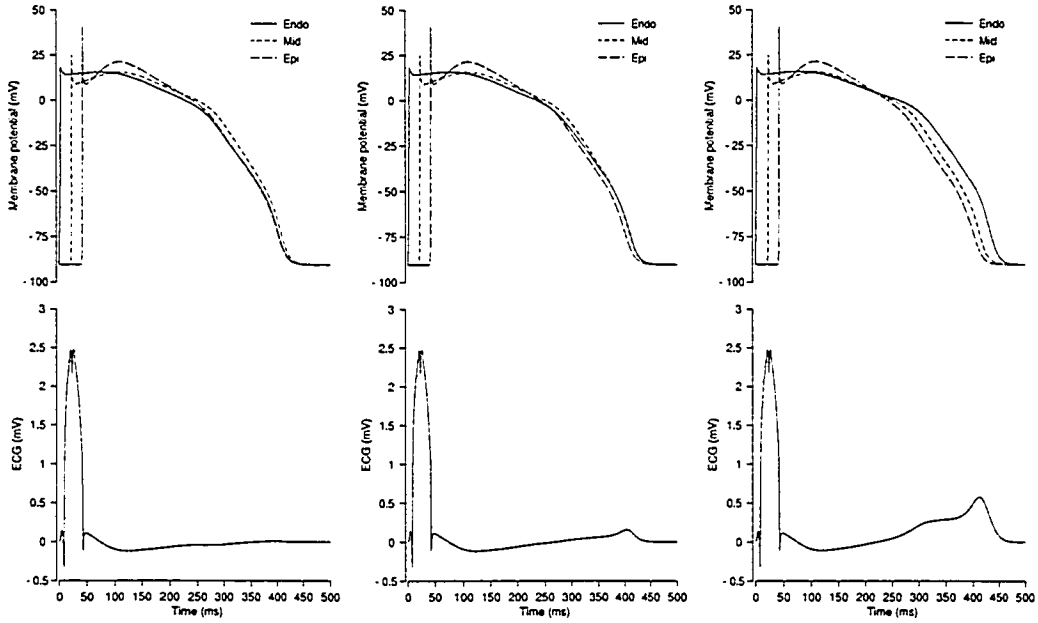

Figure 6.5: Effects on the T wave of modifying the endocardial AP. The same geometry as in Figure 6.4 was used. The top panel shows one AP from each of the three regions. The bottom panel shows the corresponding transmural ECG. The APs are as described by the Bernus model, with the endocardial AP modified by varying $\bar{G}_K$: (a) $\bar{G}_K = 0.015\,mS/\mu F$; (b) $\bar{G}_K = 0.014\,mS/\mu F$; and (c) $\bar{G}_K = 0.011\,mS/\mu F$. In (a), repolarization of the endocardial and epicardial regions are nearly coincident, resulting in a T wave that is barely discernible. In (b), the epicardial region repolarizes ahead of the endocardial region, giving rise to a positive T wave. Increasing this repolarization gradient yields a more prominent T wave as shown in (c).

endocardium, and augments the gradient between the M region and epicardium. Consequently, a large positive T wave is formed.

To test whether a positive T wave is produced under more "realistic" conditions, we modified the Bernus model so that the APDs match those reported by Antzelevitch and colleagues [70, 92]. Note, however, that the Bernus model is a model of the human AP, whereas the work of Antzelevitch has been performed on canine cardiac tissue. Therefore, the matching of the APDs was done in a relative sense. The endocardial AP was chosen as the standard. The M cell AP was then modified so that the ratio of its duration to that of the endocardial AP matched the ratio of the duration of the corresponding APs reported in the work of Antzelecitch

Table 6.2: Comparison of the APDs of the Bernus model and those reported in [70].

		Bernus Model	
	[70]	Original	Modified
Endo APD_{90}	265	357	357
M Cell APD_{90}	280	394	377†
Epi APD_{90}	223	357	299‡
APD_{Endo}/APD_{M}	0.95	0.91	0.95
APD_{Endo}/APD_{Epi}	1.19	1.00	1.19

†$\bar{G}_K = 0.0145\,mS/\mu F$, ‡$\bar{G}_K = 0.030\,mS/\mu F$

and colleagues. The epicardial AP was similarly modified. The modifications and APDs are summarized in Table 6.2.

Figure 6.6 shows the results of a simulation with this modified Bernus model. The epicardium is the last to depolarize and now the first to repolarize, which agrees with that found in [92]. This creates a positive voltage gradient between the epicardium and M region, and inscribes the ascending limb of the T wave. The voltage gradient continues to increase until the last epicardial cell repolarizes, which corresponds with the peak of the T wave. At this point, the negative voltage gradient between the M region and endocardium—arising from the repolarization of endocardial cells ahead of M cells—takes over and thusly inscribes the descending limb of the T wave. The end of the T wave is reached when the voltage gradient is abolished by repolarization of the last M cell.

Effects of Electrotonic Interactions: Figure 6.7 shows the transmural variation in APD for the previous simulation (where the Bernus model was modified to match the APD ratios reported by Antzelevitch and coworkers). The isolated endocardial AP has a duration of 357 ms, whereas in the simulated tissue the endocardial APD is lengthened, varying from 369.5 ms at the endocardial boundary of the tissue to 368.3 ms at the border between the endocardial and M cell regions. The APD of the M cells in the tissue varies from 368.0 ms at the border between the endocardial and M cell regions to 335.0 ms at the border between the epicardial and M cell regions. This represents a decrease in duration compared to the isolated M cell, which has an APD of 377 ms (see Figure 6.8). As with the endocardial cells, the APs

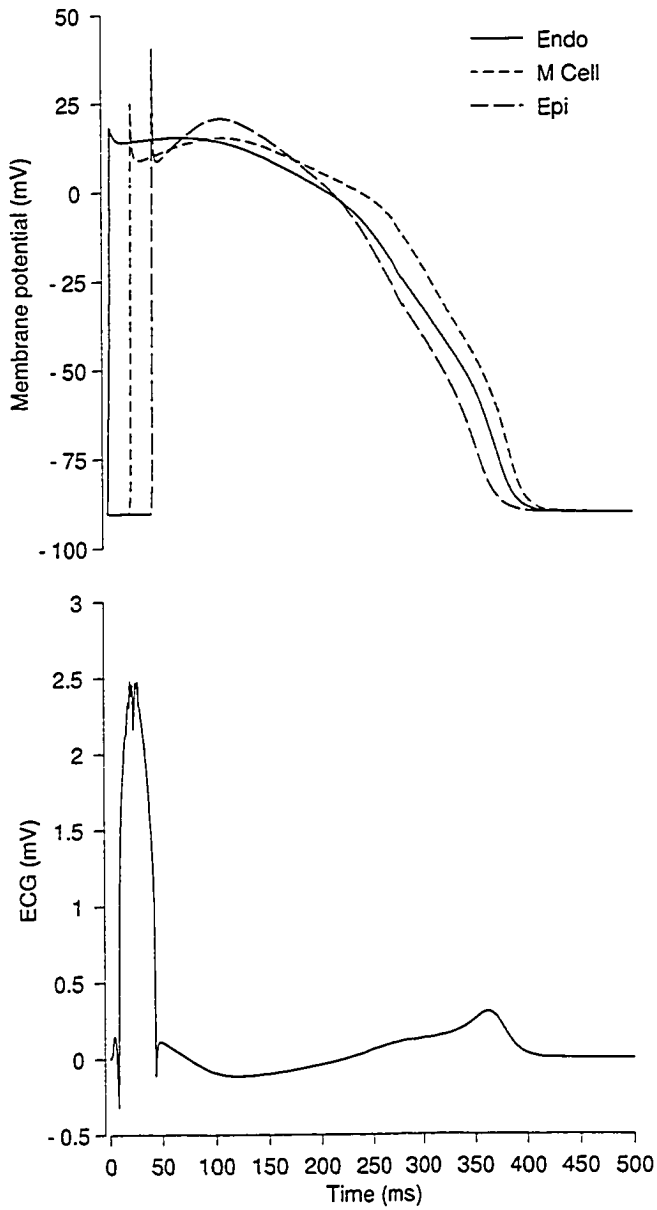

Figure 6.6: AP morphology and ECG waveforms for a heterogeneous cell distribution with a modified Bernus model. The same geometry as in Figure 6.4 was used. The top panel shows one AP from each of the three regions. The bottom panel shows the corresponding transmural ECG. The endocardial AP was described by the Bernus model with default parameters. The epicardial and M cell APs were modified so that the relative APDs match those observed by Antzelevitch and coworkers [70, 92]. Note that the T wave has the expected upright shape.

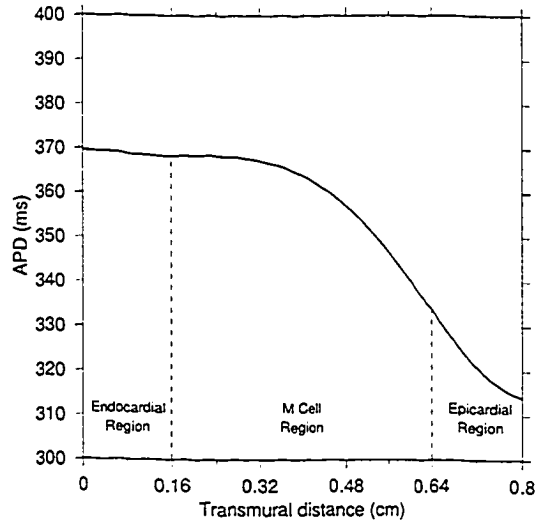

Figure 6.7: Action-potential duration as a function of transmural distance in a heterogeneous 2-D strip of cardiac tissue. The same geometry as in Figure 6.4 was used. The endocardial AP was described by the Bernus model with default parameters. The Bernus epicardial and M cell APs were modified so that the relative APDs match those observed by Antzelevitch and coworkers [70, 92].

of the epicardial cells are lengthed, but the percentage of increase is much greater. The APD of the epicardial cells in the tissue varies from 334.0 ms at the border between the epicardial and M cell regions to 314.0 ms at the epicardial boundary of the tissue. On the other hand, an isolated epicardial cell has an APD of just 299 ms. In short, the electrotonic interactions smooth out the differences in APD across the simulated ventricular wall.

6.4 Discussion

In this chapter, we have investigated the effects of transmural electrophysiological heterogeneities on the waveforms of the ECG. Experimental evidence suggests the existence of three distinct ventricular cells: endocardial, M, and epicardial [2]; however, this is still the subject of controversy [3]. Our results show that a T wave with the same polarity as the QRS complex can be generated by a model of cardiac tissue that includes the three cell types. Of key importance in generating a "correct" T wave was the presence of a transmural dispersion of *repolarization*. On the other

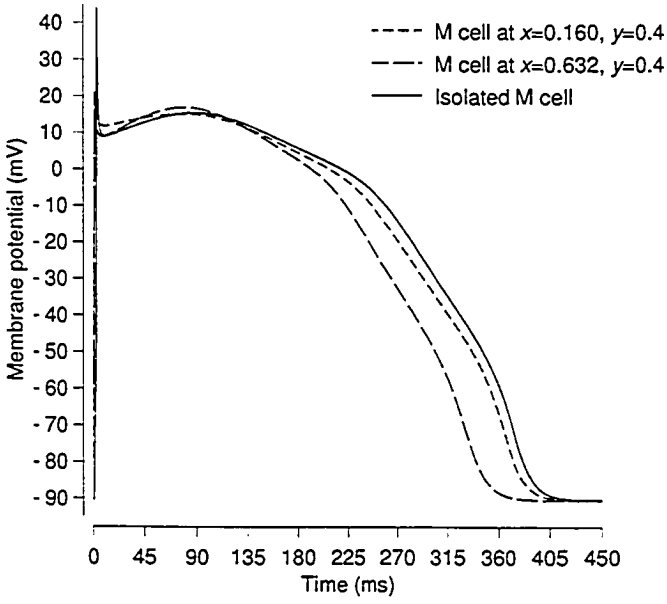

Figure 6.8: Effect of electrotonic interactions on the M cell AP. The figure shows a nonpropagated or 'isolated' M cell AP versus the APs of two M cells from a 2-D strip of heterogeneous cardiac tissue.

hand, a J wave was produced by the heterogeneous distribution of the transient outward current, I_{to}, across the ventricular wall. The presence of a large I_{to} in epicardium created a notch in the AP that was not present in the endocardial AP. This established a transmural voltage gradient that manifested as a J wave in the ECG.

The effect of heterogeneity has only recently been investigated in simulation studies. Gima and Rudy [30] recently investigated the basis of ECG waveforms in a heterogeneous model incorporating M cells. Their simulations included the more detail LRd model of cardiac APs [25, 44, 86, 94]; however, their studies were restricted to a 1-D monodomain fiber. Quite recently, Clayton and Holden [11] studied the propagation of normal beats and re-entry in 2-D and 3-D models of cardiac tissue. Their monodomain model incorporated regional differences in AP shape and duration. For description of the AP, they used the LRd model as a starting point and then simplified it so that all ionic concentrations, except for the intracellular $[Ca^{2+}]$, were held constant.

Estimation of pseudo ECGs from propagation models is often done with the

following formula [11, 30]:

$$\Phi_o(r) = \frac{1}{4\pi g_o} \int_H -D_i \nabla' V_m \cdot \nabla' \|r - r'\|^{-1} dV' \tag{6.2}$$

On the other hand, we have used the expression

$$\Phi_o(r) = \frac{1}{4\pi g_o} \int_H \frac{\nabla' \cdot D_i \nabla' V_m}{\|r - r'\|} dV' \tag{6.1}$$

To see how these two equations relate, we begin with the vector identity

$$\nabla \cdot \left(\|r - r'\|^{-1} D_i \nabla V_m \right) = \|r - r'\|^{-1} \nabla \cdot D_i \nabla V_m + D_i \nabla V_m \cdot \nabla \|r - r'\|^{-1}$$

Using this expression in equation (6.1) we get

$$\Phi_o(r) = \frac{1}{4\pi g_o} \left\{ \int_H \nabla' \cdot \left(\|r - r'\|^{-1} D_i \nabla' V_m \right) dV' - \int_H D_i \nabla' V_m \cdot \nabla' \|r - r'\|^{-1} dV' \right\}$$

and applying the divergence theorem [80] to the first integral gives

$$\begin{aligned} \Phi_o(r) &= \frac{1}{4\pi g_o} \left\{ \int_{\partial H} n \cdot \left(\|r - r'\|^{-1} D_i \nabla' V_m \right) dS' - \int_H D_i \nabla' V_m \cdot \nabla' \|r - r'\|^{-1} dV' \right\} \\ &= \frac{1}{4\pi g_o} \left\{ \int_{\partial H} \|r - r'\|^{-1} \left(n \cdot D_i \nabla' V_m \right) dS' - \int_H D_i \nabla' V_m \cdot \nabla' \|r - r'\|^{-1} dV' \right\} \end{aligned}$$

Under the assumption of the Colli Franzone boundary condition (see Section 2.4), we have $n \cdot D_i \nabla V_m = 0$ and so the first integral drops out. In this case, equation (6.1) reduces to equation (6.2). We, however, have used the boundary conditions proposed by Tung (again refer to Section 2.4), for which $n \cdot D_i(\nabla V_m + \nabla \Phi_e) = 0$. In this situation, equations (6.1) and (6.2) are not equivalent.

Our calculated ECGs differ from the "standard" ECG for several reasons. First, we did not have an atrial component in our model; therefore, there was no P wave in our simulated ECGs. Second, we initiated propagation by applying a stimulus to just one site. This does not mimick how the Purkinje network activates the ventricular muscle, and hence can not reproduce the true QRS complex. Finally, the ECG was caculated from V_m, which was recorded in the propagation model at 1 ms intervals. This interval can easily miss the true peaks in the APs. Shortening the interval at which V_m is recorded in the propagation model should likely produce a 'smoother' QRS complex, but this was not investigated.

The model used in this study has a number of limitations. We have restricted investigations to a simple 2-D geometry, and have assumed uniform tissue conductivity across the wall. Some experimental evidence [93] has shown a conductive barrier between epicardium and deep subepicardium, which coincided with a sharp transition in cell orientation in this region. Furthermore, Zygmunt and coworkers [96, 97] have shown that I_{Na} and I_{NaCa} contribute to electrical heterogeneity within the canine ventricle. We, however, have investigated a heterogeneous expression of only I_K and I_{to}. Lastly, we have not included a Purkinje network and ignore the mechanical activity of cardiac tissue. Nonetheless, these simulations provide, on a theoretical basis, links between the morphologies of ECG waveforms and the underlying cellular mechanisms.

Chapter 7

Conclusions

We have investigated the propagation of electrical activity in the human ventricular myocardium. In Chapter 2, we presented the derivation of a mathematical model that includes detailed cellular membrane electrodynamics and can incorporate important characteristics of cardiac tissue, such as anisotropy, fiber rotation, and transmural heterogeneity in electrophysiological properties. We have implemented two numerical methods:

- an ADI method (Chapter 3) that can only handle a monodomain model with restricted boundary conditions, yet is computationally efficient; and
- a method-of-lines approach (Chapter 4) that can handle the bidomain model in its fully coupled form, but requires huge computing resources.

In Chapter 5, we described a decoupling procedure which requires no assumptions on the anisotropic conductivities and which yields a single reaction-diffusion equation (or monodomain model) for simulating the propagation of activation. Preliminary results suggest that the decoupled model may be adequate for studying general properties of cardiac dynamics in isolated whole heart models. In Chapter 6, we investigated the basis for ECG waveforms using a model that had transmural electrical heterogeneity through incorporation of three cell types: endocardial, M cell, and epicardial. The simulations demonstrated that a T wave with the same polarity as the QRS complex was generated by a transmural dispersion of repolarization (resulting from the heterogeneous distribution of cell types), while a J wave was produced by a transmural voltage gradient (resulting from the heterogeneous distribution of the transient outward current, I_{to}).

The numerical solution of the bidomain equations typically proceeds by solving each subsystem — membrane potential, interstitial potential, and AP variables —

separately through some form of equation splitting. Unless care is taken, this limits the accuracy of the solution. A key accomplishment of this thesis was the development and implementation of a method-of-lines approach for solving the anisotropic bidomain model in its fully coupled form. This approach resulted in a system of DAEs, which was solved with the well written and robust software package DASPK. However, for 3-D models the system of DAEs was quite large. Without further intervention, the memory requirements and CPU time would have been prohibitive. This problem was overcome in two ways. First, the memory requirement was reduced by taking advantage of the sparsity of the DAE system, and second, computing time was reduced through parallelization of the code.

Limitations and Future Work

The preliminary results presented in Chapter 6 on the basis of ECG waveforms were restricted to 2-D sheets as the turn-around time for 3-D simulations prevented the tuning of parameters. Further investigation should be done in a 3-D wedge with realistic fiber rotation. The model already includes all of the necessary prerequisites to do these simulations.

The linear systems arising from the method-of-lines approach were solved by a direct method using a sparse solver. For large-scale DAE systems, a preconditioned Krylov subspace method for the linear-system solution may be a better choice. The Krylov method can potentially outperform the direct method in terms of time steps, error-test failures, and so on, thereby greatly reducing the computing time while requiring less memory. However, the selection of a good preconditioner largely influences the success of this method. DASPK provides the preconditioned Krylov method has an option, and this avenue was initially investigated, but later abandoned due to lack of a good preconditioner. Further research in this area could yield better results.

In the method-of-lines approach, we performed the spatial discretization using finite differences and assuming a fixed mesh. At present, the code is restricted to regular geometries. The discretization component could be replaced by collocation methods or finite elements, allowing easy application to irregular geometries such

as a realistic heart shape. Another avenue of research would be to drop the fixed-mesh constraint, thereby making the code adaptive in both time and space.

Future work should also include an analysis of the new "capillary capacitance" bidomain model with a view of showing that this model can reproduce the same time course of the cardiac AP foot (τ_{foot}), which has been observed in experimental analysis.

Appendix A

Glossary of Physiological Terms

Membrane	semipermeable structure at surface of living cells, such as neurons and cardiac cells
Cytoplasm, myoplasm, axoplasm	the semifluid conducting medium inside a living cell in general, and a cardiac cell and an axon in particular
Axon	extension of a neuron, carrying nerve impulses
Resting Potential	electrical potential of the interior of a cell or axon at rest relative to the exterior
Polarization	de- and hyper-, result of current flow by which the membrane potential is made less and more negative
Local circuit currents	electric currents through the axon or cardiac tissue and surrounding solution by which an impulse at one region stimulates an adjacent region, resulting in propagated activation
Cable theory	as applied to a linear axon or cardiac fibre expresses local circuit current in terms of λ
Space clamp	an experimental technique in which the membrane potential and current are kept uniform over a short length of axon/fibre; can be used for either current- or voltage-clamp experiments

Activation	fast process by which a membrane goes from a passive to an active state; the initial stage of impulse production, just following a suprathreshold stimulus
Strength-duration curve	a curve showing the threshold amplitude of a rectangular stimulating pulse plotted against its duration
Action potential	time course of a potential during activation and recovery phases of nerve or cardiac cell
Propagation	conduction process by which activity at one point creates local circuit current to excite adjacent region
Current clamp	an experimental technique in which the membrane current is controlled and the time course of the membrane potential recorded
Voltage clamp	an experimental technique in which the membrane potential is controlled by electronic feedback and the time course of the membrane current recorded
Absolute refractory period	the period following an impulse during which the axon or cardiac cell is inexcitable
Accommodation	the decrease of excitability during a subthreshold constant stimulus
Active response	a response due to the nonlinear properties of the membrane; the opposite of passive response
Conduction	the movement of activation; propagated activation

Decremental conduction	impulse conduction with ever-decreasing action-potential size, eventually leading either to an impulse of constant size or to extinction of the impulse
Depressed state	a state following a subthreshold stimulus in which the threshold is greater than the resting value
Enhanced state	a state following a subthreshold stimulus in which the threshold is lower than the resting value
Impulse	a sequence of electrical and chemical events in an excitable cell, consisting of activation and recovery
Latency	the time between the beginning of a suprathreshold stimulus and the appearance of the resulting impulse
Local response	a response that occurs and remains only near the stimulating electrode
Membrane action potential	an action potential recorded from a space-clamped cell or a small, uniformly responding patch of cell membrane
Nondecremental conduction	impulse conduction with constant velocity and action-potential size
Passive response	a response that has an amplitude proportional to the amplitude of the stimulus; a linear response

Refractory state	the state following activation during which the excitable cell is first rendered inexcitable (absolute refractory period) and then has a threshold above the resting value (relatively refractory period)
Relative refractory period	the period following activation during which the threshold is greater than the resting value
Response	an electrochemical change, either an action potential or a subthreshold active response, resulting from applying a stimulus to an excitable cell
Resting state	the stationary condition of an excitable cell which has received no stimuli recently
Stationary action potential	an action potential that occurs locally in an axon or fibre and is not propagated
Stimulus	any physical agent acting on an excitable cell that can serve to produce an action potential
Stimulus-response curve	a curve of response size versus stimulus intensity
Subthreshold stimulus	a stimulus too small to elicit an action potential
Suprathreshold stimulus	a stimulus large enough to produce an action potential
Threshold	the value of stimulus just large enough to produce an action potential
Uniform conduction	nondecremental conduction

Appendix B

Bernus AP Model

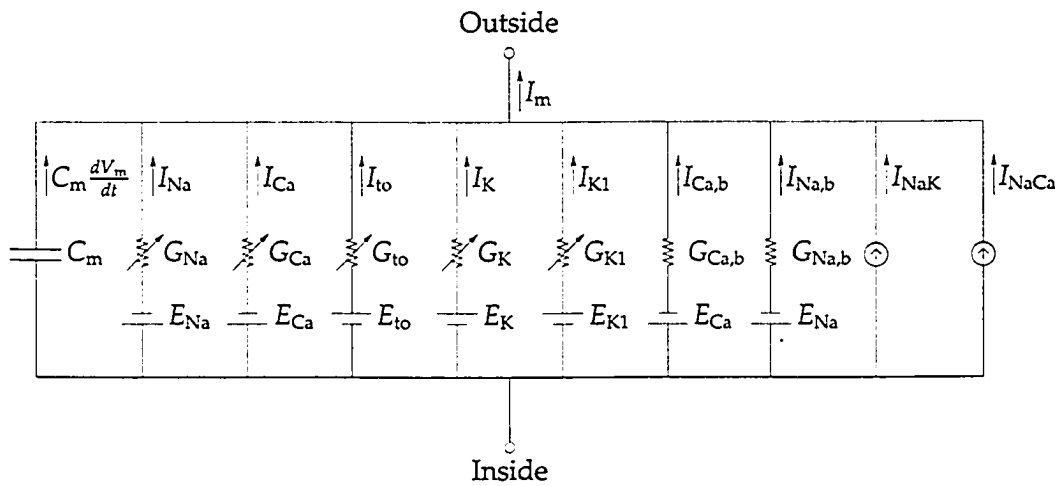

Figure B.1: Electrical circuit model of the Bernus cell membrane.

Inward Currents

Fast Na^+ Current

$$I_{Na} = \bar{G}_{Na} \cdot m^3 \cdot v^2 \cdot (V_m - E_{Na}) \tag{B.1}$$

$$\alpha_m = \frac{0.32 \cdot (V_m + 47.13)}{1 - \exp[-0.1 \cdot (V_m + 47.13)]} \tag{B.2}$$

$$\beta_m = 0.08 \cdot \exp(-V_m/11) \tag{B.3}$$

$$v_\infty = 0.5 \cdot [1 - \tanh(7.74 + 0.12 \cdot V_m) \tag{B.4}$$

$$\tau_v = 0.25 + 2.24 \cdot \left(\frac{1 - \tanh(7.74 + 0.12 \cdot V_m)}{1 - \tanh[0.07 \cdot (V_m + 92.4)]} \right) \tag{B.5}$$

Slow Ca^{2+} Current

$$I_{Ca} = \bar{G}_{Ca} \cdot d_\infty \cdot f \cdot f_{Ca} \cdot (V_m - E_{Ca}) \tag{B.6}$$

$$d_\infty = \frac{\alpha_d}{\alpha_d + \beta_d} \tag{B.7}$$

$$\alpha_d = \frac{14.98 \cdot \exp\{-0.5 \cdot [(V_m - 22.36)/16.68]^2\}}{16.68 \cdot \sqrt{2\pi}} \tag{B.8}$$

$$\beta_d = 0.1471 - \frac{5.3 \cdot \exp\{-0.5 \cdot [(V_m - 6.27)/14.93]^2\}}{14.93 \cdot \sqrt{2\pi}} \tag{B.9}$$

$$\alpha_f = \frac{6.87 \cdot 10^{-3}}{1 + \exp[-(6.1546 - V_m)/6.12]} \tag{B.10}$$

$$\beta_f = \frac{0.069 \cdot \exp[-0.11 \cdot (V_m + 9.825)] + 0.011}{1 + \exp[-0.278 \cdot (V_m + 9.825)]} + 5.75 \cdot 10^{-4} \tag{B.11}$$

$$f_{Ca} = \frac{1}{1 + [Ca^{2+}]_i/0.0006} \tag{B.12}$$

Outward Currents

Transient Outward Current

$$I_{to} = \bar{G}_{to} \cdot r_\infty \cdot to \cdot (V_m - E_{to}) \tag{B.13}$$

$$r_\infty = \frac{\alpha_r}{\alpha_r + \beta_r} \tag{B.14}$$

$$\alpha_r = \frac{0.5266 \cdot \exp[-0.0166 \cdot (V_m - 42.2912)]}{1 + \exp[-0.0943 \cdot (V_m - 42.2912)]} \tag{B.15}$$

$$\beta_r = \frac{5.186 \cdot 10^{-5} \cdot V_m + 0.5149 \cdot \exp[-0.1344 \cdot (V_m - 5.0027)]}{1 + \exp[-0.1348 \cdot (V_m - 5.186 \cdot 10^{-5}]} \tag{B.16}$$

$$\alpha_{to} = \frac{5.612 \cdot 10^{-5} \cdot V_m + 0.0721 \cdot \exp[-0.173 \cdot (V_m + 34.2531)]}{1 + \exp[-0.1732 \cdot (V_m + 34.2531)]} \tag{B.17}$$

$$\beta_{to} = \frac{1.215 \cdot 10^{-4} \cdot V_m + 0.0767 \cdot \exp[-1.66 \cdot 10^{-9} \cdot (V_m + 34.0235)]}{1 + \exp[-0.1604 \cdot (V_m + 34.0235)]} \tag{B.18}$$

$$\tau_{to} = \frac{1}{p\alpha_{to} + p\beta_{to}} \tag{B.19}$$

$$to_\infty = \frac{\alpha_{to}(V_m - V_{shift})}{\alpha_{to}(V_m - V_{shift}) + \beta_{to}(V_m - V_{shift})} \tag{B.20}$$

Delayed Rectifier K^+ Current

For endocardial and epicardial cells

$$X_\infty = \frac{0.988}{1 + \exp(-0.861 - 0.0620 \cdot V_m)} \tag{B.21}$$

$$\tau_X = 240 \cdot \exp[-(25.5 + V_m)^2/156] + 182 \cdot [1 + \tanh(0.154 + 0.0116 \cdot V_m)] + \tau'_X \tag{B.22}$$

$$\tau'_X = 40 \cdot [1 - \tanh(160 + 2 \cdot V_m)] \tag{B.23}$$

For M cells

$$X_\infty = \frac{0.972}{1 + \exp(-2.036 - 0.0834 \cdot Vm)} \tag{B.24}$$

$$\tau_X = 380 \cdot \exp[-(25.5 + V_m)^2/156] + 166 \cdot [1 + \tanh(0.558 + 0.0169 \cdot V_m)] \tag{B.25}$$

Inward Rectifier K^+ Current

$$I_{K1} = \bar{G}_{K1} \cdot K1_\infty \cdot (V_m - E_K) \tag{B.26}$$

$$K1_\infty = \frac{\alpha_{K1}}{\alpha_{K1} + \beta_{K1}} \tag{B.27}$$

$$\alpha_{K1} = \frac{0.1}{1 + \exp[0.06 \cdot (V_m - E_K - 200)]} \tag{B.28}$$

$$\beta_{K1} = \frac{3 \cdot \exp[2 \cdot 10^{-4} \cdot (V_m - E_K + 100)] + \exp[0.1 \cdot (V_m - E_K - 10)]}{1 + \exp[-0.5 \cdot (V_m - E_K)]} \tag{B.29}$$

Background Currents

Ca^{2+} Background Current

$$I_{Ca,b} = \bar{G}_{Ca,b} \cdot (V_m - E_{Ca}) \tag{B.30}$$

Na^+ Background Current

$$I_{Na,b} = \bar{G}_{Na,b} \cdot (V_m - E_{Na}) \tag{B.31}$$

Pump and Exchanger Currents

Na^+-K^+ Pump

$$I_{NaK} = \bar{G}_{NaK} \cdot f_{NaK} \cdot f'_{NaK} \tag{B.32}$$

$$f_{NaK} = \frac{1}{1 + 0.1245 \cdot \exp(-0.0037 \cdot V_m) + 0.0365 \cdot \sigma \cdot \exp(-0.037 \cdot V_m)} \tag{B.33}$$

$$f'_{NaK} = \frac{1}{1 + (10/[Na^+]_i)^{1.5}} \cdot \frac{[K^+]_o}{[K^+]_o + 1.5} \tag{B.34}$$

$$\sigma = 0.1428 \cdot [\exp([Na^+]_o/67.3) - 1] \tag{B.35}$$

Na^+/Ca^{2+} Exchanger

$$I_{NaCa} = \bar{G}_{NaCa} \cdot f_{NaCa} \tag{B.36}$$

$$\begin{aligned} f_{NaCa} = {} & (87.5^3 + [Na^+]_o^3)^{-1} \cdot (1.38 + [Ca^{2+}]_o)^{-1} \\ & \cdot \{1 + 0.1 \cdot \exp(-0.024 \cdot V_m)\}^{-1} \\ & \cdot \{[Na^+]_i^3 \cdot [Ca^{2+}]_o \cdot \exp(0.013 \cdot V_m) \\ & - [Na^+]_o^3 \cdot [Ca^{2+}]_i \cdot \exp(-0.024 \cdot V_m)\} \end{aligned} \tag{B.37}$$

Bibliography

[1] R. C. Aiken, editor. *Stiff computation*. Oxford University Press, Oxford, UK, 1985.

[2] C. Antzelevitch and J. Fish. Electrical heterogeneity within the ventricular wall. *Basic Res. Cardiol.*, 96:517–527, 2001.

[3] E. P. Anyukhovsky, E. A. Sosunov, R. Z. Gainullin, and M. R. Rosen. The controversial M cell. *J. Cardiovasc. Electrophysiol.*, 10:244–260, 1999.

[4] U. M. Ascher and L. R. Petzold. *Computer Methods for Ordinary Differential Equations and Differential-Algebraic Equations*. SIAM, Philadelphia, PA, USA, 1998.

[5] T. Ashihara, T. Namba, T. Ikeda, M. Ito, M. Kinoshita, and K. Nakazawa. Breakthrough waves during ventricular fibrillation depend on the degree of rotational anisotropy and the boundary conditions: A simulation study. *J. Cardiovasc. Electrophysiol.*, 12:312–322, 2001.

[6] G. W. Beeler and H. Reuter. Reconstruction of the action potential of ventricular myocardial fibres. *J. Physiol. (Lond.)*, 268:177–210, 1977.

[7] O. Bernus, R. Wilders, C. W. Zemlin, H. Verschelde, and A. V. Panfilov. A computationally efficient electrophysiological model of human ventricular cells. *Am. J. Physiol. Heart. Circ. Physiol.*, 282:H2296–H2308, 2002.

[8] K. E. Brenan, S. L. Campbell, and L. R. Petzold. *Numerical Solution of Initial-Value Problems in Differential-Algebraic Equations*. SIAM, Philadelphia, PA, USA, 1996. Revised and corrected reprint of the 1989 original.

[9] P. L. T. Brian. A finite difference method of high-order accuracy for the solution of three-dimensional transient heat conduction problems. *AIChE J.*, 1:367–370, 1961.

[10] P. N. Brown, A. C. Hindmarsh, and L. R. Petzold. Using Krylov methods in the solution of large-scale differential-algebraic systems. *SIAM J. Sci. Comput.*, 15(6):1467–1488, 1994.

[11] R. H. Clayton and A. V. Holden. Propagation of normal beats and re-entry in a computational model of ventricular cardiac tissue with regional differences in action potential shape and duration. *Prog. Biophys. Mol. Biol.*, 85:473–499, 2004.

[12] C. J. Clements. Nonlinear wave propagation in an anisotropic medium. Master's thesis, Department of Mathematics, Statistics, and Computing Science, Dalhousie University, Halifax, Nova Scotia, Canada, 1996.

[13] C. J. Clements, J. C. Clements, and B. M. Horáček. On the formation of scroll waves in an anisotropic ventricular myocardium. In S. Ruan, G. S. K. Wolkowicz, and J. Wu, editors, *Differential Equations with Applications to Biology*, pages 97–107, Providence, RI, 1999. American Mathematical Society. Proceedings of the International Conference held at Dalhousie University, Halifax, NS, July 25–29, 1997.

[14] L. Clerc. Directional differences of impulse spread in trabecular muscle from mammalian heart. *J. Physiol. (Lond.)*, 255:335–346, 1976.

[15] K. W. Cole. *Membranes, Ions, and Impulses.* University of California Press, Berkeley, 1968.

[16] P. Colli Franzone, L. Guerri, and S. Rovida. Wavefront propagation in an activation model of the anisotropic cardiac tissue: asymptotic analysis and numerical simulations. *J. Math. Biol.*, 28:121–176, 1990.

[17] P. Colli Franzone and L. Guerri. Spreading of excitation in 3-D models of the anisotropic cardiac tissue. I. Validation of the eikonal model. *Math. Biosci.*, 113: 145–209, 1993.

[18] P. Colli Franzone, L. Guerri, and S. Tentoni. Mathematical modeling of the excitation process in myocardial tissue: Influence of fiber rotation on wavefront propagation and potential field. *Math. Biosci.*, 101:155–235, 1990.

[19] M. Courtemanche and A. T. Winfree. Re-entrant rotating waves in a Beeler-Reuter based model of two-dimensional cardiac electrical activity. *Int. J. Bifur. Chaos*, 1:431–444, 1991.

[20] J. M. Davidenko, P. F. Kent, D. R. Chialvo, D. C. Michaels, and J. Jalife. Sustained vortex-like waves of excitation in normal isolated ventricular muscle. *Proc. Natl. Acad. Sci. USA*, 87:8785–8789, 1990.

[21] J. M. Davidenko, A. M. Pertsov, R. Salomonsz, W. P. Baxter, and J. Jalife. Spatiotemporal irregularities of spiral wave activity in isolated ventricular muscle. *J. Electrocardiol.*, 24 (Suppl.):113–122, 1992.

[22] J. M. Davidenko, A. V. Pertsov, R. Salomonsz, W. Baxter, and J. Jalife. Stationary and drifting spiral waves of excitation in isolated cardiac muscle. *Nature*, 355: 349–351, 1992.

[23] G. Di Cola, E. Macchi, and S. Sanfelici. Numerical simulation of activation in a bidomain model of cardiac muscle. *Med. Biol. Eng. Comput.*, 34 (Suppl. 1): 87–88, 1996.

[24] J. Douglas, Jr. Alternating direction methods for three space variables. *Numer. Math.*, 4:41–63, 1962.

[25] G. M. Faber and Y. Rudy. Action potential and contractility changes in $[Na^+]_i$ overloaded cardiac myocytes: A simulation study. *Biophys. J.*, 78(5):2392–2404, May 2000.

[26] R. FitzHugh. Impulses and physiological states in theoretical models of nerve membrane. *Biophys. J.*, 1:445–466, 1961.

[27] D. W. Frazier, P. D. Wolf, J. M. Wharton, A. S. L. Tabg, W. M. Smith, and R. E. Ideker. Stimulus-induced critical point: Mechanism for the electrical initiation of reentry in normal canine myocardium. *J. Clin. Invest.*, 83:1039–1052, 1989.

[28] C. W. Gear. Simultaneous numerical solution of differential-algebraic equations. *IEEE Trans. Circuit Theory*, CT-18:89–95, 1971.

[29] D. B. Geselowitz and W. T. Miller III. A bidomain model for anisotropic cardiac muscle. *Ann. Biomed. Eng.*, 11:191–206, 1983.

[30] K. Gima and Y. Rudy. Ionic current basis of electrocardiographic waveforms: A model study. *Circ. Res.*, 90:889–896, 2002.

[31] L. S. Green, B. Taccardi, P. R. Ershler, and R. L. Lux. Epicardial potential mapping: Effects of conducting media on isopotential and isochrone distributions. *Circulation*, 84:2513–2521, 1991.

[32] R. M. Gulrajani. *Bioelectricity and Biomagnetism*. John Wiley & Sons, New York, 1998.

[33] J. Han and G. K. Moe. Nonuniform recovery of excitability in ventricular muscle. *Circ. Res.*, 14:44–60, 1964.

[34] C. S. Henriquez, A. L. Muzikant, and C. K. Smoak. Anisotropy, fiber curvature, and bath loading effects on activation in thin and thick cardiac tissue preparations: Simulations in a three-dimensional bidomain model. *J. Cardiovasc. Electrophysiol.*, 7:424–444, 1996.

[35] A. L. Hodgkin and A. F. Huxley. A quantitative description of membrane current and its application to conduction and excitation in nerve. *J. Physiol. (Lond.)*, 117:500–544, 1952.

[36] A. L. Hodgkin and W. A. Rushton. The electrical constants of crustacean nerve fiber. *Proc. R. Soc. Biol. Sci.*, 133:444, 1946.

[37] B. M. Horáček, J. Nenonen, J. A. Edens, and L. J. Leon. A hybrid model of propagated excitation in the ventricular myocardium. In D. N. Ghista, editor, *Biomedical and Life Physics*, pages 181–190. Vieweg Verlag, Wiesbaden, 1996.

[38] J. J. B. Jack, D. Noble, and R. W. Tsien. *Electric Current Flow in Excitable Cells*. Clarendon Press, Oxford, second edition, 1983.

[39] J. P. Keener. An eikonal-curvature equation for action potential propagation in myocardium. *J. Math. Biol.*, 29:629–651, 1991.

[40] J. P. Keener and A. V. Panfilov. Three-dimensional propagation in the heart: The effects of geometry and fibre orientation on propagation in myocardium. In Zipes and Jalife [95], chapter 32, pages 335–347.

[41] W. Krassowska and J. C. Neu. Effective boundary conditions for syncytial tissues. *IEEE Trans. Biomed. Eng.*, 41:143–150, 1994.

[42] V. I. Krinsky. Mathematical models of cardiac arrhythmias (spiral waves). *Pharmacol. Ther. [B]*, 3:539–555, 1978.

[43] C. Luo and Y. Rudy. A model of the ventricular cardiac action potential: Depolarization, repolarization, and their interaction. *Circ. Res.*, 68:1501–1526, 1991.

[44] C. Luo and Y. Rudy. A dynamic model of the cardiac ventricular action potential: I. Simulation of ionic currents and concentration changes. *Circ. Res.*, 74:1071–1096, 1994.

[45] D. K. Melgaard and R. F. Sincovec. General software for two-dimensional nonlinear partial differential equations. *ACM Trans. Math. Software*, 7:106–125, 1981.

[46] A. L. Muzikant and C. S. Henriquez. Paced activation mapping reveals organization of myocardial fibers: A simulation study. *J. Cardiovasc. Electrophysiol.*, 8:281–294, 1997.

[47] J. Nagumo, S. Arimoto, and S. Yoshizawa. An active pulse transmission line simulating nerve axon. *Proc. IRE*, 50:2061–2070, 1962.

[48] D. Noble. The surprising heart: a review of recent progress in cardiac electrophysiology. *J. Physiol. (Lond.)*, 353:1–50, 1984.

[49] A. V. Panfilov and A. V. Holden. Spatiotemporal irregularity in a two-dimensional model of cardiac tissue. *Int. J. Bifur. Chaos*, 1:219–225, 1991.

[50] A. M. Pertsov, E. A. Emarkova, and A. V. Panfilov. Rotating spiral waves in modified FitzHugh-Nagumo model. *Physica D*, 14:117–124, 1984.

[51] A. M. Pertsov, J. M. Davidenko, R. Salomonsz, W. T. Baxter, and J. Jalife. Spiral waves of excitation underlie reentrant activity in isolated cardiac muscle. *Circ. Res.*, 72:631–650, 1993.

[52] A. M. Pertsov and J. Jalife. Three-dimensional vortex-like reentry. In Zipes and Jalife [95], chapter 38, pages 403–410.

[53] A. Peskoff. Electric potential in three-dimensional electrically syncytial tissues. *Bull. Math. Biol.*, 41:163–181, 1979.

[54] L. Petzold. Differential/algebraic equations are not ODEs. *SIAM J. Sci. Statist. Comput.*, 3:367–384, 1982.

[55] L. R. Petzold. A description of DASSL: a differential/algebraic system solver. In R. S. Stepleman, editor, *Scientific Computing*, IMACS Transactions on Scientific Computation, I, pages 65–68. International Association for Mathematics and Computers in Simulation (IMACS), New Brunswick, NJ, 1983.

[56] R. Plonsey. Bioelectric sources arising in excitable fibers. *Ann. Biomed. Eng.*, 16:519–546, 1988.

[57] R. Plonsey and R. C. Barr. Mathematical modeling of electrical activity of the heart. *J. Electrocardiol.*, 20:219–226, 1987.

[58] R. Plonsey and R. C. Barr. *Bioelectricity: A Quantitative Approach*. Plenum Press, New York, 1988.

[59] L. Priebe and D. J. Beuckelmann. Simulation study of cellular electric properties. *Circ. Res.*, 82:1206–1223, 1998.

[60] Z. Qu, J. Kil, F. Xie, A. Garfinkel, and J. N. Weiss. Scroll wave dynamics in a three-dimensional cardiac tissue model: Roles of restitution, thickness, and fiber rotation. *Biophys. J.*, 78:2761–Âη2775, June 2000.

[61] W. Rall. Core conductor theory and cable properties of neurons. In E. R. Kandel, editor, *Handbook of Physiology – Section 1: The Nervous System, Volume I: Cellular Biology of Neurons, Part I*, chapter 3, pages 39–97. American Physiological Society, Bethesda, MD, 1977.

[62] J. M. Rogers and A. D. McCulloch. A collocation-Galerkin finite element model of cardiac action potential propagation. *IEEE Trans. Biomed. Eng.*, X:YY–YY, 1994.

[63] J. M. Rogers and A. D. McCulloch. Nonuniform muscle fiber orientation causes spiral wave drift in a finite element model of cardiac action potential propagation. *J. Cardiovasc. Electrophysiol.*, 5:496–509, 1994.

[64] B. J. Roth. Action potential propagation in a thick strand of cardiac muscle. *Circ. Res.*, 68:162–173, 1991.

[65] B. J. Roth. A comparison of two boundary conditions used with the bidomain model of cardiac tissue. *Ann. Biomed. Eng.*, 19:669–678, 1991.

[66] B. J. Roth. Electrical conductivity values used with the bidomain model of cardiac tissue. *IEEE Trans. Biomed. Eng.*, 44:326–328, 1997.

[67] S. Rush and H. Larsen. A practical algorithm for solving dynamic membrane equations. *IEEE Trans. Biomed. Eng.*, BME-25:389–392, 1978.

[68] K. J. Sampson and C. S. Henriquez. Simulation and prediction of functional block in the presence of structural and ionic heterogeneity. *Am. J. Physiol. Heart. Circ. Physiol.*, 281:H2597–H2603, 2001.

[69] O. H. Schmitt. Biological information processing using the concept of interpenetrating domains. In K. N. Leibovic, editor, *Information Processing in the Nervous System*, pages 325–331. Springer-Verlag, New York, 1969.

[70] W. Shimizu and C. Antzelevitch. Cellular and ionic basis for T-wave alternans under long-QT conditions. *Circulation*, 99:1499–1507, 1991.

[71] S. Sicouri and C. Antzelevitch. A subpopulation of cells with unique electrophysiological properties in the deep subepicardium of the canine ventricle: The M cell. *Circ. Res.*, 68:1729–1741, 1991.

[72] *Scientific Computing Software Library (SCSL) User's Guide.* Silicon Graphics, Inc., December 2003. Available at `http://docs.sgi.com`, document number: 007-4325-001.

[73] R. F. Sincovec and N. K. Madsen. Software for nonliner partial differential equations. *ACM Trans. Math. Software*, 1:232–260, 1975.

[74] M. S. Spach. Anisotropy of cardiac tissue: A major determinant of conduction? *J. Cardiovasc. Electrophysiol.*, 10:887–890, 1999.

[75] M. S. Spach, P. C. Dolber, J. F. Heidlage, J. M. Kootsey, and E. A. Johnson. Propagating depolarization in anisotropic human and canine cardiac muscle: Apparent directional differences in membrane capacitance. A simplified model for selective directional effects of modifying the sodium conductance on $\dot{V}_{max}$, τ_{foot}, and the propagation safety factor. *Circ. Res.*, 60:206–219, 1987.

[76] M. S. Spach, J. F. Heidlage, P. C. Dolber, and R. C. Barr. Extracellular discontinuities in cardiac muscle: Evidence for capillary effects on the action potential foot. *Circ. Res.*, 83:1144–1164, 1998.

[77] B. M. Steinhaus, K. W. Spitzer, and S. Isomura. Action potential collision in heart tissue—computer simulations and tissue experiments. *IEEE Trans. Biomed. Eng.*, 32:731–742, 1985.

[78] W. A. Strauss. *Partial Differential Equations: An Introduction*. John Wiley & Sons, New York, 1992.

[79] D. D. Streeter, Jr. Gross morphology and fiber geometry of the heart. In R. M. Berne, N. Sperelakis, and S. R. Geiger, editors, *Handbook of Physiology – Section 2: The Cardiovascular System, Volume I: The Heart*, pages 61–112. American Physiological Society, Bethesda, MD, 1979.

[80] E. W. Swokowski. *Calculus with Analytic Geometry*. Prindle, Weber & Schmidt, Boston, Massachusetts, alternate edition, 1983.

[81] L. Tung. *A bidomain model for describing ischemic myocardial dc potentials*. PhD thesis, Massachusetts Institute of Technology, 1978.

[82] R. T. van Dam and D. Durrer. Experimental study on the intramural distribution of the excitability cycle and on the form of the epicardial T wave in the dog heart in situ. *Am. Heart J.*, 61:537–542, 1961.

[83] B. Victorri, A. Vinet, F. A. Roberge, and J.-P. Drouhard. Numerical integration in the reconstruction of cardiac action potentials using Hodgkin-Huxley-type models. *Comput. Biomed. Res.*, 18:10–23, 1985.

[84] E. J. Vigmond and L. J. Leon. Effect of fibre rotation on the initiation of re-entry in cardiac tissue. *Med. Biol. Eng. Comput.*, 39:455–464, 2001.

[85] E. J. Vigmond and L. J. Leon. Computationally efficient model for simulating electrical activity in cardiac tissue with fiber rotation. *Ann. Biomed. Eng.*, 27: 160–170, 1999.

[86] P. C. Viswanathan, R. M. Shaw, and Y. Rudy. Effects of i_{kr} and i_{ks} heterogeneity on action potential duration and its rate dependence: A simulation study. *Circulation*, 99:2466–2474, 1999.

[87] T. Watanabe, P. M. Rautaharju, and T. F. McDonald. Ventricular action potentials, ventricular extracellular potentials, and the ECG of guinea pig. *Circ. Res.*, 57:362–373, 1985.

[88] A. T. Winfree. Electrical instability in cardiac muscle: Phase singularities and rotors. *J. Theor. Biol.*, 138:353–405, 1989.

[89] A. T. Winfree. Heart muscle as a reaction-diffusion medium: The roles of electric potential diffusion, activation front curvature, and anisotropy. *Internat. J. Bifur. Chaos Appl. Sci. Engrg.*, 7:487–526, 1997.

[90] A. T. Winfree. *When Time Breaks Down.* Princeton University Press, Princeton, NJ, 1987.

[91] F. X. Witkowski, L. J. Leon, P. A. Penkoske, W. R. Giles, M. L. Spano, W. L. Ditto, and A. T. Winfree. Spatiotemporal evolution of ventricular fibrillation. *Nature*, 392:78–82, 1998.

[92] G.-X. Yan and C. Antzelevitch. Cellular basis for the normal T wave and the electrocardiographic manifestations of the long-QT syndrome. *Circulation*, 98: 1928–1936, 1998.

[93] G.-X. Yan, W. Shimizu, and C. Antzelevitch. Characteristics and distribution of M cells in arterially perfused canine left ventricular wedge preparations. *Circulation*, 98:1921–1927, 1998.

[94] J. Zeng, K. R. Laurita, D. S. Rosenbaum, and Y. Rudy. Two components of the delayed rectifier K^+ current in ventricular myocytes of the guinea pig type: Theoretical formulation and their role in repolarization. *Circ. Res.*, 77:140–152, 1995.

[95] D. P. Zipes and J. Jalife, editors. *Cardiac Electrophysiology: From Cell to Bedside.* W. B. Saunders Company, Philadelphia, PA, USA, second edition, 1995.

[96] A. C. Zygmunt, G. T. Eddlestone, G. P. Thomas, V. V. Nesterenko, and C. Antzelevitch. Larger late sodium conductance in M cells contributes to electrical heterogeneity in canine ventricle. *Am. J. Physiol. Heart. Circ. Physiol.*, 281:H689–H697, 2001.

[97] A. C. Zygmunt, R. J. Goodrow, and C. Antzelevitch. I(NaCa) contributes to electrical heterogeneity within the canine ventricle. *Am. J. Physiol. Heart. Circ. Physiol.*, 278:H1671–H1678, 2000.